

*To my parents,  
Américo and Maria Celeste;  
My grandmother,  
Emília;  
And my sister,  
Carolina.*



# CONTENTS

<b>Contents</b>	<b>i</b>
<b>List of Tables</b>	<b>v</b>
<b>List of Figures</b>	<b>vii</b>
<b>List of Publications</b>	<b>xi</b>
<b>Motivation and outline</b>	<b>1</b>
<b>1 Introduction</b>	<b>5</b>
1.1 Properties of diamond . . . . .	5
1.2 Applications of diamond . . . . .	6
1.3 Diamond synthesis . . . . .	7
1.4 Point defects in diamond: state of the art . . . . .	8
1.5 Nitrogen-related defects . . . . .	11
1.6 Transition metals in diamond . . . . .	15
1.6.1 Nickel . . . . .	16
1.6.2 Cobalt . . . . .	21
1.6.3 Other transition metals . . . . .	22
1.7 High temperature annealing of HPHT diamond . . . . .	23
1.7.1 Nitrogen aggregation . . . . .	23
1.7.2 Formation of nickel-nitrogen complexes . . . . .	25

<b>2</b>	<b>Experimental and theoretical framework</b>	<b>29</b>
2.1	Electron paramagnetic resonance . . . . .	29
2.1.1	Electronic states in a crystal . . . . .	30
2.1.2	Effective spin Hamiltonian . . . . .	32
2.1.3	Resonance condition . . . . .	38
2.1.4	Selection rules . . . . .	41
2.1.5	Anisotropy of the EPR spectrum . . . . .	42
2.1.6	Lineshape: Bloch equations . . . . .	44
2.1.7	Instrumentation . . . . .	47
2.1.8	Determination of spin concentrations . . . . .	50
2.2	Photoexcitation EPR . . . . .	51
2.2.1	Application of photo-EPR to point defects . . . . .	51
2.2.2	Electron-lattice coupling . . . . .	52
2.2.3	Photoionization optical cross section . . . . .	55
2.3	<i>3d</i> ions in semiconductors . . . . .	56
2.4	Infrared vibrational spectroscopy . . . . .	59
2.4.1	Lattice vibrations . . . . .	59
2.4.2	Infrared spectrum . . . . .	60
<b>3</b>	<b>Sample characterization</b>	<b>63</b>
3.1	Introduction . . . . .	63
3.2	Diamond samples . . . . .	63
3.3	Infrared absorption spectra . . . . .	65
3.4	EPR spectra . . . . .	67
3.4.1	Experiment . . . . .	67
3.4.2	Results . . . . .	68

<b>4</b>	<b>The AB paramagnetic centers</b>	<b>73</b>
4.1	Introduction . . . . .	73
4.2	Centers AB1 and AB3 . . . . .	73
4.2.1	EPR spectra of the AB1 and AB3 . . . . .	73
4.2.2	Nature of the AB1 and AB3 centers . . . . .	77
4.3	Center AB5 . . . . .	79
4.3.1	The AB5 spectrum . . . . .	79
4.3.2	The sign of $D$ . . . . .	82
4.3.3	Model of the AB5 center . . . . .	87
4.4	The AB2, AB4, and AB6 centers . . . . .	91
4.4.1	EPR spectra of the AB2, AB4, and AB6 . . . . .	91
4.4.2	Nature of the AB2, AB4, and AB6 defects . . . . .	97
4.5	Summary . . . . .	98
<b>5</b>	<b>Annealing study of HPHT diamond</b>	<b>101</b>
5.1	Introduction . . . . .	101
5.2	Experimental details . . . . .	102
5.3	Results and discussion . . . . .	103
5.3.1	Annealing sequence: sample J . . . . .	105
5.3.2	Annealing sequence: sample H . . . . .	107
5.4	The AB7 paramagnetic center . . . . .	111
5.4.1	The AB7 EPR spectrum . . . . .	111
5.4.2	Nature of the AB7 defect . . . . .	114
5.5	Summary . . . . .	115

<b>6 Photo-EPR of nickel-related centers</b>	<b>117</b>
6.1 Introduction . . . . .	117
6.2 Experimental details . . . . .	118
6.2.1 Diamond samples . . . . .	118
6.2.2 Photo-EPR equipment . . . . .	118
6.2.3 Photo-EPR: saturation method . . . . .	119
6.3 Photoionization Kinetics . . . . .	123
6.4 Substitutional nickel: W8 center . . . . .	126
6.4.1 Photoexcitation of the W8 center . . . . .	126
6.4.2 Temperature dependence of the 2.5 eV photoionization . . . . .	129
6.5 The NIRIM1 center . . . . .	133
6.6 The AB centers . . . . .	137
6.6.1 Center AB5 . . . . .	137
6.6.2 Center AB4 . . . . .	139
6.6.3 Center AB2 . . . . .	142
6.6.4 Center AB3 . . . . .	143
6.6.5 Discussion . . . . .	145
6.7 The role of N in the photoionization kinetics . . . . .	147
6.8 Summary . . . . .	148
<b>Concluding remarks</b>	<b>151</b>
<b>A Lorentzian function</b>	<b>155</b>

# LIST OF TABLES

1.1	Classification of diamond . . . . .	9
1.2	Calibration factors between the IR absorption coefficient and nitrogen concentrations . . . . .	14
1.3	Nickel-related paramagnetic defects in diamond . . . . .	19
2.1	Terms of the spin Hamiltonian . . . . .	34
3.1	List of the diamond samples . . . . .	64
3.2	Concentrations of the main defects in the crystals . . . . .	66
3.3	Paramagnetic centers detected in the samples . . . . .	70
4.1	$g$ -values for the AB1 and AB3 centers . . . . .	77
4.2	Spin Hamiltonian parameters for the AB5 defect . . . . .	82
4.3	$g$ -values of the AB2, AB4, and AB6 centers . . . . .	93
5.1	Concentrations of paramagnetic centers throughout the annealing sequence . . . . .	106
5.2	$g$ -values of the AB7 defect . . . . .	113
6.1	Huang-Rhys factors for some nickel centers . . . . .	146



# LIST OF FIGURES

1.1	Crystal structure of diamond . . . . .	5
1.2	IR absorption spectrum of $N_s^0$ . . . . .	13
1.3	IR absorption spectrum of $N_s^+$ . . . . .	15
1.4	IR absorption spectra of $A$ and $B$ aggregates . . . . .	16
2.1	Splitting of $^4F$ -term in octahedral crystal field . . . . .	33
2.2	State energies of a $S = \frac{3}{2}$ system vs. magnetic field $\mathbf{B}$ . . . . .	39
2.3	Energy-level scheme for a $S = I = \frac{1}{2}$ system . . . . .	40
2.4	Anisotropy of the spectra in an EPR experiment . . . . .	44
2.5	Block diagram of an EPR spectrometer . . . . .	48
2.6	Configuration coordinate diagram . . . . .	54
2.7	State energies of a $S = \frac{3}{2}$ system vs. magnetic field $B$ . . . . .	58
3.1	IR absorption spectrum of sample A . . . . .	65
3.2	EPR spectrum of the P1 and W8 . . . . .	69
3.3	EPR spectrum with the NE1 and NE2 lines . . . . .	71
4.1	EPR spectra showing the AB1 and AB3 lines . . . . .	74
4.2	Angular dependencies of the AB1 and AB3 EPR lines . . . . .	76
4.3	EPR spectra of the AB5center . . . . .	80
4.4	Angular dependence of the AB5 EPR lines in the $Q$ -band at 6 K. . . . .	81

4.5	Angular dependence of the AB5 EPR lines in the $Q$ -band at room temperature.	83
4.6	Angular dependence of the AB5 EPR lines in the $X$ -band . . . . .	84
4.7	Energy-level diagram for the AB5 center vs. magnetic field strength . . . . .	85
4.8	Part of the $X$ -band EPR spectrum of the AB5 center . . . . .	86
4.9	Temperature dependence of the intensity difference between AB5 EPR tran- sitions . . . . .	87
4.10	Filling of the $d$ -states for the AB5 center . . . . .	88
4.11	Atomic model of the AB5 center . . . . .	90
4.12	EPR spectrum of the AB4 center . . . . .	91
4.13	Angular dependence of the AB4 spectrum . . . . .	92
4.14	EPR spectrum with AB2 and AB6 lines . . . . .	94
4.15	Angular dependence of the AB2 EPR lines . . . . .	95
4.16	Angular dependence of the AB6 EPR lines . . . . .	96
5.1	Energy levels of the AB5 center manifold vs. magnitude of $B$ . . . . .	105
5.2	Structure proposed for the NE4 center . . . . .	109
5.3	EPR spectrum showing the AB7 defect lines . . . . .	112
5.4	Angular dependence of the EPR lines of the AB7 centers . . . . .	113
6.1	Optical setup in the photo-EPR measurements . . . . .	120
6.2	Time-dependence of the AB5 EPR signal intensity . . . . .	121
6.3	Dependence of the quenching of the W8 EPR signal . . . . .	123
6.4	Diagram of the processes which may occur during an electron photoionization experiment . . . . .	124
6.5	Quenching of the W8 EPR signal vs. excitation energy . . . . .	127
6.6	Spectral dependence of the enhancement of the P1 EPR signal intensity . . .	129
6.7	The configuration coordinate model scheme . . . . .	130

6.8	Spectral dependence of the quenching of the W8 EPR signal for 20 K, 60 K and 150 K . . . . .	132
6.9	Spectral dependence of the photoinduced changes in the intensity of the NIRIM1 spectrum . . . . .	134
6.10	Diagram of the energy levels of nickel and nitrogen in diamond . . . . .	135
6.11	Quenching and recovery of the AB5 EPR signal vs. the photon energy . . . .	138
6.12	Time-dependence of the EPR signal intensity of the AB4 center . . . . .	141
6.13	Spectral dependence of the AB4 EPR signal photoenhancement . . . . .	142
6.14	Spectral dependence of the photoinduced changes in the AB2 EPR signal . .	143
6.15	Spectral dependence of the AB3 EPR signal photoquenching . . . . .	144
A.1	Lorentzian lineshapes . . . . .	156



# LIST OF PUBLICATIONS

1. R. N. Pereira, W. Gehlhoff, A. J. Neves, N. A. Sobolev, *Photo-EPR studies on nickel-related defects in diamond*, submitted to Phys. Rev. B.
2. R. N. Pereira, A. J. Neves, W. Gehlhoff, N. A. Sobolev, L. Rino, H. Kanda, *Annealing study on the formation of nickel-related paramagnetic defects in diamond*, Diamond and Relat. Mater. **11**, 623-626 (2002).
3. R. N. Pereira, W. Gehlhoff, N. A. Sobolev, A. J. Neves, D. Bimberg, *Photo-EPR studies on the AB3 and AB4 nickel-related defects in diamond*, Physica B **308-310**, 589 (2001).
4. R. N. Pereira, W. Gehlhoff, N. A. Sobolev, A. J. Neves, D. Bimberg, *Determination of the W8 and AB5 defect levels in the diamond gap*, J. Phys.: Condens. Matter **13**, 8957-8964 (2001).
5. A. J. Neves, R. Pereira, N. A. Sobolev, M. H. Nazaré, W. Gehlhoff, A. Näser, H. Kanda, *New paramagnetic centers in annealed high-pressure synthetic diamond*, Diamond and Relat. Mater. **9**, 1057-1060 (2000).
6. A. J. Neves, R. Pereira, N. A. Sobolev, M. H. Nazaré, W. Gehlhoff, A. Näser, H. Kanda, *New paramagnetic defects in synthetic diamonds grown using nickel catalyst*, Physica B **273-274**, 651-654 (1999).



# MOTIVATION AND OUTLINE

Diamond has attracted science and technology researchers worldwide due to its unique properties, like high hardness, high thermal conductivity, and optical transparency. A combination of extreme properties makes diamond particularly well suited for applications demanding high speed, high power, and high temperature. The interest on diamond raised in the last decade as a consequence of the developments occurred in its synthesis both through high pressure and high temperature methods (HPHT) and metastable processes, like the existing variety of techniques based on chemical vapor deposition (CVD). These techniques permit the synthesis of diamond in a more controlled and reproducible way, regarding its morphology, dopants, shape, and surface. This improvement led both to scientific and technological developments.

The thermal and electrical conductivities, the color, and the radiation hardness are some of the properties of a material which are affected by point defects. In this context, the study of point defects is actually implicit on the investigation of a given solid, as they are strongly connected to the properties of the material. In the case of diamond, the identification and characterization of defects due to either accidental incorporation during synthesis, or resulting from premeditated doping, turned out to be a privileged field of research. The understanding of defects has been one of the research areas which has greatly gained with the feasibility of isotopically pure diamonds and, as yet in a restricted way, with the possibility of selective doping. Moreover, since point defects may influence the performance of diamond for semiconducting applications, the interest is no longer restricted just to the theoretical and fundamental aspects. A review of the present problems concerning the research of point defects in diamond was given by Davies (1999).

Transition elements of the  $3d$  group, namely Ni, Co, or Fe and their alloys, are used as solvent / catalysts for growing diamond at high pressure and high temperature. As a result of the growth mechanism, these atoms are unavoidably introduced in significant concentrations

in the crystal lattice, and consequently may limit the performance of diamond in potential applications. These impurities are responsible for a number of point defects which are detected optically and by electron paramagnetic resonance (EPR). Nowadays, the study of the role of defects related with transition metal ions in diamond is one of the most focused areas of research concerning point defects in diamond (Davies, 1999). A good understanding of the transition metal defects is critical in gaining insight into the synthesis mechanisms and, consequently, on its control. The interest of transition metals in HPHT diamond derives also from the fact that they affect the optical and electrical properties of diamond by introducing various energy levels in its energy gap. Another important issue regarding transition metals in diamond is their influence on the kinetics of nitrogen aggregation during heat treatments at high temperatures.

In this thesis, a study of point defects in diamond due to the incorporation of nickel impurities during the growth process at HPHT is presented. The investigations were carried out using diamond crystals grown by the HPHT method with nickel-alloys as solvent / catalysts. The experiments were based on the technique of the continuous wave electron paramagnetic resonance, often combined with optical excitation.

In the first chapter, a brief overview of the diamond properties and its synthesis processes is given. In this chapter, the main results achieved to date regarding the characterization of point defects in diamond are also summarized. To clarify the motivations of the study, special emphasis is given to the recently published articles on magnetic resonance studies of defects containing elements of the iron group.

Some details of the experimental and theoretical tools employed in the present investigations are put on view in Chapter 2. This chapter includes a description of the experimental features of the EPR technique and its theoretical background, as well as a description of its extension of photoexcitation electron paramagnetic resonance. A brief introduction to the experiment and theory of infrared absorption spectroscopy is also given.

In Chapter 3, the synthesis conditions of the crystals used in this research are given. A rough characterization of the samples was attained by means of infrared absorption spectroscopy and EPR experiments, so that the overall concentrations of nitrogen and nickel impurities in the samples could be estimated.

Chapter 4 is dedicated to the report of the paramagnetic properties of six nickel-related defects (AB centers) which were previously unknown. The solution of the challenging spec-

troscopic problems which came across yield the establishment of the electron spin and the parameters of the effective spin Hamiltonian which describes each one of these systems. The exploitation of the anisotropic properties of the EPR spectra that is presented in this chapter lead to the unambiguous determination of the local symmetries of the AB defects.

The behavior of the nickel-related paramagnetic centers upon high temperature heat treatments are studied in Chapters 5. In this chapter, the results which originated from an annealing study are shown. The experimental work consisted of a series of isochronal heat treatments performed in different samples at increasing temperatures. The data are discussed in the light of the recently published literature on the annealing behavior of nitrogen and nickel defects in HPHT diamond. The properties of another paramagnetic center labeled AB7 are also described.

In Chapter 6, the successful experimental observation of the optically induced quenching and/or enhancement of the EPR resonances related with nickel-containing centers is reported. The experiments were performed by means of the EPR technique associated with photoexcitation (photo-EPR). The study of the optical behavior of the nickel-related defects allowed us to infer about induced gap levels. A discussion about common characteristics of nickel defects is also presented. In this chapter, a theoretical description of the photo-EPR experiment when applied to the study of point defects in solids is also reported.

At last, a summary of the main results and conclusions is put on review. Also, suggestions of further work to be carried out in the research of defects related with  $3d$  ions in diamond are finally proposed.



# CHAPTER 1

## INTRODUCTION

### 1.1 PROPERTIES OF DIAMOND

Carbon is a group IV element with the electronic configuration  $1s^2 2s^2 2p^2$  which may crystallize in the so-called diamond structure when the  $s$  and  $p$  atomic orbitals hybridize forming tetrahedral  $sp^3$  bonds. Other group IV elements form solids with the same structure, among which Si and Ge are well known for being very important semiconductors. The diamond structure has a face-centered cubic (fcc) lattice with two atoms per unit cell (Figure 1.1). For

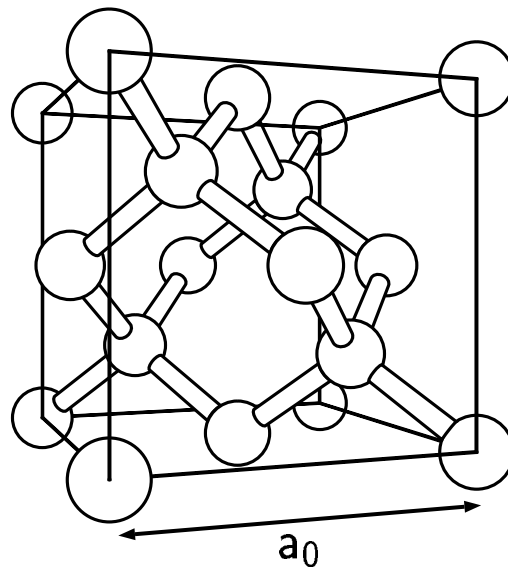


**Figure 1.1:** Crystal structure of diamond.

diamond, the measured cube edge at 25°C is  $a_0 = 3.56725 \text{ \AA}$ , with the distance between two nearest-neighbor carbon atoms being equal to  $1.5447 \text{ \AA}$  (Kaiser and Bond, 1959). The space group of the diamond structure is  $O_h^7$  (or  $Fd3m$  in international notation), comprising a total of 48 symmetry operations. From these, 24 belong to the point group  $T_d$  and the other 24 are rotation and reflection operations associated with a translation by the nonprimitive vector  $(a_0/4, a_0/4, a_0/4)$ .

Diamond is famous for being the material with the highest known hardness, but there are also other properties that are quite uncommon due to the strong covalent bonds between the carbon atoms. Some of these are the high thermal conductivity  $\sim 2500 \text{ Wm}^{-1}\text{K}^{-1}$ , the chemical inertness, the high refractive index  $n = 2.4237$  (at 546.1 nm), the elevated optical transparency, and the as well high electrical resistivity (Field, 1992).

The electronic band structure of diamond has been investigated both theoretically and experimentally (Pan and Kania, 1995). In thermal equilibrium the valence band of diamond is completely filled with electrons, whereas the conduction band is unoccupied. The maximum of the valence band and the minimum of the conduction band are located at different  $\mathbf{k}$  points. That is, the former is at the  $\Gamma$  point ( $\mathbf{k} = (0, 0, 0)$ ) of the Brillouin zone and the latter at  $3/4$  of the distance between the  $\Gamma$  and X points (along the six equivalent  $\langle 100 \rangle$  directions). Diamond may be considered as a wide-band gap semiconductor, since its indirect forbidden energy gap is found to be 5.47 eV, determined experimentally at 295 K (Clark *et al.*, 1964). For instance, industrially useful semiconductors like silicon and germanium have gap energies of 1.17 eV and 0.76 eV, respectively.

## 1.2 APPLICATIONS OF DIAMOND

Owing to its extreme mechanical properties and also chemical inertness diamond has been traditionally used in industry as an abrasive and as a coating material for certain wear applications. More recently, the use of diamond in heat dissipation devices has become very popular due to characteristics like the thermal expansion coefficient and thermal conductivity (Windischmann, 2001). Electronic and optical applications have also been emerging in the last years. Among the possibilities, we have radiation windows when high power and extreme mechanical, thermal, and chemical loads are needed (Wild and Koidl, 2001), X-ray

dosimeters (Vittone and Manfredotti, 2001), and electron beam devices, like electron and X-ray sources, high energy detectors, as well as high power switches and amplifiers (Zhirkov and Hren, 2001). More sophisticated applications have been also proposed, like the use of the well studied nitrogen-vacancy point defect in diamond for performing spin operations within the framework of the new quantum information and quantum computing science (Charnock and Kennedy, 2001).

### 1.3 DIAMOND SYNTHESIS

Many methods of synthesizing diamond are now available, allowing the fabrication of samples with different sizes and morphologies. Some of these are: the high pressure and high temperature synthesis (Burns and Davies, 1993), the shock-wave processing (Nassau, 1980), and the chemical vapor deposition techniques (CVD) (Butler and Goodwin, 2001). The development of CVD methods to fabricate large area films of diamond has focused attention on their vitally importance on the technological exploitation of the diamond physical properties (Nazaré and Neves, 2001). Alternatively, the high pressure and high temperature techniques lead to the growth of high quality single crystals. In the latter methods, graphite may be transformed into diamond upon the application of high pressure and high temperature. However, the high activation energy of the direct solid-solid transformation of graphite to diamond results in the fact that very high pressures and high temperatures are necessary in order to growth diamond at reasonable rates. Fortunately, it is possible to overcome this difficulty by employing many kinds of solvent / catalysts which assist in this transformation (Kanda and Sekine, 2001). Transition metals of group VIII, as well as alloys of these elements, have been used for this propose. Among those, Ni, Co, and Fe are the must commonly used. Other non-metallic catalysts like hydroxides, oxides, chlorides, carbonates and hydrides are also reported as useful catalysts (Kanda and Sekine, 2001). The metal-solvents dissolve carbon extensively and transport the carbon to the growing diamond surface. In this way the catalysts help in the formation of a supersaturated carbon solution. This catalyst solution is held at the temperature and pressure conditions at which diamond grows, allowing a faster conversion under easier and cheaper conditions (Burns and Davies, 1993). In order to grow large crystals it is usually applied a temperature gradient in the metal-carbon mixture. In this method the carbon source is usually composed of diamond

powers and a seed crystal is placed at the cooler region. The carbon dissolved in the higher temperature region is transported to the cooler region, where the solution becomes supersaturated with carbon. In this way, the carbon will precipitate on the seed leading to the growth of a bulk crystal. The required pressure is achieved by means of a hydraulic press made of tungsten carbide pistons and the melting of the nickel-carbon solution is afforded by means of an electrical system. The growth rate depends both on the growth temperature and temperature gradient. Low growth rates tend to form colorless crystals with lower impurity concentrations. The high-pressure cell process is able to produce single crystals with dimensions up to about 10 mm, with different morphologies. The faces commonly observed correspond to  $\{111\}$  and  $\{100\}$  crystallographic planes.

#### 1.4 POINT DEFECTS IN DIAMOND: STATE OF THE ART

The diamond material may contain extended defects, like twins, stacking faults, dislocations, platelets, and inclusions (Zhu, 1995; Clark *et al.*, 1993). Moreover, diamonds may possess point defects, which can be divided in two groups: (i) intrinsic defects (self-interstitials and vacancies) and (ii) impurity-related, with foreign atoms occupying either substitutional and/or interstitial sites.

The long-standing problems of the self-interstitial and vacancy centers in diamond were recently clarified in careful spectroscopic studies on nearly intrinsic synthetic diamonds (Newton *et al.*, 2001; Twitchen *et al.*, 2001).

The intrinsic lattice and band properties of diamond are strongly modified by impurities - wanted or unwanted. Diamond, both natural and synthetic, is never completely free of impurities. Nuclear probe techniques have detected a great number of elements inside natural diamonds (Sellschop, 1992). Most of these species are believed to be present in the form of inclusions and only a few were unambiguously identified as impurities bonded to the diamond lattice. The atoms which are known to lie on lattice sites are nitrogen (Smith *et al.*, 1959), boron (Collins and Williams, 1970; Isoya *et al.*, 1997b), nickel (Samoilovich *et al.*, 1971), cobalt (Twitchen *et al.*, 2000), silicon (Clark *et al.*, 1995), hydrogen (Woods and Collins, 1983), and phosphorous (Isoya *et al.*, 1997a). Walker (1979), Zaitsev (1998), Davies (1999) and Field (1992) reviewed the properties of optically detected defects and a compilation of paramagnetic centers can be found in a review by Ammerlaan (1990).

Nitrogen is found to be the dominant impurity in natural and synthetic HPHT diamond and determines most of its optical properties. The classification of the crystals according to the form and the amount of incorporated nitrogen reflects the importance of this impurity in diamond science (see Table 1.1). Diamonds with high nitrogen content ( $> 10$  ppm) are of type I, whereas crystals with low concentration of nitrogen defects belong to the type II group. A more detailed description of nitrogen defects will be given in the following section.

**Table 1.1:** Classification of diamond according to the amount and the form of nitrogen defects that they contain (see Section 1.5).

Type	Origin	Nitrogen defects
Ia	98% of the natural diamonds	<i>A</i> and <i>B</i> aggregates of nitrogen
Ib	$\approx 0.1\%$ of the natural HPHT diamonds	Nitrogen in the paramagnetic form (P1 centers)
IIa	Rare in nature	Few ppm of nitrogen; undetected by IR
IIb	Extremely rare in nature; some HPHT crystals	Less nitrogen than IIa in P1 centers; p-type semiconducting due to boron

Another important impurity is boron, which can be easily introduced in substitutional site due to its smaller atomic radius relative to carbon. Boron gives rise to p-type semiconducting behavior of type IIb crystals (Chrenko, 1973), with the acceptor state located at 0.368 eV above the valence band (Nazaré and Neves, 2001). Optical spectroscopy measurements have shown that boron occupies preferentially  $\{111\}$  and  $\{110\}$  planes over the  $\{100\}$  planes (Kawarada *et al.*, 1990). Boron doping of diamond can be achieved during the growth, by ion implantation or high temperature diffusion (Okano, 1995). Isoya *et al.* (1997b) have found a paramagnetic center in electron irradiated HPHT diamond doped with boron during

growth. The defect, labeled as NIRIM4, has an  $\langle 100 \rangle$ -split interstitialcy structure formed by a boron-nitrogen pair in the positive charge state.

The control of the incorporation of dopant atoms is a main technological issue. Principally those able to induce n-type doping of diamond. Very recently, Kalish (2001) reviewed the theoretical and practical achievements concerning the n-type doping of diamond. With its extremely low solubility of potential dopants, diamond seems to reject traditional doping techniques, as thermal diffusion and incorporation during growth. Nitrogen, being next to carbon in the Periodic Table, was considered to be the most probable n-type dopant of diamond. This expectation was frustrated by the observation that substitutional nitrogen creates a deep donor state in the energy gap (Farrer, 1969). Ion implantation, which is successfully applied in other semiconductors with low solubility of dopants, has been revealing restricted success in diamond (Dresselhaus and Kalish, 1992; Okano, 1995; Kalish and Uzan-Saguy, 2001; Prins, 2001). In theoretical studies, Katayama-Yoshida *et al.* (2001) proposed an alternative method of the co-doping by creating donor-acceptor-donor complexes with low activation energies, for example, nitrogen-boron-nitrogen complexes. Apart from nitrogen, the most investigated candidates to act as shallow donors in diamond are phosphorous and sulfur.

Phosphorus introduced during the growth of CVD diamonds seems to be a reproducible donor (Koizumi *et al.*, 1997). However, the reported activation energy of about 0.5 eV is still too large to promote enough electrons to the conduction band for n-type conduction at room temperature (Koizumi *et al.*, 1998). EPR investigations by Isoya *et al.* (1997a) yielded the identification of a P-N complex in type IIa HPHT crystals implanted with high energy phosphorus ions (NIRIM8 EPR center). Furthermore, Samsonenko *et al.* (1991) analyzed the EPR spectra of phosphorus-doped diamond powders and found a structure of two hyperfine lines, which they correlate with the incorporation of phosphorous ( $I = 1/2$ , natural abundance 100%).

The role of sulfur on the electronic properties of diamond have been more controversial. Although, theoretical calculations predict that substitutional sulfur may have relatively shallow levels in diamond (Saada *et al.*, 2000), experiments seem not to confirm such expectations (Kalish *et al.*, 2000).

Nuclear probe measurements proved that all natural diamonds contain hydrogen both as a surface layer and as an homogeneous bulk component. The bulk concentrations of hydrogen

are in the range from 500 to 3600 ppm (Sellschop, 1992). Since an hydrogen-rich mixture is used in the growth of diamond from the gas phase, hydrogen is present in large amounts in CVD diamond films. The first clear evidence for the presence of hydrogen bonded to the diamond lattice was given by Woods and Collins (1983). They showed that the infrared absorption peaks at  $3107\text{ cm}^{-1}$  and  $3098\text{ cm}^{-1}$  result from  $^{12}\text{C-H}$  and  $^{13}\text{C-H}$  vibrations, respectively. That is, the shift of the lines and their relative intensities are compatible with the mass and the natural abundance of the carbon-13 isotope. A review of the hydrogen related optical features in diamond was given recently by Zaitsev (2001). The interest of hydrogen has also been associated with its role on the passivation of donor and acceptor dopants in diamond (Chevallier, 2001; Chevallier *et al.*, 2001). *Ab initio* calculations proposed a possible shallow donor center containing hydrogen (Miyazaki *et al.*, 2002). This defect is a complex of two nearest-neighbor substitutional nitrogen atoms with hydrogen in the bond centered position. The fact that nitrogen pairs are easily formed in diamond (Chrenko *et al.*, 1977) and the discovery of a muonium trap in nitrogen-rich diamond (Machi *et al.*, 2000), suggest that this N-H-N complex may be a promising precursor of n-doping in diamond. Rosa *et al.* (1999) observed the generation of a defect with a photoionization energy of 1.2 eV through hydrogenation of CVD diamond films containing nitrogen.

Since this thesis is dedicated to the study of nickel-containing defects, a more detailed summary of the main results in the literature regarding transition metal centers in diamond is given in Section 1.6. The very important defects which are due to the nitrogen incorporation in diamond are reviewed in the following section.

## 1.5 NITROGEN-RELATED DEFECTS

Excluding impurities associated with inclusions, nitrogen is the most abundant impurity both in natural and HPHT diamonds and can be incorporated in different forms. Synthetic diamonds growth by the HPHT method at relatively low temperatures ( $\sim 1400^\circ\text{C}$ ) incorporate typically between 50 and 300 ppm of nitrogen, mostly in the single substitutional form. Natural crystals incorporate nitrogen predominantly in aggregated forms, *A* and *B* centers. In a small percentage of natural diamonds, nitrogen is present in the single substitutional form, these are named as type Ib (see Table 1.1). Only a very small fraction of natural stones has an extremely low amount of nitrogen (type II), which is undetectable by infrared

absorption spectroscopy (IR absorption).

Nitrogen substituting a carbon atom in the diamond lattice turns out to be paramagnetic when in the neutral charge state, giving rise to the well know P1 EPR signal originally studied by Smith *et al.* (1959). The P1 EPR spectrum is formed by a three line structure resulting from the hyperfine interaction with the almost 100% abundant  $^{14}\text{N}$  isotope with  $I = 1$ . The strength of the P1 spectrum may be used to measure the concentration of  $\text{N}_\text{s}^0$  defects.<sup>1</sup> The axial angular dependence of the hyperfine structure of the EPR spectrum established that the P1 is a defect with trigonal symmetry. Nitrogen forms four bonding orbitals with neighboring carbon atoms, being the remaining unpaired electron in an highly localized antibonding orbital directed along one of the  $\langle 111 \rangle$  directions of the bonds. The analysis of the hyperfine coupling with the nitrogen nucleus shows that the unpaired electron is located  $\sim 25\%$  on the nitrogen and  $\sim 75\%$  on the carbon that is bonded to nitrogen along the main axial direction (Loubser and van Wyk, 1978). Further EPR and electron-nuclear double resonance (ENDOR) measurements yielded to the determination of the hyperfine parameters of the  $^{15}\text{N}$  isotope ( $I = \frac{1}{2}$ ) and of the  $^{13}\text{C}$  neighboring atoms in seven inequivalent sites (Cox *et al.*, 1994). Smith *et al.* (1959) and Messmer and Watkins (1973) suggested that the trigonal symmetry of the P1 center was due to a Jahn-Teller distortion. EPR measurements above room temperature show that at temperatures higher than 600 K the unpaired electron hops between the four C-N bonds, proving that the trigonal distortion is not caused by a neighboring defect (Shu'lman *et al.*, 1967; Loubser and van Ryneveld, 1967). Calculations of the Jahn-Teller energy from the reorientation data contest the picture of a Jahn-Teller distortion driving the trigonal symmetry of the P1 defect. Furthermore, self-consistent Green's-function calculations of the unrelaxed substitutional nitrogen predict an  $A_1$  antibonding ground state, contradicting the interpretation that the axial distortion is resulting from a Jahn-Teller effect (Bachelet *et al.*, 1981). *Ab initio* calculations by Breuer and Briddon (1996) and Kajihara *et al.* (1991) concluded that there is solely an  $A_1$  state in the gap. With the trigonal distortion being due to the occupancy of the bonding/antibonding states in one of the N-C bonds.

Isolated  $\text{N}_\text{s}^0$  induce absorption in the infrared region of the spectrum, see Figure 1.2 (Chrenko *et al.*, 1971). The band at  $1130 \text{ cm}^{-1}$  is related with a C-N vibration, whereas the sharp

---

<sup>1</sup>In this work, the subscripts "s" and "i" are used to indicate the substitutional and interstitial tetrahedral sites.

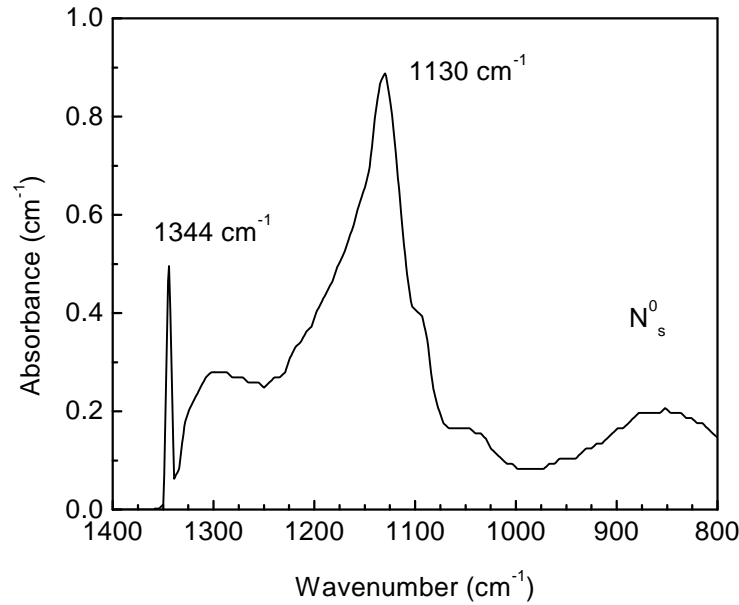


**Figure 1.2:** IR absorption spectrum in the one-phonon region of diamond due to  $N_s^0$ .

peak at  $1344\text{ cm}^{-1}$  is produced by a vibration mode of a C-C bond (Clark *et al.*, 1993). By comparing the intensity of the P1 EPR spectrum with the strength of the infrared absorption of type Ib synthetic diamonds was found that the concentration of  $N_s^0$  atoms  $[N_s^0]$  may be also determined using this spectrum. The correlation between the absorption coefficient at the maximum of  $1130\text{ cm}^{-1}$  measured in  $\text{cm}^{-1}$  and  $[N_s^0]$  obtained by Kiflawi *et al.* (1994) is given in Table 1.2. Farrer (1969) compared the photoconductivity and the optical absorption between 1.7 and 2.9 eV of type Ib diamonds and suggested that the optical threshold due to the substitutional  $N^0$  donor is 1.7 eV. From the temperature dependence of the resistance, measured in the same samples, the author determined a thermal activation energy of about 1.7 eV. Later on, Walker (1979) proposed an optical ionization energy for the  $N_s^0$  defect of 2.2 eV, taking into account that the thermal activation energy is 1.7 eV. The difference is due to relaxation towards the T-site experienced by  $N_s^0$  that is observed on the EPR measurements. Very recent photoconductivity and EPR experiments on CVD diamond doped with nitrogen corroborate the suggestion of Walker (1979) that the optical threshold of  $N_s^0$  is 2.2 eV (Rosa *et al.*, 1999).

In crystals containing defects which can act as acceptors (like boron, substitutional nickel or

**Table 1.2:** Calibration factors between the IR absorption coefficient  $\mu_x$  ( $\text{cm}^{-1}$ ), measured at room temperature and at the photon wave number  $x$  ( $\text{cm}^{-1}$ ), and nitrogen concentration for each of the spectral components  $\text{N}_s^0$ ,  $\text{N}_s^+$ ,  $A$  and  $B$ .

Defect	[N] (ppm)	Reference
$\text{N}^0$	$25.0 \pm 2 \times \mu_{1130}$	Kiflawi <i>et al.</i> (1994)
$\text{N}^+$	$5.5 \pm 1 \times \mu_{1332}$	Lawson <i>et al.</i> (1998)
$A$	$16.5 \pm 1 \times \mu_{1282}$	Boyd <i>et al.</i> (1994)
$B$	$79.4 \pm 8 \times \mu_{1282}$	Boyd <i>et al.</i> (1995)

vacancies),  $\text{N}_s^0$  may donate an electron, resulting in the formation substitutional  $\text{N}^+$  centers. Using IR absorption spectroscopy, Lawson *et al.* (1998) have assigned a previously detected component of the absorption spectrum, named as X-component (Lawson and Kanda, 1993), to substitutional  $\text{N}^+$ . The authors studied the changes produced in the concentration of  $\text{N}_s^0$  centers and in the X-component of the spectrum upon photoexcitation of diamond samples. Figure 1.3 shows the component of the infrared absorption spectrum produced by  $\text{N}_s^+$  defects. Absorption of  $1 \text{ cm}^{-1}$  at  $1332 \text{ cm}^{-1}$  in the IR spectrum of the  $\text{N}_s^+$  component corresponds to  $5.5 \pm 1$  ppm of  $\text{N}_s^+$  centers (see Table 1.2).

Aggregated forms of nitrogen in diamond of type  $A$  and  $B$  are also detectable by infrared absorption spectroscopy. Aggregates of the type  $A$  consist of two nearest-neighbor substitutional nitrogen atoms  $\text{N}_s\text{-N}_s$  (Davies, 1976). The neutral defect does not produce any signal in the electron paramagnetic resonance spectrum due to pairing of the two excess electrons (Jones *et al.*, 1992). The aggregates  $B$  are formed by four N atoms around one vacancy (Davies, 1999). Figure 1.4 shows the components of the IR absorption spectrum induced by the  $A$  and  $B$  aggregates in diamond. The calibration factors between the concentration of  $A$  and  $B$  defects and the absorption coefficient at  $1282 \text{ cm}^{-1}$  of the corresponding components in the IR spectrum are given in Table 1.2.

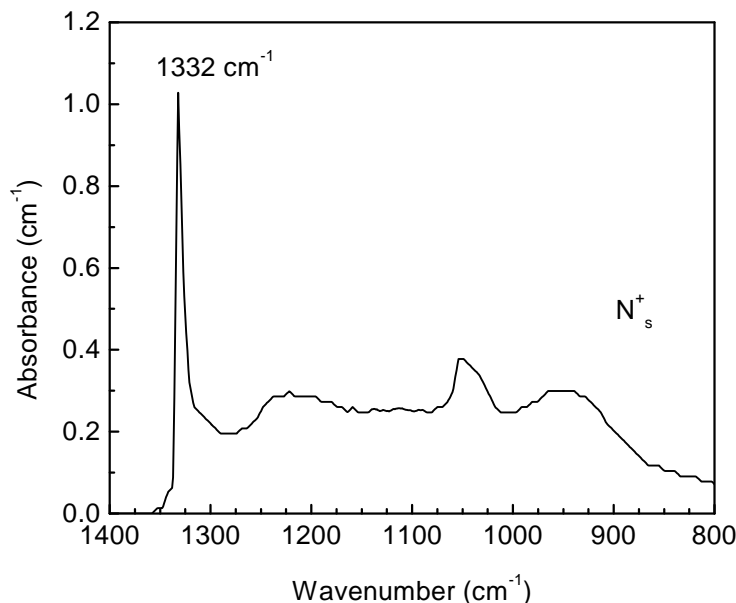


**Figure 1.3:** Shape of the absorption spectrum in the one-phonon region associated with  $N_s^+$  in diamond.

## 1.6 TRANSITION METALS IN DIAMOND

For many years researchers speculated about the possibility of incorporating heavy elements, like transition metal ions, in the diamond lattice. The use of alloys of  $3d$  elements as solvent / catalysts in the manufacture of synthetic diamond at high pressure and high temperature, let us to think that during the growth process some transition metals may be incorporated as inclusions and/or dispersed defects. In silicon, transition metal ions are known to be incorporated at interstitial sites of  $T_d$  symmetry (V, Cr, Mn, Fe, Co and Ni) and at substitutional sites (Cr and Mn) (Ludwig and Woodbury, 1960). Here, most of the experimental results were obtained by means of electron paramagnetic resonance. The differences in the behavior of the  $3d$  ions in silicon and diamond are presumably due to the much smaller space available in the diamond lattice for these relatively large ions and the metastability of the diamond carbon-phase at the atmospheric pressure. Until now, nickel (Samoilovich *et al.*, 1971; Davies *et al.*, 1989) and cobalt (Twitchen *et al.*, 2000) are the only transition metal elements which were unambiguously identified as constituents of impurity defects in diamond. Iron (Iakoubovskii and Adrienssens, 2002), copper (Baker, 2001), manganese (Iakoubovskii

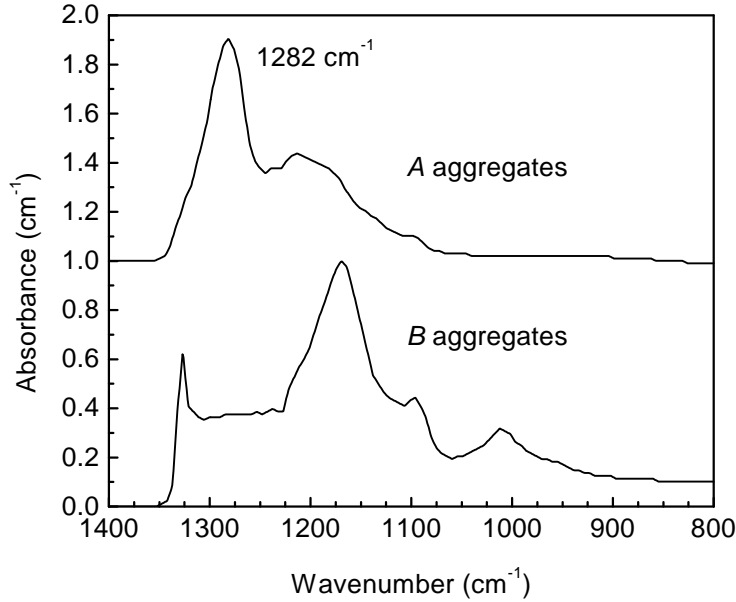


**Figure 1.4:** Characteristic one-phonon IR absorption spectra in the defect-induced region of the *A* and *B* aggregates. The spectrum of the *A* centers is shifted by  $1 \text{ cm}^{-1}$ .

and Stesmans, 2001), and titanium (Gippius and Collins, 1993) centers have been suggested, but not confirmed.

### 1.6.1 NICKEL

The first proof of the incorporation of a transition metal as a dispersed impurity in the diamond lattice was given by Samoilovich *et al.* (1971). They studied a previously observed isotropic EPR spectrum at  $g = 2.032$ , labeled W8 (Loubser and van Ryneveld, 1966). The samples were powdered diamond grown in a nickel system enriched with the isotope  $^{61}\text{Ni}$  ( $I = \frac{3}{2}$ , natural abundance 1.25%). EPR spectra of such samples exhibited a structure of four isotropic lines, indicative of the hyperfine interaction with the  $^{61}\text{Ni}$  nuclei. However, the use of powder samples and the isotropy of the EPR lines hindered the determination of the precise localization of the nickel impurity in the diamond lattice, as well as its electronic spin. More recently, Isoya *et al.* (1990a) performed pulsed Fourier-transform and continuous-wave EPR measurements to study the W8 center in synthetic HPHT diamonds. An effective spin state of  $S = \frac{3}{2}$  with the electronic configuration  $3d^7$  was determined through the Fourier-

transform nutational EPR spectra. Making use of the simple Ludwig-Woodbury model (see Section 2.3), which has been successfully applied to the description of transition metal elements in Si and Ge, the authors established that the observed configuration results from a negatively charged Ni occupying a tetrahedral substitutional position ( $\text{Ni}_\text{T}^-$ ).

Another conclusive evidence of the formation of a nickel defect in diamond resulted from optical spectroscopy studies on the 1.40 eV optical system with zero-phonon lines (ZPLs) at 1.401 and 1.404 eV and an associated broad band around 1.8 eV. This spectrum is typically observed by photoluminescence (PL) and absorption spectroscopy in synthetic diamonds with low nitrogen concentration (Collins *et al.*, 1990). Nazaré *et al.* (1991) have found an isotopic splitting in each one of the 1.40 eV zero-phonon lines with intensity ratios that matched the natural abundances of the Ni isotopes, showing that the center involves nickel. Photoluminescence upon uniaxial stress and Zeeman-PL measurements indicate that the 1.40 eV transitions occur in a trigonal center between a ground state doublet and an excited singlet state (Nazaré *et al.*, 1991). The ground state degeneracy was considered as being partially lifted by splitting into two states  $\Gamma_5$  and  $\Gamma_4$  due to the spin-orbit interaction. From the Zeeman results the authors estimated the  $g$ -values of the lower ground state to be  $g_{\parallel} = 2.42$  and  $g_{\perp} = \pm 1.28$ , and of the excited state  $g_{\parallel} = \pm 0.18$  and  $g_{\perp} = 2.5$ , both states having effective spin  $S = \frac{1}{2}$ . An interstitial  $\text{Ni}^+$  structure with electronic configuration  $3d^9$  was proposed for the defect, where the trigonal symmetry is produced by a distortion along an  $\langle 111 \rangle$  direction. In an EPR study of synthetic diamond, Isoya *et al.* (1990b) observed a trigonal defect named NIRIM2 with effective spin  $S = \frac{1}{2}$  and  $g_{\parallel} = 2.3285 \pm 0.0050$  and  $g_{\perp} \approx 0$ . The center was tentatively assigned to interstitial  $\text{Ni}^+$  (electronic configuration  $3d^9$ ) with the trigonal distortion produced by a neighboring vacancy or impurity. Both research groups proposed that the optical transitions at 1.40 eV and the NIRIM2 EPR spectrum would result from the same defect (Isoya *et al.*, 1990b; Nazaré *et al.*, 1991). Paslovsky and Lowther (1992) performed LCAO cluster calculations of nickel defects in diamond. Their results supported the suggestion that the 1.40 eV optical transitions occur in a trigonally distorted nickel defect, with the ground state splitting resulting from the spin-orbit coupling. The proposed model for the center was a relaxed interstitial  $\text{Ni}^+$  ion.

Very recently, Mason *et al.* (1999) investigated the Zeeman splitting of the 1.404 eV ZPL through the magnetic circular dichroism of the optical absorption (MCDA). Their experimental data were explained as arising from internal transitions occurring in a  $3d^9$  ion under

the crystal field of the interstitial site of diamond, plus a trigonal distortion and the spin-orbit interaction. They determined from the MCDA Zeeman data the  $g$ -values of the ground and excited states as being  $g_{\parallel} = 2.32$  and  $g_{\perp} = 0$  and  $g_{\parallel} \approx 0$  and  $g_{\perp} = 2.445$ , respectively. The sign of the MCDA and the determined  $g$ -values of the excited state corroborated the result from Nazaré *et al.* (1991) that the lower level of the ground doublet transforms as a  $\Gamma_{5,6}$  state. The unusual  $g$ -values of the excited  $\Gamma_4$  state were explained by an admixture, induced by the spin-orbit interaction, with another  $\Gamma_4$  excited state. The authors failed to optically detect electron paramagnetic resonance (ODEPR) associated with the 1.404 eV transition. Such observation would be a direct proof of the assignment of the 1.40 eV optical feature to the NIRIM2 EPR spectrum. Pawlik *et al.* (1998) studied several MCDA lines in synthetic diamonds by optically detecting the electron paramagnetic resonance via the MCDA (MCDA-ODEPR), namely, the bands at 1.72, 1.40 and 1.06 eV. The angular dependence of the MCDA-ODEPR spectra upon rotation of the external magnetic field about an  $\langle 111 \rangle$  direction, obtained at 1.40 eV, was found to be typical of a trigonal defect with  $g_{\parallel} = 2.32 \pm 0.01$ . Due to the close agreement between this value with that obtained by Isoya *et al.* (1990b) for the NIRIM2 spectrum ( $g_{\parallel} = 2.3285 \pm 0.0050$ ) the 1.40 eV line was assigned to the NIRIM2 EPR center (Pawlik *et al.*, 1998).

In the recent years several paramagnetic defects with strong evidence of nickel participation were detected by magnetic resonance techniques. These centers were correlated with nickel because they are found only in samples grown in nickel-containing solvent / catalysts and have  $g$ -values resulting from a non-negligible spin-orbit coupling  $\lambda \mathbf{L} \cdot \mathbf{S}$ , typical of such ions in diamond.

Isoya *et al.* (1990b), in their EPR study of synthetic diamonds grown from a Ni-containing solvent, observed an isotropic spectrum, labeled NIRIM1, with  $g = 2.0112$  at measurement temperatures higher than 20 K. Its spin state was found to be  $S = \frac{1}{2}$  by a pulsed EPR technique. The NIRIM1 EPR spectrum evidenced at 4 K a small anisotropy, that was interpreted as resulting from an intermediate Jahn-Teller effect associated with trigonal distortions. Isoya *et al.* (1990b) assigned the NIRIM1 center to interstitial nickel in the positive charge state ( $\text{Ni}_i^+$ ). Alike the NIRIM2 spectrum, the NIRIM1 signal was observed in diamonds grown from a nickel solvent with the addition of a nitrogen getter.

Using the MCDA and ODEPR techniques Pawlik *et al.* (1998) have studied an annealed diamond grown with a solvent / catalyst that contained nickel. In the MCDA spectra

**Table 1.3:** List of the nickel-related defects found in diamond by electron paramagnetic resonance. Other spin Hamiltonian parameters, like hyperfine constants, can be obtained in the corresponding references. See the text and references for details about the proposed structures shown in this table.

Center	Spin	Symmetry	$g$ -values	Model	Reference
W8	$\frac{3}{2}$	Cubic	$g = 2.0319$	$\text{Ni}_s^-$	Isoya <i>et al.</i> (1990a)
NIRIM1	$\frac{1}{2}$	Cubic	$g = 2.0112$	$\text{Ni}_i^+$	Isoya <i>et al.</i> (1990b)
NIRIM2	$\frac{1}{2}$	Trigonal	$g_{\parallel} = 2.3285$ $g_{\perp} \approx 0$	$\text{Ni}_i^+ \text{V}$	Isoya <i>et al.</i> (1990b)
NE4	$\frac{1}{2}$	Trigonal	$g_{\parallel} = 2.0227$ $g_{\perp} = 2.0988$	$(\text{NiVC}_6)^-$	Nadolinny <i>et al.</i> (1999)
NE1	$\frac{1}{2}$	Monoclinic-I	$g_1 = 2.1282$ $g_2 = 2.007$ $g_3 = 2.0908$	$(\text{NiVC}_4\text{N}_2)^-$	Nadolinny <i>et al.</i> (1999)
NE2	$\frac{1}{2}$	Triclinic	$g_1 = 2.1301$ $g_2 = 2.0100$ $g_3 = 2.0931$	$(\text{NiVC}_3\text{N}_3)^0$	Nadolinny <i>et al.</i> (1999)
NE3	$\frac{1}{2}$	Monoclinic-I	$g_1 = 2.0729$ $g_2 = 2.0100$ $g_3 = 2.0476$	$(\text{NiVC}_3\text{N}_3)^0$	Nadolinny <i>et al.</i> (1999)
NE5	$\frac{1}{2}$	Monoclinic-I	$g_1 = 2.0329$ $g_2 = 2.0898$ $g_3 = 2.0476$	$(\text{NiVC}_4\text{N}_2)^-$	Nadolinny <i>et al.</i> (1999)
RM1	$\frac{1}{2}$	Monoclinic-I	$g_1 = 2.1719$ $g_2 = 2.052$ $g_3 = 2.042$	$(\text{NiVC}_2\text{N}_4)^+$	Mashkovtsev <i>et al.</i> (1999)
ME1	$\frac{3}{2}$	$\sim$ Cubic	$g = 2.02$	$\text{Ni}_s^- \text{N}_{1-6}^+$	Noble <i>et al.</i> (1998)

they observed features at 1.29, 1.40, 1.69 and 1.72 eV. The authors were able to optically detect magnetic resonance on all these lines, showing that they are related with paramagnetic centers. By comparing the  $g$ -values obtained from the angular dependence of the

ODEPR spectra at 1.72 eV ( $g_{\parallel} = 2.004 \pm 0.005$  and  $g_{\perp} = 2.093 \pm 0.005$ ) with the values reported by Nadolinny and Yelisseyev (1994) for the NE4 center (see Table 1.3 and Subsection 1.7.2), Pawlik *et al.* (1998) concluded that the 1.72 eV doublet is correlated with the NE4 paramagnetic defect. The ODEPR measurements on the 1.06 eV MCDA line showed that this optical transition occurs in a  $S = \frac{1}{2}$  defect with trigonal symmetry (Pawlik *et al.*, 1998).

An analysis of natural blue diamonds from the Argyle mine in Western Australia carried out by Noble *et al.* (1998) revealed the appearance of a new band in the EPR spectra (labeled ME1 in Table 1.3). The spectrum consists of a broad line with peak-to-peak linewidth of about 1.4 mT centered at  $g = 2.02$ . Based on the evaluation of the data obtained from ENDOR measurements performed on this line, the authors proposed that the latter is due to a defect consisting of one substitutional  $\text{Ni}^{-}$  ion with an undetermined number of  $\text{N}_{\text{s}}^{+}$  ions in the six possible fourth-nearest-neighbor positions.

In addition to the nickel-related EPR centers described above, several optical absorption features are present in the region of the electromagnetic spectrum from the UV to the near infrared. As-grown diamonds synthesized through the HPHT method from a nickel-containing solvent, exhibit typically the optical absorption bands with zero-phonon lines (ZPLs) at 1.25, 1.40, 1.883, 2.51 and 3.1 eV. The photoluminescence spectra of this type of crystals tend to show the features with ZPLs at 1.40 and 2.56 eV. The 1.40 eV system is dominant in diamonds with nitrogen concentrations less than 10 ppm. The centers with ZPL at 1.883 and 2.51 eV are dominant in diamonds grown without a nitrogen getter, which have typical nitrogen concentrations  $[\text{N}] > 50$  ppm.

Topographic optical measurements have been giving a strong experimental evidence that nickel incorporates preferentially  $\{111\}$  growth sectors of synthetic diamond (Collins and Spear, 1982). Moreover, it is found that the increase of the nitrogen concentration in such growth sectors correlates with an increase of some nickel-related optical features (Kanda and Watanabe, 1999). Usually, the concentration of nitrogen impurities is higher in  $\{111\}$  than in  $\{001\}$  growth sectors (Burns *et al.*, 1990). Also the growth rate and the growth temperature have an influence on the concentration of transition metal and nitrogen defects in the different growth sectors. Kiflawi *et al.* (2002) have found that the growth rate increase produces higher concentrations of Ni (and Co) in the  $\{111\}$  growth sectors, as well as an increase of N impurities in the  $\{001\}$  growth sectors. Further, they found that the higher is

the incorporation of Ni defects in the  $\{111\}$  growth sectors the lower is the concentration of nitrogen in the same sectors.

### 1.6.2 COBALT

The first report of a cobalt related defect in diamond was due to Bagdasaryan *et al.* (1975). They investigated by EPR polycrystalline diamonds grown with pure transition metal catalysts and detected a new EPR signal in the magnetic field region corresponding to  $g \approx 4$ . The spectrum has a lineshape typical of powder samples, which could be explained assuming an axially symmetric  $g$ -tensor with an hyperfine structure resulting from interaction with a  $^{59}\text{Co}$  nucleus with spin  $I = 7/2$  (natural abundance 100%). It was proposed that the observed  $g$ -values are indicative of a transition metal ion with  $3d^7$  electronic configuration in an octahedral environment. By assuming that the Ludwig-Woodbury model applies to transition metal defects in diamond (see Section 2.3), the authors assigned the new spectrum to a distorted interstitial  $\text{Co}^{2+}$  ion.

Very recently, Twitchen *et al.* (2000) have detected a new paramagnetic defect, labeled O4, on an annealed HPHT diamond grown from a cobalt-containing solvent system. The observation of an eight line structure in the EPR spectra, which results from an hyperfine interaction with a nucleus of spin  $I = 7/2$ , clearly indicates that the spectrum is related to a cobalt-containing defect. The angular dependence of the EPR line positions permitted the assignment to a monoclinic-I system with the following  $g$ -values:  $g_1 = 1.8438$ ,  $g_2 = 1.7045$ , and  $g_3 = 2.3463$ . The measured  $g$ -values can be explained by considering a transition metal ion with  $t_2^5$  configuration in a distorted strong octahedral crystal field. It was speculated that according to the Ludwig-Woodbury theory the likely model of the O4 center is similar to that proposed for the NE4 nickel defect (see Subsection 1.7.2), with one of the six neighboring carbons being substituted by a nitrogen atom:  $(\text{CoVC}_5\text{N})^-$ . In this model, nitrogen plays a role in two different ways. It donates one extra electron to cobalt and lowers the symmetry of the defect from  $D_{3d}$  to  $C_{1h}$ .

In a PL study, Lawson and Kanda (1996) suggested that cobalt forms also several optically active centers in diamonds grown using cobalt as solvent / catalysts. As-grown crystals reveal a cobalt-related ZPL at 1.989 eV, whereas upon annealing, other features are created with ZPLs at 2.135 eV, 2.207 eV, 2.277 eV, 2.367 eV, and 2.590 eV. A weak absorption line at 1.852 has also been detected in diamonds grown with cobalt (Lawson and Kanda, 1996;

Zaitsev, 2000). Similarly to nickel, cobalt seems to be incorporated in diamond exclusively in the  $\{111\}$  growth sectors (Lawson and Kanda, 1996; Kiflawi *et al.*, 2002).

### 1.6.3 OTHER TRANSITION METALS

Although there is not an unambiguous proof of the incorporation in diamond of other transition metals than nickel and cobalt, some other  $3d$  elements have been tentatively assigned to EPR and optically detected features. Baker (2001) pointed out for the possibility that an EPR center named W36, previously ascribed to be boron-related, may be formed by a copper ion lying on a double semi-vacancy site. This model is similar to that proposed for the NE4 nickel-related EPR defect (see Subsection 1.7.2). His proposal was based on the re-analysis of the defect symmetry, the hyperfine structure of the EPR spectra and also on the measured value of the zero-field splitting.

Iakoubovskii and Stesmans (2001) reported the detection of an EPR signal consisting of a six line hyperfine structure in diamond powders grown at HPHT with a Ni-Mn alloy as solvent / catalyst. The spectrum was assigned to a defect containing a manganese ion, due to the nuclear spin  $I = 5/2$  of its nearly 100% abundant isotope  $^{55}\text{Mn}$ .

Bharuth-Ram *et al.* (1998) performed experiments of  $^{57}\text{Fe}$  implantation in diamond at temperatures up to 800 K. In-beam Mössbauer measurements have revealed the introduction of iron as a dispersed impurity in interstitial sites. Very recently, a photoluminescence center with a ZPL at 1.789 eV was exclusively found in diamonds which were grown from iron-containing solvent / catalysts (Iakoubovskii and Adrienssens, 2002). The authors speculate that this feature is due to a Fe-containing defect.

A titanium-related luminescence system at 1.249 eV have been reported by Gippius and Collins (1993) and Zaitsev (2000) in diamonds ion-implanted with  $\text{Ti}^+$  and subsequently annealed at high temperatures ( $\sim 1400^\circ\text{C}$ ). Optical features related with Zn and Cr are also reported in diamonds implanted with positively charged ions of these elements (Zaitsev, 2000).

## 1.7 HIGH TEMPERATURE ANNEALING OF HPHT DIAMOND

Owing to the great amount of recent work on the behavior of point defects upon high temperature annealing of HPHT synthetic diamond, a brief summary of the results related with the principal EPR and optical features is given.

### 1.7.1 NITROGEN AGGREGATION

Much of our knowledge about nitrogen in diamond comes from studies of its aggregation during heat treatments. An Historical perspective of nitrogen aggregation studies in diamond is given by Evans (1992). Chrenko *et al.* (1977) have found that annealing diamond at temperatures between 1700 and 1900°C under stabilizing pressures of about 6 GPa, caused the diffusion of single substitutional nitrogen atoms to form nearest-neighbor pairs. The authors found that this process obeyed second order kinetics (Chrenko *et al.*, 1977), where

$$\frac{dN_N}{dt} = -KN_N^2. \quad (1.1)$$

Here,  $N_N$  is the concentration of single nitrogen centers,  $t$  is time, and  $K$  is the aggregation rate constant. Evans and Qi (1982) suggested an hopping mechanism for the nitrogen migration with an activation energy of  $5 \pm 0.3$  eV at 1700°C and 7 GPa. The ratio between the concentration of  $N_s$  and  $A$  centers appearing in natural diamonds is determined by the time and temperature that they spent below the earth surface. At annealing temperatures of  $T_a > 2400^\circ\text{C}$ , a second stage of aggregation starts with the formation of  $B$  centers by the migration of  $A$  centers (Evans and Qi, 1982). Further annealing leads to the formation of platelets. Although the nature of platelets is still unknown it is believed that these are large extended defects composed predominantly of nitrogen. Alternatively, it is also possible that the platelets consist of a precipitate of interstitial carbon atoms with some participation of nitrogen (Woods, 1986; Lang *et al.*, 1992). Platelets induce a typical spectrum in the one-phonon region of the infrared absorption spectrum of diamond with a peak at  $1376\text{ cm}^{-1}$  (Evans, 1992).

During the formation of  $B$  aggregates, nitrogen form in minor amounts an optically active defect, labeled  $N3$  center (Clark *et al.*, 1956), comprising three tetrahedrally coordinated nitrogen atoms on a  $\{111\}$  plane with a vacancy at the center (van Wyk and Loubser, 1993). This defect produces an EPR spectrum labeled  $P2$  (Loubser and van Wyk, 1978). The

well known H3 and H4 nitrogen centers with zero-phonon lines at 2.463 eV and 2.499 eV may be produced on irradiated type Ia diamond upon annealing at  $T_a > 550^\circ\text{C}$ . These are believed to be formed when a vacancy is trapped by an  $A$  center (Davies, 1977a) or  $B$  aggregate (van Wyk and Woods, 1995), respectively. The H3 and H4 centers were found to be paramagnetic in an excited state, producing in this way the EPR spectra labeled W26 and W25, respectively (van Wyk and Woods, 1995).

Upon an annealing work carried out at  $1500^\circ\text{C}$  in vacuum, natural and synthetic type Ib diamonds showed that the introduction of vacancies by electron irradiation of the samples enhances the conversion of  $N_s$  centers to  $A$  aggregates (Collins, 1980). It was proposed that in samples with high concentration of nitrogen, the aggregation process involved multiple release and retrapping of vacancies (Collins, 1980).

In addition, Satoh and Sumiya (1995) suggested that the presence of solvent metal atoms, incorporated during growth of HPHT samples, affects the aggregation process. In the  $\{111\}$  growth sectors, where the transition metal impurities are preferentially incorporated (Collins and Spear, 1982), the aggregation rate of nitrogen is much higher than in the other sectors. Moreover, Kiflawi *et al.* (1997) observed that the aggregation rate evidenced as well differences within the same  $\{111\}$  growth sector. These differences resulted from changes in the growth temperature which influences the impurity content, namely an increase in the growth temperature was found to reduce the nitrogen aggregation constant  $K$ . They also reported a second order kinetics process for the conversion of  $N_s$  defects to  $A$  aggregates. However, the lack of any correlation between an optical feature and the concentration of cobalt in the crystal, hindered the observation of a direct relation between the aggregation rate and Co concentration. Furthermore, Kiflawi *et al.* (1998) performed topographic IR absorption measurements in diamonds grown from a nickel solvent system, where the nickel incorporation level was estimated through the absorption coefficient of the  $1332\text{ cm}^{-1}$  sharp peak, previously related to the positively charged nitrogen (Lawson *et al.*, 1998). This leads to a rough estimative of the concentration of substitutional Ni, since it is generally accepted that nitrogen transfers its unpaired electron to nickel, leading to the formation of the more stable negatively charged substitutional Ni defects (Isoya *et al.*, 1990a). In this way, they showed directly that the presence of Ni was responsible for an enhancement of the nitrogen aggregation. In contradiction to the previously reported results, it was found that in these experiments the formation of  $A$  centers did not followed second order kinetics. A similar

deviation from simple second order kinetics was observed by Fisher and Lawson (1998) in a work on Ni and Co catalyzed HPHT diamonds. Several reasons for the observed deviation were proposed: (a) nitrogen has different migration rates depending on the charge state; (b) nitrogen is forming *A* defects as well as nickel-nitrogen complexes; or (c) the migration is assisted by vacancies and/or carbon interstitials generated by nickel impurities (Kiflawi *et al.*, 1998). There is no experimental evidence that during the annealing process a significant amount of Ni-N centers is formed. Theoretical modelling pointed out that the most probable mechanisms are those which involve vacancies and carbon interstitials (Kiflawi *et al.*, 1998). Nadolinny *et al.* (2000) observed the presence of the W15 and W33 vacancy-containing paramagnetic centers in annealed diamond which were grown from nickel and cobalt solvents. Their observation is a weak indication that vacancies are produced during the heat treatments. Kiflawi *et al.* (1998) and Fisher and Lawson (1998) suggested that the interstitial-assisted aggregation process may be more effective than the vacancy-assisted mechanism. This is supported by the optical detection in intermediate annealing stages of the  $1450\text{ cm}^{-1}$  absorption peak related with interstitial nitrogen (Kiflawi *et al.*, 1996). Nickel being larger than carbon atoms may be a center of the generation of carbon interstitials, which create nitrogen interstitials by exchanging places with a substitutional nitrogen. Interstitial nitrogen is more mobile than substitutional nitrogen atoms, so the aggregation rate is increased.

### 1.7.2 FORMATION OF NICKEL-NITROGEN COMPLEXES

It has been observed that the defects related with nickel in diamond have a relatively complicated behavior upon high temperature annealing. Lawson and Kanda (1993) and Kupriyanov *et al.* (1999) studied the transformations experienced by the optical absorption and PL nickel-related features, respectively, while the annealing characteristics of nickel-containing paramagnetic centers have been studied by Nadolinny *et al.* (1999). Lawson and Kanda (1993) found that annealing nitrogen- and nickel-containing samples at temperatures in excess of  $1600^{\circ}\text{C}$  results in the growth of a complex absorption structure in the visible region at the expense of the optical transitions at 1.883 and 2.51 eV. Most of the new lines exhibit a transitory behavior upon annealing at increasing temperatures and only a few are present after annealing at temperatures higher than  $1900^{\circ}\text{C}$  (Lawson and Kanda, 1993). The 1.40 eV system appears to be rather stable, as it is observable in diamond samples that suffered very

high temperature annealing (Kupriyanov *et al.*, 1999). One of the transient defects produces a four line structure in the optical absorption spectrum with a ZPL at 1.693 eV. Uniaxial stress measurements on the 1.693 eV zero phonon line have shown that this is an electric dipole transition which occurs at a defect of orthorhombic-I symmetry (Neves *et al.*, 1999a). In the PL spectra of annealed nickel- and nitrogen-containing diamonds, the S3 (ZPL at 2.496 eV), S2 (ZPLs at 2.37 eV, 2.535 eV, and 2.596 eV), and 2.369 eV systems dominate (Nadolinny and Yelisseyev, 1993; Yelisseyev and Nadolinny, 1995; Kupriyanov *et al.*, 1999). Additionally, PL bands with ZPLs at 1.413, 1.563, 1.648, 1.660, 1.704, 1.940, 1.991, and 2.071 eV are also produced through the annealing of this type of diamonds (Kupriyanov *et al.*, 1999). Among these systems only the S2, S3, 1.563, and 1.648 eV persist after annealing at temperatures higher than 2000°C. The S2, S3, and 1.563 eV optical features are also typical of natural diamonds (Pereira, 1992). Photoluminescence excitation spectra of the 1.660 and 1.991 eV PL systems have revealed that they are responsible for the vibronic bands with ZPLs at 2.427 and 1.991 eV seen in the absorption spectra of annealed diamonds (Kupriyanov *et al.*, 1999). It is widely accepted that the emerging features are due to the formation of nickel-nitrogen complexes (Lawson and Kanda, 1993; Kupriyanov *et al.*, 1999; Yelisseyev and Nadolinny, 1995). In an annealing study of nitrogen-containing diamonds grown in the presence of cobalt, Lawson and Kanda (1996) suggested that nitrogen forms complexes with cobalt to produce optically active centers in a manner analogous to that of nickel.

Experimental support to the formation of nickel-nitrogen complexes is provided by EPR studies on annealed HPHT crystals by Nadolinny and Yelisseyev (1993, 1994) and Nadolinny *et al.* (1997). Nadolinny and co-workers have been studying a group of spin-half paramagnetic defects whose EPR spectra shows a multi-line structure due to the interaction of the unpaired electron with up to four nitrogen atoms. Namely, the NE1 and NE5 spectra reveal the presence of two equivalent nitrogen atoms and the EPR spectra of the NE2 and NE3 centers show the involvement of three nitrogen atoms. More recent studies of the  $^{13}\text{C}$  hyperfine structure in the EPR spectra of these nickel-nitrogen complexes yielded the confirmation or refinement of the originally proposed defect structure (Nadolinnny *et al.*, 1999). In addition, the authors report the detection of another paramagnetic defect named NE8. The authors proposed that all these centers are formed upon high pressure and high temperature annealing through the capture of four mobile nitrogen atoms by a trigonal paramagnetic defect labeled NE4. In their model, the NE4 center is the common fragment of the nickel-nitrogen

complexes NE1-NE3, NE5, and NE8, which differ only in the number and in the positions of the nitrogen atoms in the nickel coordination shell. Furthermore, the authors discuss that through the capture of one additional nitrogen atom, the NE1 and NE5 defects yield the formation of the NE2 and NE3 centers, respectively. It is argued that the NE4 center is formed, during the early stages of heat treatments, through the release of self-interstitials by substitutional  $\text{Ni}^-$  defects. In this process the nickel ion becomes positioned in the center of two semi-vacancies. In such an arrangement the defect would have  $D_{3d}$  point symmetry. In the present work, this basic structural unit will be represented by  $\text{NiVC}_6$ . The model for the NE4 EPR spectrum has not been unambiguously proved yet. However, the deviations of the  $g$ -values reported for all NE centers from the free electron value  $g_e$  strongly suggest that they contain nickel in their structure. The NE8 EPR spectrum, evidencing an hyperfine structure due to the interaction with four equivalent carbon atoms, seems to be the same as the RM1 spectrum reported independently by Mashkovtsev and Palyanov (1999). Some of the parameters of the RM1 spectrum are shown in Table 1.3. Both groups proposed a structure based on one nickel ion positioned in between two adjacent vacancies (i.e., NE4 defect model), which captured four nitrogen atoms in equivalent sites (Mashkovtsev and Palyanov, 1999; Nadolinny *et al.*, 1999). The S3, S2 and 2.369 eV nm vibronic systems, detected through photoluminescence spectroscopy, have been tentatively correlated with the NE1, NE2, and NE3 paramagnetic centers, respectively (Nadolinny and Yelisseyev, 1993; Yelisseyev and Nadolinny, 1995).

Noble *et al.* (1998) have also detected one of the nickel-nitrogen defects (the NE2 complex) in natural blue diamonds from the Argyle mine in Australia. The fact that most of the nitrogen incorporation in the studied samples was in the form of  $B$  aggregates, indicates that the crystals were subjected to high temperatures for a long period of time at some stage of their existence. This would be the reason for the appearance of NE2 defects in these natural diamonds.



# CHAPTER 2

## EXPERIMENTAL AND THEORETICAL FRAMEWORK

### 2.1 ELECTRON PARAMAGNETIC RESONANCE

The electron paramagnetic resonance (EPR) technique goes back more than fifty years, when Zavoiskii (1945) reported the first successful measurements. This technique may be applied whenever a system has unpaired electrons. For instance, in the understanding of reactions involving free radicals in biological and chemical systems (Atherton *et al.*, 1994; Gordy, 1980) or the study of transition metal complexes in solid states (Abragam and Bleaney, 1970; Pilbrow, 1990).

EPR is also a very powerful technique for studying the electronic structure of defects in semiconductors (Ludwig and Woodbury, 1962; Lancaster, 1966; Watkins, 1999). With this technique, we can obtain information concerning the total angular momentum and the local symmetry of point defects. Moreover, it can also give precious insight into the chemical nature of centers, with a great deal of information provided by nuclear hyperfine interactions. These interactions reveal both the nuclear spin and the relative abundance of the involved isotopes, which are both a clear chemical fingerprint of the atoms present in the center. Further information concerning the structure of defects is supplied by the anisotropic characteristics of such hyperfine interactions.

### 2.1.1 ELECTRONIC STATES IN A CRYSTAL

As a starting point, we will introduce the Hamiltonian of the whole crystal and then consider the approximations usually assumed in order to calculate its energy states. The Hamiltonian of the perfect crystal which neglects relativistic and magnetic terms is

$$\hat{\mathcal{H}} = \hat{\mathcal{H}}_n + \hat{\mathcal{H}}_e, \quad (2.1)$$

where  $\hat{\mathcal{H}}_n$  comprises the operator of the kinetic energy of the nuclei and the operator representing the interactions among the nuclei with mass  $M_l$ ,

$$\hat{\mathcal{H}}_n = \sum_l -\frac{\hbar^2}{2M_l} \nabla_l^2 + \sum_{l,k} U(\mathbf{R}_l - \mathbf{R}_k). \quad (2.2)$$

$\hat{\mathcal{H}}_e$  describes the kinetic energy of the electrons, and the electron-electron and electron-nuclei coulombic interactions,

$$\hat{\mathcal{H}}_e = \sum_i -\frac{\hbar^2}{2m_e} \nabla_i^2 + \frac{1}{4\pi\epsilon_0} \sum_{i>j} \frac{e^2}{|\mathbf{r}_i - \mathbf{r}_j|} + \sum_{i,l} V(\mathbf{r}_i - \mathbf{R}_l). \quad (2.3)$$

The energies  $E$  of the system are determined by the time-independent Schrödinger equation

$$\hat{\mathcal{H}} \psi(\mathbf{r}, \mathbf{R}) = E \psi(\mathbf{r}, \mathbf{R}), \quad (2.4)$$

where  $\psi(\mathbf{r}, \mathbf{R})$  are the eigenfunctions of the system, and  $\mathbf{r} \equiv (\mathbf{r}_1, \mathbf{r}_2, \dots)$  and  $\mathbf{R} \equiv (\mathbf{R}_1, \mathbf{R}_2, \dots)$ . The solution of the Schrödinger equation is impossible to attain in solids. Thus, some approximations are needed in order to calculate the energy values of a given system.

Since the mass of the electrons is very small when compared to the mass of the nuclei, the former can be regarded as instantaneously adjusting their motion to that of the nuclei. Therefore, the wavefunctions of the system in terms of the electronic coordinates  $\mathbf{r}$  and nuclear coordinates  $\mathbf{R}$  are written through the following first order ansatz:

$$\psi(\mathbf{r}, \mathbf{R}) = \varphi(\mathbf{r}, \mathbf{R}) \chi(\mathbf{R}). \quad (2.5)$$

These wavefunctions separate the electronic and nuclear motion. Then, in the adiabatic approximation, the Schrödinger equation is separated into two equations (Ridley, 1999),

$$\hat{\mathcal{H}}_e \varphi(\mathbf{r}, \mathbf{R}) = E_e \varphi(\mathbf{r}, \mathbf{R}), \quad (2.6)$$

$$\hat{\mathcal{H}}_n \chi(\mathbf{R}) = E_n \chi(\mathbf{R}). \quad (2.7)$$

This approximation implies that the eigenenergies of the nuclei  $E_n$  are not affected by the electronic states. This means that  $\varphi(\mathbf{r}, \mathbf{R})$  is the wavefunction of all the electrons and  $\chi(\mathbf{R})$  is the wavefunction of the nuclei.

Using the one-electron approximation and the periodic properties of the perfect crystal, it can be shown that the wavefunctions of the electrons in the static lattice are of Bloch type (Kittel, 1996),

$$\varphi_{n\mathbf{k}}(\mathbf{r}) = u_{n\mathbf{k}}(\mathbf{r}) \exp(i\mathbf{k} \cdot \mathbf{r}), \quad (2.8)$$

$$u_{n\mathbf{k}}(\mathbf{r} + \boldsymbol{\tau}) = u_{n\mathbf{k}}(\mathbf{r}), \quad (2.9)$$

where  $\boldsymbol{\tau}$  is a Bravais lattice vector,  $n$  labels the energy band and  $\mathbf{k}$  is the wavevector of the electron in the first Brillouin zone. The electronic structure of a perfect crystal consists of several energy bands with index  $n$ , which may be energetically separated by forbidden energy bands. In insulating and semiconducting materials, the highest energy band that is occupied (valence band) is completely filled with electrons. There is a continuous transition between isolators and semiconductors depending the energy separation  $E_g$  between the valence and the conduction bands. Diamond, with its  $\sim 5.5$  eV indirect energy gap, is commonly designated as a wide-band gap semiconductor.

The creation of point defects in the perfect lattice introduce a potential which is localized in space. The electronic part of the Hamiltonian of the system becomes

$$\hat{\mathcal{H}}_e = \hat{\mathcal{H}}_{e0} + \hat{U}, \quad (2.10)$$

where  $\hat{\mathcal{H}}_{e0}$  now denotes the electronic part of the Hamiltonian of the perfect crystal given in Equation (2.3) and  $\hat{U}$  is the perturbation introduced by the impurity. This potential leads to new solutions of the Schrödinger equation. Weak and delocalized potentials tend to produce states with energies close to the allowed band edges, whereas deep and localized potentials induce mid-gap levels. The latter are referred as deep defects. Excellent theoretical description of the electronic structure of defects in semiconducting materials has been given by Stoneham (1975) and Pantelides (1978). In Section 2.3, we will briefly introduce theoretical models used in the description of the electronic structure of transition metal impurities in semiconductors, since these are the type of defects which are studied in this work.

Physical interactions due to any externally applied magnetic field, as well as the magnetic dipole-dipole interaction and the spin-orbit interaction were not accounted for in the above

mentioned Hamiltonian  $\hat{\mathcal{H}}_e$ . The energy splittings produced by such interactions can be studied by electron paramagnetic resonance at feasible applied magnetic fields and microwave frequencies. In the following subsection, we will introduce the formalism which is normally used to describe the spin-dependent interactions of paramagnetic defects in crystals.

### 2.1.2 EFFECTIVE SPIN HAMILTONIAN

The ground state manifold of a paramagnetic ion in a crystal consists commonly of a group of electronic levels whose separation is of the order of a few reciprocal centimeters, whereas the energy separation to the other electronic states is much higher. The influence of ligand atoms on the ions of the iron-group series can be described by the well known crystal field or ligand field approach (Abragam and Bleaney, 1970). In the intermediate crystal field approach, the electronic states of the paramagnetic ion in the crystal are assumed to be the free ion  $LS$ -states which are affected by the electrostatic field of the surroundings. This interaction splits the different  $LS$ -states of the free ion term into several manifolds depending on the symmetry of the system. Such splitting is usually calculated using the ligand field interaction in the operator form (Abragam and Bleaney, 1970),

$$\hat{\mathcal{H}}_{\text{ligand}} = \sum_{k=2,4} \sum_{q=-k}^k B_k^q O_k^q, \quad (2.11)$$

where  $B_k^q$  are coefficients quantifying the strength of the crystal field and  $O_k^q$  are polynomials in the components of the orbital angular momentum. These polynomials for the different crystal field symmetries may be found in the Appendices 16 and 17 of the book from Abragam and Bleaney (1970). For the case of  $d^3$  and  $d^8$  configurations in an octahedral crystal field the  ${}^4F$ -term of the free ion is split into a ground orbital singlet state and two higher energy triplet states, as shown in Figure 2.1. In this case the orbital momentum of the ground state is completely quenched. The same is true for the  $d^2$  and  $d^7$  configurations in a tetrahedral ligand field (Abragam and Bleaney, 1970). A crystal field of lower symmetry cause further splitting of the states. An effect of the lifting of degeneracy produced by non-cubic crystal fields is that the ground states of transition metal ions have frequently a zero orbital angular momentum  $\mathbf{L}$  (van Vleck, 1932; Bourgoïn and Lannoo, 1981). This means that the energy levels of the ion may be essentially characterized by the spin. Therefore, we ascribe an effective spin  $S$  to the described manifold, which is a fictitious spin reflecting the multiplicity  $(2S+1)$  of the involved states at zero magnetic field (Abragam and Bleaney, 1970). All spin-

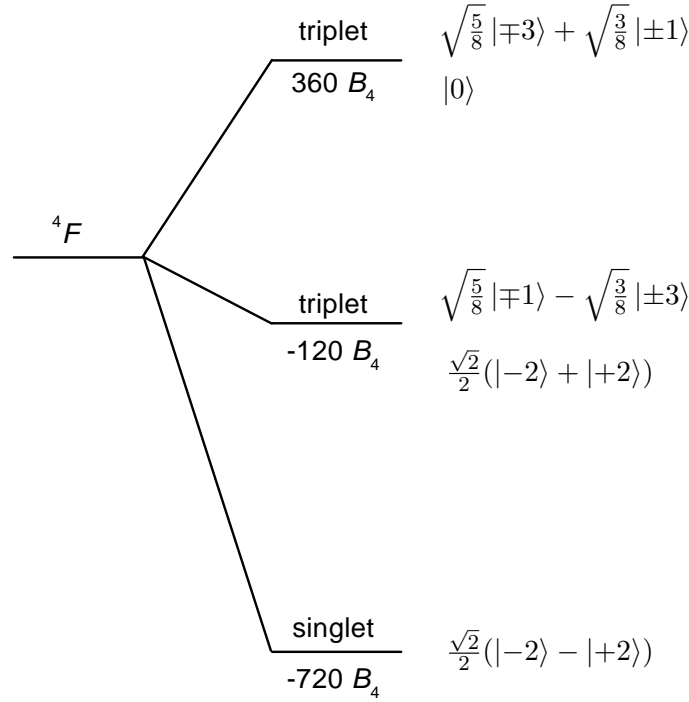


**Figure 2.1:** Splitting of the  ${}^4F$ -term ( $d^3$  and  $d^8$  configurations) in octahedral crystal field. In this case the cubic potential has the form  $\hat{\mathcal{H}}_{\text{ligand}} = B_4(O_4^0 + 5O_4^4)$  (Abragam and Bleaney, 1970).

dependent interactions within such manifolds (ground or excited states) can be described with a so-called spin Hamiltonian as a function of the electron and nuclear spin operators. In this energy operator the contributions of the orbital angular momentum are included in the parameters which mediate its different terms.

### TERMS OF THE SPIN HAMILTONIAN

The terms in the spin Hamiltonian depend on the magnetic field  $B$ , the electronic spin  $\hat{S}$  and a nuclear spin  $\hat{I}$ , all raised to a certain power. Generally, this dependence may be represented in the form  $B^a \hat{S}^b \hat{I}^c$ . For example, if  $a = c = 0$  and  $b = 2$ , the operator  $\hat{S}^2$  denotes for the term  $\hat{\mathbf{S}} \cdot \mathbf{D} \cdot \hat{\mathbf{S}}$ . The integers  $a$ ,  $b$  and  $c$  are limited by the invariance of the spin Hamiltonian under time-reversal ( $a + b + c = 2n$ ) and by the vector addition triangular inequality ( $b \leq 2S$ ,

$c \leq 2I$ ). If we neglect non-linear terms in  $\mathbf{B}$  then  $a \leq 1$ . Thus,

$$\begin{aligned} a + b + c &= 2n, \\ a \leq 1, \quad b &\leq 2S, \quad c \leq 2I, \end{aligned} \quad (2.12)$$

where  $n$  is an integer (Pake and Estle, 1973). In Table 2.1, the allowed terms for different combinations of spins  $S$  and  $I$ , limited by (2.12), are shown. Normally, the terms with higher

**Table 2.1:** Possible terms of the spin Hamiltonian according to the restrictions given in (2.12). The terms depending on  $I$  to a power higher than two were neglected as their contributions are extremely small. Adapted from Pake and Estle (1973).

$S \setminus I$	0	$\frac{1}{2}$	$\geq 1$
$\frac{1}{2}$	$B\hat{S}$	$B\hat{S}, \hat{S}\hat{I}, B\hat{I}$	$B\hat{S}, \hat{S}\hat{I}, B\hat{I}, \hat{I}^2, B\hat{S}\hat{I}^2$
1	$B\hat{S}, \hat{S}^2$	$B\hat{S}, \hat{S}\hat{I}, B\hat{I}, \hat{S}^2, B\hat{S}^2\hat{I}$	$B\hat{S}, \hat{S}\hat{I}, B\hat{I}, \hat{I}^2, B\hat{S}\hat{I}^2, \hat{S}^2, B\hat{S}^2\hat{I}, \hat{S}^2\hat{I}^2$
$\frac{3}{2}$	$B\hat{S}, \hat{S}^2, B\hat{S}^3$	$B\hat{S}, \hat{S}\hat{I}, B\hat{I}, \hat{S}^2, B\hat{S}^2\hat{I}, B\hat{S}^3, \hat{S}^3\hat{I}$	$B\hat{S}, \hat{S}\hat{I}, B\hat{I}, \hat{I}^2, B\hat{S}\hat{I}^2, \hat{S}^2, B\hat{S}^2\hat{I}, \hat{S}^2\hat{I}^2, B\hat{S}^3, \hat{S}^3\hat{I}, B\hat{S}^3\hat{I}^2$
$\vdots$			

powers have smaller contributions to the spin Hamiltonian and very often may be neglected in EPR experiments. For instance, the proper spin Hamiltonian of a system with spin  $S = 1$  and one nucleus with  $I = 1$  is usually written as,

$$\hat{\mathcal{H}} = \beta_e \mathbf{B} \cdot \mathbf{g} \cdot \hat{\mathbf{S}} + \hat{\mathbf{S}} \cdot \mathbf{D} \cdot \hat{\mathbf{S}} + \hat{\mathbf{S}} \cdot \mathbf{A} \cdot \hat{\mathbf{I}} + \hat{\mathbf{I}} \cdot \mathbf{Q} \cdot \hat{\mathbf{I}} - \beta_n \mathbf{B} \cdot \mathbf{g}_n \cdot \hat{\mathbf{I}}, \quad (2.13)$$

where the allowed higher order terms  $B\hat{S}\hat{I}^2$ ,  $B\hat{S}^2\hat{I}$  and  $\hat{S}^2\hat{I}^2$  are neglected. The matrices  $\beta_e \mathbf{g}$ ,  $\mathbf{D}$ ,  $\mathbf{A}$ ,  $-\beta_n \mathbf{g}_n$  and  $\mathbf{Q}$  mediate the coupling between the indicated vectors. The number of independent coefficients in these matrices, as well as their principal axes systems are determined by the symmetry of the spin system under study. These properties are normally obtained comparing the observed line positions in an EPR spectrum with those predicted by an analytic spin Hamiltonian. In most cases the complexity of the spin Hamiltonian does not allow analytical solution. In practice, its eigenvalues are evaluated numerically

by the use of a computer or through approximation methods, like the perturbation theory treatment (Weil, 1975).

The first and last terms in the spin Hamiltonian (2.13) correspond to the Zeeman interactions for the electron spin and nucleus spin, respectively. The constants  $\beta_e$  and  $\beta_n$  are the Bohr magneton and the nuclear magneton, respectively. Since  $\beta_e/\beta_n$  is equal to the ratio between the proton mass and the electron mass,  $m_p/m_e$ , the nuclear Zeeman term is comparatively small. When the magnetic field at the nucleus due to the electron spin magnetic moment (hyperfine field) is considerably stronger than the external magnetic field, the nuclear Zeeman term may be neglected. The term depending on the matrix  $Q$  determines the nuclear quadrupole interaction, which appears for  $I \geq 1$  and arises from the interaction between the nuclear quadrupole moment and the electric field gradient at the nucleus (Abragam and Bleaney, 1970; Slichter, 1996). Although the quadrupole and nuclear Zeeman terms may also be important for the interpretation of EPR spectra, they are of fundamental importance for experiments of nuclear magnetic resonance (NMR) (Günther, 1998; Bruch, 1996; Harris, 1986) and electron-nuclear double resonance (ENDOR) (Feher, 1956; Weil *et al.*, 1994; Sigel, 1987). The terms that are crucial for the analysis of electron paramagnetic resonance spectra are described in more detail in the following section.

### THE PARAMETERS IN THE SPIN HAMILTONIAN

As mentioned above, the orbital momentum of ions in crystals is frequently quenched due to the electrostatic interaction with the surrounding. However, also in such cases may exist a residual angular momentum from the admixture of certain excited states to the ground state caused by the spin-orbit and spin-spin interactions. Therefore, the  $g$ -factor of a crystal defect with an orbital singlet as ground state is not equal to the free electron value  $g_e = 2.002319$ . Because the admixtures of the excited states reflect the symmetry of the defect, the  $g$ -values are dependent on the angle between the direction of the magnetic field and the symmetry axes of the paramagnetic defect.

The Hamiltonian that describes the Zeeman interaction and the spin-orbit coupling in a  $LS$ -manifold is given by

$$\hat{\mathcal{H}} = \beta_e \mathbf{B} \cdot (\hat{\mathbf{L}} + g_e \hat{\mathbf{S}}) + \lambda \hat{\mathbf{L}} \cdot \hat{\mathbf{S}}, \quad (2.14)$$

where  $\hat{\mathbf{S}} = \sum_i \hat{\mathbf{s}}_i$  is the total spin operator and  $\hat{\mathbf{L}} = \sum_i \hat{\mathbf{l}}_i$  is the total orbital angular momentum operator, which are calculated in the framework of the Russell-Saunders coupling (Born,

1989). The spin-orbit term results from re-writing the interaction between the spins of the individual electrons  $\hat{\mathbf{s}}$  and their orbital momenta  $\hat{\mathbf{l}}$  (Griffith, 1961),

$$\sum_i \xi \hat{\mathbf{l}}_i \hat{\mathbf{s}}_i = \lambda \hat{\mathbf{L}} \cdot \hat{\mathbf{S}}, \quad (2.15)$$

where  $\lambda = \pm \xi/2S$ , with the  $+$  sign applying to a less than half-filled shell and the  $-$  sign to a more than half-filled shell. It can be shown that, for a singlet orbital state the Hamiltonian (2.14) may be written in the form of an effective spin Hamiltonian

$$\hat{\mathcal{H}} = \beta_e \mathbf{B} \cdot \mathbf{g} \cdot \hat{\mathbf{S}} + \hat{\mathbf{S}} \cdot \mathbf{D}_{\text{so}} \cdot \hat{\mathbf{S}}, \quad (2.16)$$

where  $\hat{\mathbf{S}}$  now denotes for the effective spin of the system. In second order perturbation theory the  $ij$ th element of the effective  $\mathbf{g}$ -matrix is given by

$$g_{ij} = g_e \delta_{ij} + 2\lambda \Lambda_{ij}, \quad (2.17)$$

where the subscripts  $i$  and  $j$  denote the directions  $x$ ,  $y$  or  $z$  and  $\Lambda_{ij}$  reads

$$\Lambda_{ij} = - \sum_{n \neq 0} \frac{\langle 0 | \hat{L}_i | n \rangle \langle n | \hat{L}_j | 0 \rangle}{E_n - E_0}. \quad (2.18)$$

Here  $E_0$  and  $E_n$  are the energies of the ground and excited states, respectively (Stoneham, 1975).

As we may see from Equation (2.16), there is a contribution from the spin-orbit coupling to the matrix  $\mathbf{D}$ , represented in the Hamiltonian (2.13), since the values of  $\mathbf{D}_{\text{so}}$  are related to  $\mathbf{g}$ . This part of the  $\mathbf{D}$ -matrix has the following form:

$$\mathbf{D}_{\text{so}} = \lambda^2 \mathbf{\Lambda}. \quad (2.19)$$

In addition to this, another important contribution to  $\mathbf{D}$  results from the electron-electron dipole interaction, i.e., interaction between the magnetic dipoles associated with the individual spins.

The third term in the spin Hamiltonian (2.13) represents the hyperfine interaction, which is due to the interaction between the unpaired electrons and the magnetic moments of the nuclei. A rigorous description of the various contributions to the matrix  $\mathbf{A}$  is given by Abragam and Bleaney (1970) and Stoneham (1975). The hyperfine coupling may be decomposed into an isotropic and an anisotropic part

$$\mathbf{A} = A_0 \mathbf{1} + \mathbf{T}, \quad (2.20)$$

where  $\mathbf{l}$  is a  $3 \times 3$  unit matrix. The isotropic term  $A_0$  is determined by the the Fermi contact interaction. It represents the interaction energy between the nuclear moment and the magnetic field produced at the nucleus due to the electron spin. It is given by

$$A_0 = \frac{2\mu_0}{3} g\beta_e g_n \beta_n |\varphi(0)|^2, \quad (2.21)$$

where  $\varphi(0)$  is the amplitude of the electronic wavefunction evaluated at the nucleus (Weil *et al.*, 1994). This contribution is non-zero for electrons in  $s$  orbitals, since they have a sufficient probability for being found within the nuclear volume. The anisotropic part  $\mathbf{T}$  of the hyperfine interaction arises from the dipole-dipole interaction between the electronic and nuclear magnetic moments. The expression for the dipole-dipole interaction for two dipole moments separated by a vector  $\mathbf{r}$  is

$$\hat{\mathcal{H}}_{\text{dipolar}}(\mathbf{r}) = \frac{\mu_0}{4\pi} g\beta_e g_n \beta_n \left( \frac{3(\hat{\mathbf{S}} \cdot \mathbf{r})(\hat{\mathbf{I}} \cdot \mathbf{r})}{r^5} - \frac{\hat{\mathbf{S}} \cdot \hat{\mathbf{I}}}{r^3} \right) \equiv \hat{\mathbf{S}} \cdot \mathbf{T} \cdot \hat{\mathbf{I}}. \quad (2.22)$$

The elements of the anisotropic component  $\mathbf{T}$  of the hyperfine coupling matrix due to this interaction are given by (Weil *et al.*, 1994),

$$T_{ij} = -\frac{\mu_0}{4\pi} g\beta_e g_n \beta_n \left\langle \frac{r^2 - 3i^2}{r^5} \right\rangle \quad i = j, \quad (2.23)$$

$$T_{ij} = -\frac{\mu_0}{4\pi} g\beta_e g_n \beta_n \left\langle -\frac{3ij}{r^5} \right\rangle \quad i \neq j, \quad (2.24)$$

where  $i$  and  $j$  denote for the spacial coordinates  $x$ ,  $y$ , or  $z$ . The hyperfine parameters  $A_0$  and  $\mathbf{T}$  quantify the amplitude and angular variation of the unpaired electron spin density around the nucleus. The resolution, in the EPR spectrum, of the structure which arises from the interaction with neighboring nuclei provides precious information concerning the species involved. This structure is commonly termed ligand hyperfine interaction or superhyperfine interaction.

#### EXAMPLE: QUADRUPLLET STATES ( $S = \frac{3}{2}$ )

As an example, a singlet orbital state with effective spin  $S = \frac{3}{2}$  will be considered. This is the case of the well known substitutional  $\text{Ni}^-$  defect in diamond. The spin Hamiltonian for a  $S = \frac{3}{2}$  state without any hyperfine interaction and with an isotropic  $g$  is

$$\hat{\mathcal{H}} = g\beta_e \mathbf{B} \cdot \hat{\mathbf{S}} + \hat{\mathbf{S}} \cdot \mathbf{D} \cdot \hat{\mathbf{S}}, \quad (2.25)$$

For simplicity, and also because of the small contribution to the energy levels, the Kostär-Statz term,

$$B\hat{S}^3 \equiv f\beta_e\{S_x^3B_x + S_y^3B_y + S_z^3B_z - \frac{1}{5}(\hat{\mathbf{S}} \cdot \mathbf{B})[3S(S+1) - 1]\}, \quad (2.26)$$

is neglected. It is often convenient to express the spin Hamiltonian (2.25) in the principal axes system (X,Y,Z) of the D-matrix

$$\hat{\mathcal{H}} = g\beta_e(B_X\hat{S}_X + B_Y\hat{S}_Y + B_Z\hat{S}_Z) + D_X\hat{S}_X^2 + D_Y\hat{S}_Y^2 + D_Z\hat{S}_Z^2. \quad (2.27)$$

If we take the quantization axis of  $\hat{\mathbf{S}}$  along the principal axis  $\mathbf{Z}$  and use the eigenfunctions  $|M_S\rangle = |+\frac{3}{2}\rangle, |+\frac{1}{2}\rangle, |-\frac{1}{2}\rangle$  and  $|-\frac{3}{2}\rangle$  of  $\hat{S}_Z$  as a basis set, the secular matrix of the spin Hamiltonian reads

$$\begin{bmatrix} \frac{3}{2}g\beta_e B_Z + D & \frac{\sqrt{3}}{2}g\beta_e(B_X - iB_Y) & \sqrt{3}E & 0 \\ \frac{\sqrt{3}}{2}g\beta_e(B_X + iB_Y) & \frac{1}{2}g\beta_e B_Z - D & g\beta_e(B_X - iB_Y) & \sqrt{3}E \\ \sqrt{3}E & g\beta_e(B_X + iB_Y) & -\frac{1}{2}g\beta_e B_Z - D & \frac{\sqrt{3}}{2}g\beta_e(B_X - iB_Y) \\ 0 & \sqrt{3}E & \frac{\sqrt{3}}{2}g\beta_e(B_X + iB_Y) & -\frac{3}{2}g\beta_e B_Z + D \end{bmatrix}, \quad (2.28)$$

with

$$D \equiv \frac{3}{2}D_Z, \quad (2.29)$$

$$E \equiv \frac{1}{2}(D_X - D_Y). \quad (2.30)$$

Only two independent energy parameters  $D$  and  $E$  are required to quantify the magnetic dipole-dipole interaction, since the trace of  $\mathbf{D}$  is zero ( $tr(\mathbf{D}) = 0$ ) (Pake and Estle, 1973). In the simple case of  $\mathbf{B} \parallel \mathbf{Z}$ , the secular determinant yields the following energy eigenvalues:

$$U_{1,2} = -\frac{1}{2}g\beta_e B_Z \pm \sqrt{(g\beta_e B_Z - D)^2 + 3E^2}, \quad (2.31)$$

$$U_{3,4} = +\frac{1}{2}g\beta_e B_Z \pm \sqrt{(g\beta_e B_Z + D)^2 + 3E^2}. \quad (2.32)$$

The axial and orthorhombic contributions of the matrix  $\mathbf{D}$  given by  $D$  and  $E$ , respectively, cause a partial raising of the fourfold spin degeneracy of the quadruplet state even in a zero magnetic field. This effect is usually designated as *zero-field splitting* (see Figure 2.2).

### 2.1.3 RESONANCE CONDITION

The interaction of an isotropic spin system with  $S = 1/2$  with a nuclear spin  $I = 1/2$  for a magnetic field  $\mathbf{B}$  along  $\mathbf{z}$  is described by the spin Hamiltonian

$$\hat{\mathcal{H}} = g\beta_e B_z\hat{S}_z + A(\hat{S}_z\hat{I}_z + \hat{S}_x\hat{I}_x + \hat{S}_y\hat{I}_y) - g_n\beta_n B_z\hat{I}_z. \quad (2.33)$$

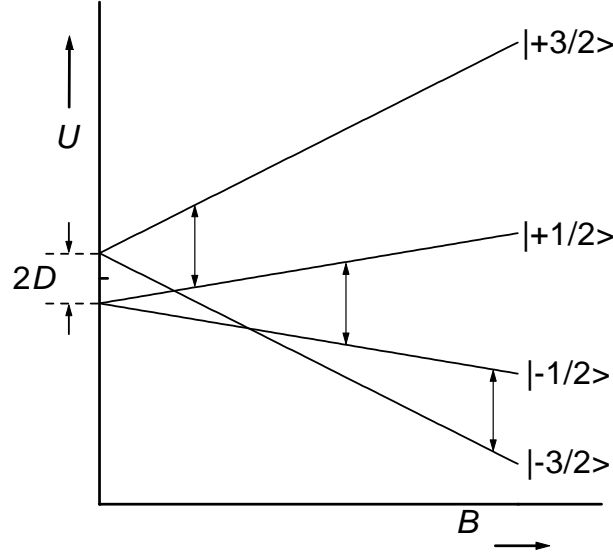


**Figure 2.2:** Energy levels for a  $S = \frac{3}{2}$  system, with  $D > 0$  and  $E = 0$ , as a function of an applied magnetic field  $\mathbf{B}$  parallel to  $\mathbf{Z}$ . When also  $E \neq 0$  the energy levels show a nonlinear variation with  $B$ . If both  $D$  and  $E$  are zero, the four eigenstates are degenerate for  $B = 0$  and the energy differences between the states  $M_S = \pm\frac{3}{2} \leftrightarrow \pm\frac{1}{2}$  and  $M_S = \frac{1}{2} \leftrightarrow -\frac{1}{2}$  for a given  $B$  are equal.

Using the eigenfunctions  $|M_S, M_I\rangle$  of  $\hat{S}_z$  and  $\hat{I}_z$  as a basis set, the following energies are obtained:

$$U_{1,2} = \pm \frac{1}{2} g \beta_e B_z + \frac{1}{4} A \mp \frac{1}{2} g_n \beta_n B_z, \quad (2.34)$$

$$U_{3,4} = -\frac{1}{4} A \pm \frac{1}{2} \left[ (g \beta_e + g_n \beta_n)^2 B_z^2 + A^2 \right]^{\frac{1}{2}}. \quad (2.35)$$

The corresponding eigenfunctions are

$$|S_{1,2}\rangle = |\pm 1/2, \pm 1/2\rangle, \quad (2.36)$$

$$|S_3\rangle = \cos \phi | +1/2, -1/2\rangle + \sin \phi | -1/2, +1/2\rangle, \quad (2.37)$$

$$|S_4\rangle = -\sin \phi | +1/2, -1/2\rangle + \cos \phi | -1/2, +1/2\rangle, \quad (2.38)$$

with the angle  $\phi$  given by,

$$\phi = \frac{1}{2} \arcsin \left\{ 1 + \left[ \frac{(g \beta_e + g_n \beta_n) B_z}{A} \right]^2 \right\}^{-\frac{1}{2}}. \quad (2.39)$$

When  $g\beta_e B_z \gg |A|$  the wavefunctions  $|S_3\rangle$  and  $|S_4\rangle$  are approximately  $|+1/2, -1/2\rangle$  and  $|-1/2, +1/2\rangle$ , respectively. Thus, for sufficiently high magnetic fields the functions  $|M_S, M_I\rangle$  are eigenfunctions of the spin Hamiltonian (see Figure 2.3). Resonant absorption occurs if the frequency is adjusted so that  $h\nu$  is equal to the energy difference  $\Delta U$  between levels with different  $M_S$ .

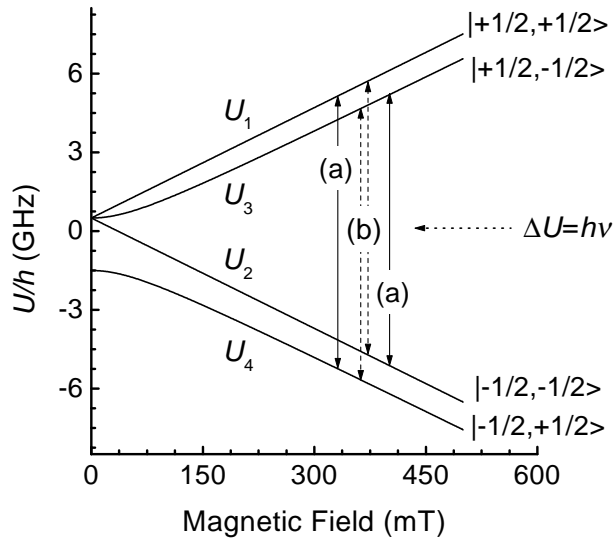


**Figure 2.3:** Energy-level scheme for an isotropic system with  $S = I = \frac{1}{2}$  as a function of an applied magnetic field  $B$ . The represented wave-functions are the high-field eigenfunctions, i.e, above the initial region of curvature ( $g\beta_e B_z \gg |A|$ ). The arrows represent the spin transitions which may be induced during an EPR experiment using a microwave frequency  $\nu$  in the  $X$ -band. Solid and dashed arrows apply for allowed (a) and "forbidden" (b) transitions, respectively.

There are two main experimental methods of studying electron paramagnetic resonance, the techniques of *continuous-wave* and *pulsed-resonance* (Mims, 1972; Sigel, 1987; Weil *et al.*, 1994). In the present work continuous-wave techniques were used, where the behavior of the resonant system is studied in a stationary regime by continuously applying an exciting microwave field. The applied microwave frequency is kept at a certain value  $\nu$  and the external magnetic field  $B$  is varied to locate the values at which resonance occurs (see Figure 2.3).

## 2.1.4 SELECTION RULES

The form of the interaction of the electromagnetic radiation with a spin system determines the probability of the transitions between the spin states. Under the resonance conditions, the transition probability between two states,  $|T_i\rangle$  and  $|T_f\rangle$ , is proportional to  $|\langle T_i | \hat{\mathcal{H}}_1 | T_f \rangle|^2$ . The operator  $\hat{\mathcal{H}}_1$  describes the perturbation on the spin system due to the magnetic component of the acting microwave radiation and is expressed by

$$\hat{\mathcal{H}}_1 = -\mathbf{B}_1 \cdot \hat{\boldsymbol{\mu}}, \quad (2.40)$$

where  $\hat{\boldsymbol{\mu}}$  is the total magnetic dipole operator of the spin system and  $\mathbf{B}_1$  is the amplitude vector of the magnetic component of the excitation microwave field. In the common case of having  $\mathbf{B}_1 \perp \mathbf{B}$ , choosing  $\mathbf{B} \parallel \mathbf{z}$  and  $\mathbf{B}_1 \parallel \mathbf{x}$ , one has

$$\hat{\mathcal{H}}_1 = g \beta_e B_1 \hat{S}_x - g_n \beta_n B_1 \hat{I}_x, \quad (2.41)$$

When  $|M_S, M_I\rangle$  are eigenfunctions of the spin Hamiltonian, the general matrix elements of  $\hat{\mathcal{H}}_1$  are

$$\begin{aligned} \langle M_S, M_I | \hat{\mathcal{H}}_1 | M'_S, M'_I \rangle &= g \beta_e B_1 \langle M_S | \hat{S}_x | M'_S \rangle \langle M_I | M'_I \rangle, \\ &- g_n \beta_n B_1 \langle M_S | M'_S \rangle \langle M_I | \hat{I}_x | M'_I \rangle. \end{aligned} \quad (2.42)$$

For EPR transitions these elements are zero unless  $M'_S = M_S \pm 1$  and  $M'_I = M_I$ . (The case  $M'_S = M_S$  and  $M'_I = M_I \pm 1$  not considered here is normally only realized in the NMR experiments (Günther, 1998; Bruch, 1996; Harris, 1986)). Thus, under high-field conditions the selection rules for transitions detected by EPR are

$$\Delta M_S = \pm 1 \quad \text{and} \quad \Delta M_I = 0. \quad (2.43)$$

In the example of Figure 2.3 only the transitions (a) are allowed at high magnetic fields ( $\Delta M_I = 0$ ). The other transitions (b) are allowed only at low fields, where the eigenfunctions become linear combinations of the  $|M_S, M_I\rangle$  states and the quantum numbers  $M_S$  and  $M_I$  are no longer applicable. These transitions are usually labeled "forbidden" transitions. It is seen from Equation (2.42) that the transition probability for a transition which satisfies the conditions (2.43) is proportional to  $(g \beta_e B_1)^2$ .

### 2.1.5 ANISOTROPY OF THE EPR SPECTRUM

The anisotropic Zeeman term, shown in Section 2.1.2, can be written in the matrix form as

$$\hat{\mathcal{H}}_{Ze} = \beta_e \mathbf{B}^T \cdot \mathbf{g} \cdot \hat{\mathbf{S}}. \quad (2.44)$$

The product  $\mathbf{B}^T \cdot \mathbf{g}$  may be regarded as an effective field,

$$\mathbf{B}_{\text{eff}}^T = \frac{B}{g_e} \mathbf{n}^T \cdot \mathbf{g}, \quad (2.45)$$

where  $\mathbf{n}$  is an unit vector in the particular direction of  $\mathbf{B}$ . When the electron spin is quantized along this effective field  $\mathbf{B}_{\text{eff}}$ , the new spin Hamiltonian  $g_e \beta_e \mathbf{B}_{\text{eff}}^T \cdot \hat{\mathbf{S}}$  yields the following eigenvalues for each particular direction  $\mathbf{n}$  (Weil *et al.*, 1994):

$$U_{M_S} = [\mathbf{n}^T \cdot (\mathbf{g} \cdot \mathbf{g}^T) \cdot \mathbf{n}]^{1/2} \beta_e B M_S = g(\mathbf{n}) \beta_e B M_S, \quad (2.46)$$

with the angular dependent  $g$ -value given by

$$\begin{aligned} g^2 = \mathbf{n}^T \cdot \mathbf{g} \mathbf{g} \cdot \mathbf{n} = & (\mathbf{g} \mathbf{g})_{xx} \sin^2 \theta \cos^2 \phi + 2(\mathbf{g} \mathbf{g})_{xy} \sin^2 \theta \cos \phi \sin \phi + \\ & (\mathbf{g} \mathbf{g})_{yy} \sin^2 \theta \sin^2 \phi + 2(\mathbf{g} \mathbf{g})_{xz} \cos \theta \sin \theta \cos \phi + \\ & 2(\mathbf{g} \mathbf{g})_{yz} \cos \theta \sin \theta \sin \phi + (\mathbf{g} \mathbf{g})_{zz} \cos^2 \theta, \end{aligned} \quad (2.47)$$

where  $\theta$  and  $\phi$  are the angles which define the direction of  $\mathbf{n}$  in polar coordinates.<sup>1</sup> For a spin-half system the energy difference between the paramagnetic states is

$$\Delta U = g(\theta, \phi) \beta_e B. \quad (2.48)$$

The tensor  $\mathbf{g} \mathbf{g}$  is determined experimentally through the spectroscopic measurement of the angular dependence of the  $B$  value which corresponds to a level splitting matching the microwave quantum  $h\nu$ ,

$$g(\theta, \phi) = \frac{h\nu}{\beta_e B(\theta, \phi)}. \quad (2.49)$$

In principle, it is necessary to perform the rotation of  $\mathbf{B}$  in three perpendicular crystal planes to evaluate all the elements of  $\mathbf{g} \mathbf{g}$ . However, in the case of defects in crystals with the

---

<sup>1</sup>The quantity  $\mathbf{g} \mathbf{g} \equiv \mathbf{g} \cdot \mathbf{g}^T$  have the transformation properties of a symmetric second-rank tensor (Abragam and Bleaney, 1970; Pake and Estle, 1973). It is the quantity which is measured experimentally, since the square roots of its eigenvalues correspond to the principal  $g$ -values determined in EPR. Therefore, in the literature the  $3 \times 3$  matrix  $\mathbf{g}$  is frequently assumed to be a tensor. In this context, the term tensor will be used in the following to designate all the anisotropic quantities of the spin Hamiltonian which are determined experimentally.

diamond structure, it is frequently enough to rotate the applied magnetic field in an  $\{110\}$  crystallographic plane. A defect whose symmetry operations are those of a point group  $G$  of order  $n_G$  (the number of symmetry operations of the point group), in a crystal with the site symmetry of order  $n_C$ , can take  $n_C/n_G$  different orientations (Kaplianskii, 1964). In diamond, the point group symmetry of the site centered at a carbon atom is  $T_d$ . Thus, the orientational degeneracy of a defect in diamond is  $24/g_G$ . Each one of the defect orientations can have a different angular dependence of the EPR lines and, correspondingly, a different tensor  $\mathbf{g}\mathbf{g}$ . The tensors  $\mathbf{g}\mathbf{g}_i$  of all equivalent orientations of the center are dictated by the point symmetry of the crystal and may be calculated through the similarity transformations,

$$\mathbf{g}\mathbf{g}_i = \mathbf{R}^{-1} \cdot \mathbf{g}\mathbf{g} \cdot \mathbf{R}, \quad (2.50)$$

with  $\mathbf{R}$  being matrixes representing the symmetry operations of the crystal and  $\mathbf{g}\mathbf{g}$  being the tensor of one particular symmetry site. After evaluating the elements of  $\mathbf{g}\mathbf{g}$ , it is possible to transform this tensor to its diagonal form and determine the corresponding normal directions. The square root of the resulting eigenvalues are the principal  $g$ -values of the defect and the normal directions determine the symmetry of the defect. There are eight symmetry systems to which a defect in a crystal with  $T_d$  point symmetry may belong. These are the cubic, tetragonal, trigonal, orthorhombic (I and II), monoclinic (I and II), and triclinic systems. The point groups belonging to each of these symmetry systems are defined by their common principal axes directions and common symmetry operations (Kaplianskii, 1964). For example, a defect with a trigonal symmetry in diamond may transform according to five point groups:  $D_{3d}$ ,  $D_3$ ,  $C_{3v}$ ,  $S_6$  or  $C_3$ . Helpful information regarding point group theory commonly applied to the study of defects, including point groups of the different symmetry systems, character tables and correlation tables, can be found elsewhere (Goss, 2000). Through the tensor  $\mathbf{g}\mathbf{g}$  only the symmetry system of a defect can be determined. The ligand hyperfine structure may lead to the determination of the precise point symmetry group of the defect.

The capability of the EPR in finding the symmetry of point defects is demonstrated in the following simple example of a paramagnetic center with  $S = 1/2$  and trigonal symmetry. A typical EPR pattern upon rotation of the magnetic field  $\mathbf{B}$  in an  $\{110\}$  crystallographic plane is shown in Figure 2.4. Although for trigonal symmetry the total number of possible orientations is eight, only four can be differentiated in an EPR experiment. This results from the fact that  $\mathbf{B}$  is an axial vector, which means, for example, that the directions  $[111]$  and  $[\bar{1}\bar{1}\bar{1}]$  cannot be distinguished. The four distinguishable center orientations produce only

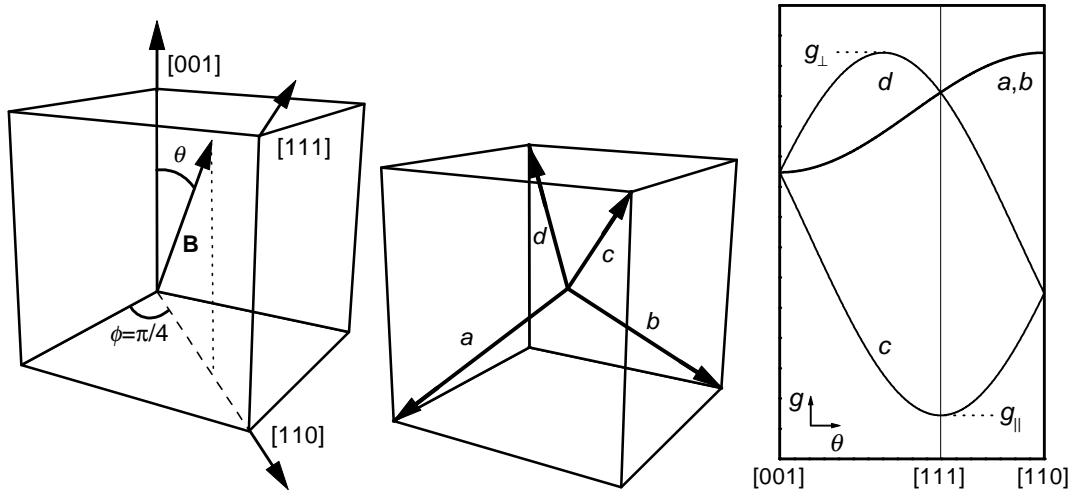


**Figure 2.4:** Orientation of the magnetic field  $\mathbf{B}$  relative to the cubic crystallographic axes (left). Direction of the principal axis  $\mathbf{Z}$  for each one of the four equivalent orientations of a defect with trigonal symmetry (center). Dependence of the EPR transitions by the rotation of the magnetic field in the  $(1\bar{1}0)$  plane (right).

three distinct angular variation curves for the rotation of  $\mathbf{B}$  in an  $\{110\}$  crystallographic plane (see Figure 2.4). The principal  $g$ -values of the paramagnetic center may be evaluated directly from a plot like that shown in Figure 2.4. In our example,  $g_{\parallel}$  is the value that the orientation  $c$  takes for  $\mathbf{B} \parallel [111]$  and  $g_{\perp}$  corresponds to the value that the orientations  $a$  and  $b$  take for  $\mathbf{B} \parallel [110]$ . So, the rotation experiment in one particular plane provides, in an unambiguous way, the  $g$ -values for a trigonal center. This is the reason why it is frequently possible to evaluate the tensor  $\mathbf{g}\mathbf{g}$  from solely one rotation experiment. When the anisotropic hyperfine term is added to the spin Hamiltonian and the system has orthorhombic symmetry ( $D_{2h}$ ,  $D_2$  or  $C_{2v}$ ), the normal directions of the tensors  $\mathbf{g}$  and  $\mathbf{A}$  must coincide. On the contrary, in triclinic symmetry ( $C_1$  or  $C_i$ ) each coupling tensor in the spin Hamiltonian may have its own principal axes system.

### 2.1.6 LINESHAPE: BLOCH EQUATIONS

A very useful description of the dynamics of EPR transitions is given by the Bloch equations, which accounts for the relaxation processes occurring during an EPR experiment. This

formalism was originally developed by Bloch (1946) to explain the nuclear magnetic resonance phenomena and describes the time-dependence of the total magnetization vector  $\mathbf{M}$ , defined as

$$\mathbf{M} = \frac{1}{V} \sum_i^N \boldsymbol{\mu}_i, \quad (2.51)$$

when a spin system is subjected to a magnetic field  $\mathbf{B}$  comprising a static component  $\mathbf{B}_0$ , taken along  $\mathbf{z}$ , and an oscillating component  $\mathbf{B}_1$  parallel to  $\mathbf{x}$ .  $\mathbf{M}$  is the magnetic moment of  $N$  individual magnetic dipoles per unit volume and precesses around the direction of  $\mathbf{B}$  when relaxation effects are neglected. Assuming that upon application of a magnetic field  $\mathbf{B}$ , the deviations of the longitudinal and transverse components of  $\mathbf{M}$  relax exponentially with respect to their equilibrium values, with time rates  $\tau_1$  and  $\tau_2$ , respectively, the vector  $\mathbf{M}$  moves according to the phenomenological equation

$$\frac{d\mathbf{M}}{dt} = \gamma_e \mathbf{M} \times \mathbf{B} - \frac{M_x \mathbf{i} + M_y \mathbf{j}}{\tau_2} - \frac{(M_z - M_z^0) \mathbf{k}}{\tau_1}, \quad (2.52)$$

where  $\gamma_e = g\beta_e/\hbar$ . The time constants  $\tau_1$  and  $\tau_2$  are called the *longitudinal* and *transverse relaxation times*, respectively. Expressing the system of differential equations given by Equation (2.52) in a new coordinate frame  $(x_\phi, y_\phi, z)$  that is rotating about  $\mathbf{z}$  at the same angular frequency  $\omega$  of  $\mathbf{B}_1$ , and solving the result for steady-state conditions, one obtains the following expressions for the components of the magnetization (Weil *et al.*, 1994):

$$M_{x_\phi} = -M_z^0 \frac{\gamma_e B_1 (\omega_0 - \omega) \tau_2^2}{1 + (\omega_0 - \omega)^2 \tau_2^2 + \gamma_e^2 B_1^2 \tau_1 \tau_2}, \quad (2.53)$$

$$M_{y_\phi} = +M_z^0 \frac{\gamma_e B_1 \tau_2}{1 + (\omega_0 - \omega)^2 \tau_2^2 + \gamma_e^2 B_1^2 \tau_1 \tau_2}, \quad (2.54)$$

$$M_z = +M_z^0 \frac{1 + (\omega_0 - \omega)^2 \tau_2^2}{1 + (\omega_0 - \omega)^2 \tau_2^2 + \gamma_e^2 B_1^2 \tau_1 \tau_2}, \quad (2.55)$$

with  $\omega_0 = -\gamma_e B_0$ . Here,  $M_z^0$  is the steady-state magnetization along  $\mathbf{z}$  in the absence of the oscillating field. For very high values of  $B_1$ , the magnetization  $\mathbf{M}$  vanishes. The magnetization vector is directly proportional to the magnetic field,

$$\mathbf{M} = \chi \frac{\mathbf{B}}{\mu_m}, \quad (2.56)$$

with  $\chi$  being the susceptibility and  $\mu_m$  the permeability of the medium. Thus, one can define the dynamic susceptibilities

$$\chi' = \chi^0 \frac{\omega_0 (\omega_0 - \omega) \tau_2^2}{1 + (\omega_0 - \omega)^2 \tau_2^2 + \gamma_e^2 B_1^2 \tau_1 \tau_2}, \quad (2.57)$$

$$\chi'' = \chi^0 \frac{\omega_0 \tau_2}{1 + (\omega_0 - \omega)^2 \tau_2^2 + \gamma_e^2 B_1^2 \tau_1 \tau_2}, \quad (2.58)$$

with  $\chi^0$  being the static magnetic susceptibility.  $\chi'$  and  $\chi''$  are the *dispersive* and *absorptive* parts of a complex susceptibility  $\chi' - i\chi''$ . When measuring EPR in the absorption mode, the detected EPR signal is proportional to the fractional change in the resistance of the resonator that is produced during the sweep of the absorption curve. This can be written as (Pilbrow, 1990),

$$\frac{\Delta R}{R} = 4\pi\eta Q \chi'', \quad (2.59)$$

where  $\eta$  is the filling factor and  $Q$  is the quality factor of the resonator. The filling factor is a measure of the efficiency with which the microwave magnetic field is concentrated in the sample. Poole (1983) derives expressions of  $\eta$  for particular cases commonly observed in EPR experiments. In general, the filling factor is proportional to the ratio between the sample volume  $V_s$  and the cavity volume  $V_c$ ,  $V_s/V_c$ . The quality factor is an important parameter of the cavity loaded with a sample and is related to the energy losses in the resonator. Some details about the  $Q$  value will be given in the following section. For a reflection cavity and detection in the linear region of the detector characteristic curve we have (Poole, 1983),

$$\frac{\Delta R}{R} = \frac{\Delta V_r}{V}, \quad (2.60)$$

where  $V$  is the applied voltage and  $\Delta V_r$  is the change in the reflected voltage. Since  $V \propto P_0^{1/2}$ , the change in the reflected voltage at the detector crystal is according to Equation (2.59) given by

$$\Delta V \propto \eta Q \chi'' P_0^{1/2}, \quad (2.61)$$

which in turn is proportional to the EPR signal. Substituting Equation (2.58) in (2.61), it is easily found that the EPR signal reads

$$S(\omega_0 - \omega) \propto \frac{\pi\eta Q \chi^0 \omega_0 P_0^{1/2}}{(1 + \gamma_e^2 B_1^2 \tau_1 \tau_2)^{1/2}} Y(\omega_0 - \omega), \quad (2.62)$$

where  $Y(\omega_0 - \omega)$  is a normalized Lorentzian function (see Appendix A) with the linewidth given by

$$\Gamma = \frac{(1 + \gamma_e^2 B_1^2 \tau_1 \tau_2)^{1/2}}{\tau_2}. \quad (2.63)$$

Thus, the Bloch formalism predicts that the EPR lines have a Lorentzian shape, which are homogeneously broadened according to Equation (2.63). The intensity of an EPR line  $I_{\text{EPR}}$  is defined as the area under the corresponding absorption curve. In EPR, the modulation-phase-sensitive detection technique produces first-derivative lines that provide better resolved spectra (see the following subsection). For first-derivative Lorentzian shaped EPR lines,

$$I_{\text{EPR}} = \frac{\pi}{\sqrt{3}} A_{\text{pp}} \Delta B_{\text{pp}}^2, \quad (2.64)$$

where  $A_{\text{pp}}$  and  $\Delta B_{\text{pp}}$  are the peak-to-peak amplitude and linewidth, respectively. According to Equation (A.3) the peak-to-peak amplitude has the following dependence on the magnitude of  $\mathbf{B}_1$ :

$$A_{\text{pp}} \propto \frac{\eta Q \chi^0 \omega_0 B_1 \tau_2^2}{(1 + \gamma_e^2 B_1^2 \tau_1 \tau_2)^{3/2}}. \quad (2.65)$$

The amplitude of the signal varies linearly with  $B_1$  ( $\propto P_0^{1/2}$ ) for relatively small values of  $B_1$ . In this case, the system is out of saturation. If the exciting microwave power  $P_0$  ( $\propto B_1^2$ ) further increases,  $A_{\text{pp}}$  reaches a maximum and then decreases for higher incident powers. The resonant system is in the so-called power saturation regime. This emphasizes the importance of choosing an adequate microwave power for the detection of an EPR signal. When the saturation term  $\gamma_e^2 B_1^2 \tau_1 \tau_2 \ll 1$ , the linewidth is approximately constant, increasing only when saturation effects set in. The stationary solutions of the magnetization are only applicable if the sweep is slow as compared with the time rates  $\tau_1$  and  $\tau_2$ , i.e.,  $dB_0/dt \ll B_1/(\tau_1 \tau_2)^{1/2}$ . The EPR spectrum is then said to be obtained in slow-passage conditions, otherwise, the spectra is measured under fast-passage conditions.

Apart from the homogeneous broadening which is quantified through Equation (2.63), an EPR line can also undergo an inhomogeneous broadening. Inhomogeneously broadened lines consist of a family of overlapping lines, which may result from unresolved fine and/or hyperfine structures, or fluctuations of the applied magnetic field throughout the sample. The latter effects tend to produce lines which have a Gaussian-like shape.

### 2.1.7 INSTRUMENTATION

Usually, continuous-wave EPR spectrometers operate at a constant frequency with the magnetic field varying linearly within the region of interest. Such equipments consist typically of a microwave bridge, housing the microwave source; a waveguide; a microwave resonant cavity; a magnet and its power supply; and an electronic circuit that detects the microwave signal and displays the result (see Figure 2.5). The use of preamplifiers and of the lock-in technique causes a considerably improvement of the signal-to-noise ratio. The magnetic field is modulated in order to perform a phase-sensitive detection (PSD) at the modulation frequency of the magnetic field. Such a method provides a greater sensitivity than a DC detection technique. Modern X-band spectrometers achieve a sensitivity of about  $10^9$  spins per mT under standard conditions.

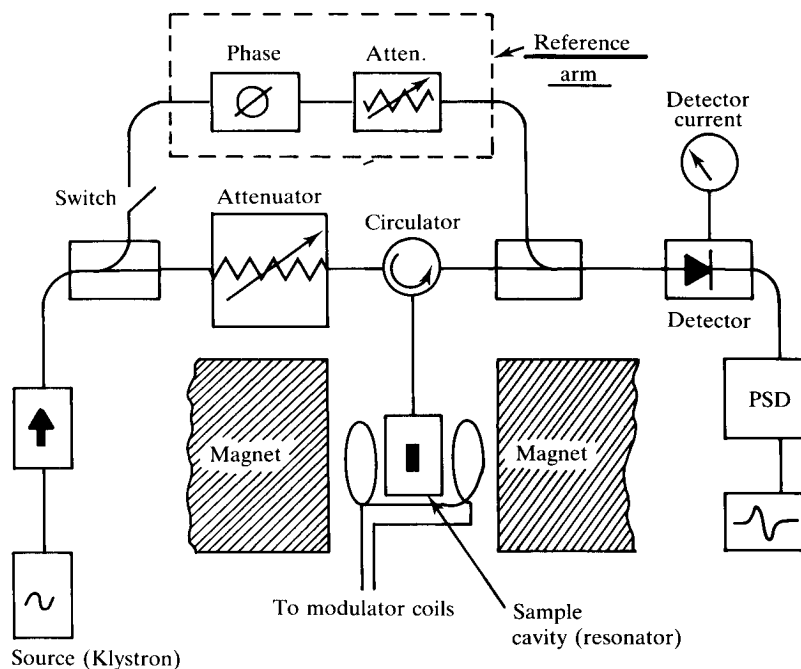


**Figure 2.5:** Block diagram of an EPR spectrometer. Taken from Pilbrow (1990).

The microwave power is generated by a klystron or Gunn diode which is provided with an automatic frequency control (AFC). For measuring EPR in the absorption mode, the AFC regulates the spectrometer in a way that the dispersion part of the susceptibility is ruled out, by stabilizing the klystron frequency to the resonance frequency of the cavity. An attenuator controls the used microwave power and a frequency counter measures the radiation frequency. A circulator forces the incident microwave radiation to the microwave cavity and directs the reflected power to the detector crystal. After this, the signal is split into two components: one conveys the error signal to the AFC and the other goes to the preamplifier. The latter signal is filtered by a lock-in detector (commonly operating at 100 kHz) that eliminates a large part of the noise. An oscilloscope can be used as an alternative mode for rapid scans and for tuning the cavity. The reference arm guides microwave power from the klystron directly to the detector, permitting an appropriate biasing of the power level at the detector.

The field modulation is often achieved by placing small Helmholtz coils on each side of the cavity. The modulation frequency  $\nu_m$  should be much less than the peak-to-peak linewidth

$\Delta B_{\text{pp}}^0$  expressed in frequency units,

$$\nu_{\text{m}} \ll \frac{g\beta_{\text{e}}}{h} \Delta B_{\text{pp}}^0, \quad (2.66)$$

in order to avoid distortion of the lineshape.  $\Delta B_{\text{pp}}^0$  is the linewidth which would be observed at zero amplitude of the magnetic field modulation. When the modulation amplitude  $B_{\text{m}}$  is much lower than  $\Delta B_{\text{pp}}^0$ , the observed linewidth  $\Delta B_{\text{pp}}^{\text{obs}}$  is unchanged. If the modulation amplitude approaches  $\Delta B_{\text{pp}}^0$ , the observed lines begin to broaden and distort (Poole, 1983). For  $B_{\text{m}} < \Delta B_{\text{pp}}^0$ , the peak-to-peak amplitude  $A_{\text{pp}}$  of a first-derivative line increases linearly with  $B_{\text{m}}$ , reaching a maximum for  $B_{\text{m}} \approx 3.5\Delta B_{\text{pp}}^0$  for Lorentzian shaped absorption lines. When resolution is important, the modulation amplitude should be at least one-half of the expected structure splitting, provided that the sensitivity is not compromised.

An important part of an EPR spectrometer is the resonator, where the sample is located. A wide variety of resonators may be employed for measuring EPR (Poole, 1983). The commonly used resonators are the cylindrical  $\text{TE}_{011}$  and the rectangular  $\text{TE}_{102}$  cavities. The cavity walls are highly conductive, allowing the formation of a standing electromagnetic wave. The dimensions of the cavities are related with the microwave frequency value. In both cavities the electric field standing wave is aligned in the plane perpendicular to the vertical axis. The location of the maximum of the magnetic field  $\mathbf{B}_1$  corresponds to the location of the minimum of the electric field component. Usually,  $\mathbf{B}_1$  is chosen perpendicular to the static magnetic field direction (see Subsection 2.1.4), and the sample should be placed where  $\mathbf{B}_1$  has its maximum value. To compare measurements obtained in different cavities, we must know the quality factors  $Q$  of the resonators. The quality factor of an empty resonator  $Q_{\text{u}}$  (unloaded) corresponds to the ohmic losses in the walls of the cavity,

$$Q_{\text{u}} = \frac{2\pi(\text{energy stored in the resonator per cycle})}{(\text{energy dissipated per cycle})}. \quad (2.67)$$

In addition, there are energy losses due to the cavity coupling hole and due to the existence of materials inside the resonator that have a non-zero imaginary dielectric constant. These losses are quantified by the coupling quality factor  $Q_{\text{r}}$  and the dielectric factor  $Q_{\epsilon}$ , respectively. Since most of the dielectric losses occur in the sample and the sample holder, it is important to position the sample inside the cavity in a region where the microwave electric field is minimum. The overall quality factor  $Q$  is given by summing the reciprocals of the different factors (Poole, 1983),

$$\frac{1}{Q} = \frac{1}{Q_{\text{u}}} + \frac{1}{Q_{\text{r}}} + \frac{1}{Q_{\epsilon}}. \quad (2.68)$$

An estimate of the quality factor of the resonator with sample can be computed through the expression

$$Q = \frac{\nu}{\Delta\nu}, \quad (2.69)$$

where  $\nu$  is the microwave frequency and  $\Delta\nu$  is the width at half-maximum of the cavity resonance curve (Poole, 1983). Cylindrical cavities generally have a significantly higher  $Q_u$  factor than rectangular cavities. It is important to stress here that the sensitivity of the EPR is proportional to the product of the quality factor  $Q$  by the filling factor  $\eta$ , as seen from Equation (2.59). The increase of the sample volume raises the value of the filling factor, whereas,  $Q$  tends to decrease due to the dielectric losses. Thus, the optimum sample size for the highest sensitivity is strongly dependent on the used microwave frequency.

### 2.1.8 DETERMINATION OF SPIN CONCENTRATIONS

The concentration of the paramagnetic species giving rise to a certain EPR signal is frequently the goal of EPR spectroscopists. The intensity of the corresponding EPR signal is dependent on a number of factors (some were already mentioned in Subsection 2.1.6):

1. The population difference  $\Delta n$  between the two states involved in the transition. This value is proportional to the spin concentration  $n$  and is given by the Boltzmann population distribution at the measurement temperature  $T$ . Since the EPR signal is proportional to  $\Delta n$ , low operating temperatures benefit signal enhancement.
2. The transition probability, that is, the square of the matrix element between the initial and the final states of the transition moment operator  $\hat{\mathcal{H}}_1$ . In the absence of power saturation, the transition probability is proportional to  $(g \beta_e B_1)^2$ , see Equation (2.42).
3. The center symmetry (number of equivalent centers), the electron spin, which determines the number of different transitions (fine structure), and the hyperfine interaction that produces a further splitting of every line.
4. The effective magnitude of  $B_1$ , that is, the microwave power at the sample. This requires the knowledge of the applied microwave power  $P_0$ , the quality factor  $Q$ , the filling factor  $\eta$ , and the coupling coefficient, which quantifies the microwave power coupled into the cavity.
5. The modulation frequency  $\nu_m$  and modulation amplitude  $B_m$ .

6. The microwave frequency  $\nu$ .
7. Other spectrometer characteristics, such as magnetic field sweep, gain, number of scans, etc.

In the present work, the concentration of a certain paramagnetic center will be determined by comparing the intensity of its EPR spectrum with that produced by a species with a known concentration. The acquisition parameters of both spectra should be chosen in a way that most of the above mentioned variables are the same. However, in cases where this requirement is not fully achievable one may correct the result by knowing the influence of the particular variable on the EPR signal intensity. For example, a difference in the microwave power  $P_0$  used when detecting the EPR spectra may be corrected, since  $I_{\text{EPR}} \propto \sqrt{P_0}$ , provided that the EPR spectra are obtained under non-saturation conditions. Experimental variables, like the measurement temperature  $T$ , the modulation amplitude and frequency, the filling factor and the quality factor should be the same for the measurements of the spectra of both species, since in the most cases their influence on  $I_{\text{EPR}}$  is very hard to quantify. Due to the fact that the intensity of an EPR signal is proportional to the total amount of spins giving rise to the spectrum, the sample volume must be taken into account.

## 2.2 PHOTOEXCITATION EPR

The basis of the photoexcitation electron paramagnetic resonance technique (photo-EPR) is the detection of EPR upon external illumination of the paramagnetic system. The influence of the photoexcitation may have different natures. For instance, it may promote the system from the ground state, allowing the detection of excited states that are paramagnetic. Alternatively, the illumination may induce ionization, enabling the observation of other paramagnetic charge states of the system under study. The time-dependence of the light-induced changes may be determined by monitoring the time evolution of the intensity of an EPR signal.

### 2.2.1 APPLICATION OF PHOTO-EPR TO POINT DEFECTS

The position of the energy levels belonging to a given defect in the energy gap of a semiconductor is one of the most important parameters of the defect. For paramagnetic centers,

they can be determined by photo-EPR. The photoionization threshold is usually observed through illumination with monochromatic radiation in an appropriate wavelengths range. The application of the photo-EPR technique to the study of ionization processes occurring on localized states in semiconductors was reviewed by Godlewski (1985). When compared to other methods like optical absorption and photoconductivity, the correlation between the spectroscopically identified and characterized defects and their energy levels is the main advantage of the photo-EPR as a tool for the determination of the defect level energies. This technique may provide also additional information on other characteristics of paramagnetic centers, like their aptitude for capturing and recombining charge carriers. Methods which are based on optical excitation (as is the case of the photo-EPR) yield the determination of the optical ionization thresholds of defects, whereas other techniques which induce a thermal stimulation (e.g., deep level transient spectroscopy) lead to the measurement of thermal ionization energies. In general these energies have different values (see Section 2.2.3).

### 2.2.2 ELECTRON-LATTICE COUPLING

In the present work, the photoexcitation applied during a photo-EPR experiment promotes transitions between quantum states of the imperfect crystal whose energy difference is of the order of the eV. In such a case, the contributions of the spin-dependent interactions may be neglected in the Hamiltonian which calculates the energies of the involved states, since the energy splittings they produce are too small to be resolved in the photo-EPR spectra.

In Subsection 2.1.1, the movement of the nuclei were considered as being independent on that of the electrons by making use of the adiabatic approximation (see Equations (2.6) and (2.7)). However, when the electrons are excited from one state to other, the change in the charge distribution forces the atomic vibrations to occur about new equilibrium points. The formalism frequently used for a quantitative treatment of the electron-phonon interaction in optical transitions involving defects is the so-called configuration coordinate (CC) model. Rigorous descriptions of the CC formalism are given elsewhere (Markham, 1959; Keil, 1965; Kelley, 1972).

Due to the mass difference between the nuclei and the electrons the movement of the nuclei is much slower than that of the electrons. So, we may calculate the electronic energies for a fixed nuclei configuration and assume that the electrons respond adiabatically to the movement of the nuclei. The electrons and nuclei are treated separately by neglecting the terms of

the Hamiltonian that differentiate  $\varphi(\mathbf{r}, \mathbf{R})$  with respect to  $\mathbf{R}$ . That is,  $\varphi(\mathbf{r}, \mathbf{R})$  depends only parametrically on  $\mathbf{R}$ . This approximation, usually known as the Born-Oppenheimer approximation, separates the Schrödinger equation into two coupled equations,

$$\left[ \hat{\mathcal{H}}_e + \sum_{l>k} U(\mathbf{R}_l - \mathbf{R}_k) \right] \varphi(\mathbf{r}, \mathbf{R}) = P(\mathbf{R}) \varphi(\mathbf{r}, \mathbf{R}), \quad (2.70)$$

$$\left[ \sum_l -\frac{\hbar^2}{2M_l} \nabla_l^2 + P(\mathbf{R}) \right] \chi(\mathbf{R}) = E \chi(\mathbf{R}). \quad (2.71)$$

The energy eigenvalue  $P(\mathbf{R})$  enters as an adiabatic potential in which the nuclei move.

Let us calculate the energies for transitions from an initial to a final (excited) state assuming that they are orbitally non-degenerate states separated in energy by at least several vibrational quanta. In the harmonic approximation, only contributions of the form  $\frac{1}{2} M \omega^2 Q^2$  are considered in the second term of Equation (2.2). Here,  $M$ ,  $\omega$  and  $Q$  are the mass, angular frequency, and normal mode, respectively. For simplicity, we consider that only one dominant mode of vibration is important. The vibrational potential of the initial state can be considered as being

$$P_i = \frac{1}{2} M \omega^2 Q^2. \quad (2.72)$$

Upon optical excitation by an energy  $E_{\text{opt}}$ , the defect goes from the initial state  $i$  into the final state  $f$ . The potential surface of this state, expanded in the normal mode coordinate of the ground state, may be assumed to have the following dependence:

$$P_f = E_{\text{opt}} + \frac{1}{2} M \omega^2 Q^2 + a Q + b Q^2, \quad (2.73)$$

$$\equiv E_{\text{opt}} + \frac{1}{2} M \left( \omega^2 + \frac{2b}{M} \right) \left( Q + \frac{a}{M \omega^2 + 2b} \right)^2 - \frac{a^2}{2M \omega^2 + 4b}. \quad (2.74)$$

Here,  $a$  and  $b$  represent the strength of the linear and quadratic contributions, respectively. The equilibrium configurational coordinate of the excited vibrational state of the defect is shifted from the value of the initial state by

$$\Delta Q = -\frac{a}{M \omega^2 + 2b}. \quad (2.75)$$

Due to the additional quadratic term ( $b Q^2$ ) the mode vibrates with a new frequency

$$\Omega = \sqrt{\omega^2 + \frac{2b}{M}}. \quad (2.76)$$

However, in cases where this term is negligible we have  $\Omega \approx \omega$ . The change of the equilibrium point implies a relaxation of the system, with an energy release of

$$E_{\text{rel}} = \frac{a^2}{2M \omega^2 + 4b}. \quad (2.77)$$

The strength of the electron-lattice coupling is usually described through the dimensionless Huang-Rhys factor

$$S = \frac{E_{\text{rel}}}{\hbar\Omega} = \frac{a^2}{2M \hbar\Omega^3}, \quad (2.78)$$

so that, Equation (2.74) may be re-written as

$$P_f = E_{\text{opt}} - S \hbar\Omega + \frac{1}{2} M \Omega^2 (Q - \Delta Q)^2. \quad (2.79)$$

Substituting Equations (2.72) and (2.74) in the Hamiltonian (2.71) we obtain the following eigenvalues for the initial and final vibronic states

$$E_i = \left(n + \frac{1}{2}\right) \hbar\omega, \quad (2.80)$$

$$E_f = \left(m + \frac{1}{2}\right) \hbar\Omega + E_{\text{opt}} - S \hbar\Omega. \quad (2.81)$$

The configuration coordinate diagram in Figure 2.6 shows the initial and final state energies, as well as transitions between these states. Such transitions may result from the interaction

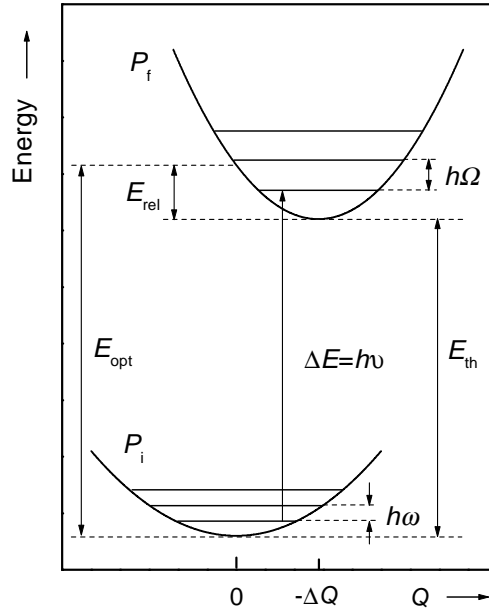


**Figure 2.6:** Configuration coordinate diagram for quadratic mode coupling involving only one vibration mode. The represented transition occurring for excitation with photon energies  $\Delta E = h\nu$ , corresponds to a zero-phonon line observed in optical absorption measurements.

between the defect and electromagnetic radiation. The Frank-Condon approximation neglect

the  $Q$  dependence of the matrix elements of the electromagnetic perturbation between the initial and final states. This results in that the transitions are assumed to be vertical, as shown in Figure 2.6.

### 2.2.3 PHOTOIONIZATION OPTICAL CROSS SECTION

Optical cross sections  $\sigma$  are measured by the excitation of electrons from localized states into the conduction band or from the valence band to a localized state. The photoionization process is described by Fermi's golden rule (Schiff, 1968),

$$\sigma(h\nu) = \left( \frac{\mathcal{E}_{\text{eff}}}{\mathcal{E}_0} \right)^2 \frac{4\pi^2 \hbar^2 \alpha}{3m_0^2 n_r} \frac{1}{h\nu} \sum_f |\langle \psi_f | \mathbf{p} | \psi_i \rangle|^2 \delta[h\nu - (E_f - E_i)], \quad (2.82)$$

where  $\mathbf{p}$  is the electric dipole moment,  $\alpha$  is the fine-structure constant  $e^2/\hbar c$  ( $e$  and  $c$  are the elementary charge and the speed of light, respectively),  $n_r$  is the refractive index of the material and  $h\nu$  is the photon energy.  $\mathcal{E}_0$  is the applied field and  $\mathcal{E}_{\text{eff}}$  is the effective field at the defect site. The wavefunctions of the initial and final states are given by  $\psi_i$  and  $\psi_f$ , respectively, and  $E_i$  and  $E_f$  are their corresponding energies. Thus, to calculate the optical cross section we need to know the initial and final states and their energies, as well as  $\mathcal{E}_{\text{eff}}$ .

The value of  $\mathcal{E}_{\text{eff}}$  is very difficult to determine and is usually adjusted to the experimental values of the optical cross section. Many theoretical studies have been dedicated to the calculation of the shape of  $\sigma(h\nu)$  based on different models of the impurity potential (Stoneham, 1975; Pantelides, 1978; Jaros, 1977; Monemar and Samuelson, 1978; Ridley, 1980; Amato, 1980; Kopylov and Pikhtin, 1974; Piekara *et al.*, 1977; Petit *et al.*, 1986; Delerue *et al.*, 1989). A model which is widely applied to describe the photoionization of deep centers is the one proposed by Lucovsky (1965). Here, the impurity potential is taken as a  $\delta$ -function, rather than the columbic potential of the hydrogenic model for shallow levels, with the electron mass being that of the conduction band. The Lucovsky model is a special case of the more general quantum-defect model proposed by Bebb and Chapman (1967). Applying the result to the calculation of the spectral dependence of the photoionization optical cross section, Lucovsky found the following expression, known as the Lucovsky formula:

$$\sigma_{\text{el}}(E_{\text{opt}}, h\nu) \propto \frac{(h\nu - E_{\text{opt}})^{\frac{3}{2}}}{(h\nu)^3}, \quad (2.83)$$

where  $h\nu$  is the photon energy and  $E_{\text{opt}}$  is the optical ionization threshold. The subscript in  $\sigma$  means that this is a purely electronic capture radiative cross section. That is, the interaction

between electrons and the lattice is neglected. An approach proposed by Piekara *et al.* (1977) has been successfully applied to describe the electron-phonon coupling in the photoionization of a defect in a crystal (Godlewski, 1985). Due to its simplicity this treatment was used in the present work. In their calculations the authors made use of the configuration coordinate model in order to account for the electron-lattice interaction, i.e., lattice relaxation. The removal/addition of one electron from/to a defect level causes a symmetrical distortion of the lattice around the center due to changes of the charge distribution. Thus, the parabolic potentials of the ground and ionized states are displaced in the configurational space. Although the CC model was originally created for transitions within localized states it is also applicable to transitions between localized states and a continuum of states (Monemar and Samuelson, 1978; Samuelson and Monemar, 1978; Kopylov and Pikhtin, 1974; Piekara *et al.*, 1977). The formula of the broadened optical cross section deduced by Piekara *et al.* (1977) using the Born-Oppenheimer and Frank-Condon approximations reads

$$\sigma(h\nu) = \frac{1}{\sqrt{\pi}} \int_{-\beta}^{\infty} dz e^{-z^2} \sigma_{\text{el}}(E_{\text{opt}}, h\nu + \Gamma z) \left(1 + \frac{\Gamma z}{h\nu}\right)^{-1}, \quad (2.84)$$

where

$$\Gamma = \hbar\Omega \sqrt{\frac{2(E_{\text{opt}} - E_{\text{th}})}{\hbar\omega} \coth\left(\frac{\hbar\omega}{2kT}\right)}, \quad (2.85)$$

and

$$\beta = \frac{h\nu - E_{\text{opt}}}{\Gamma}.$$

In these expressions  $\sigma_{\text{el}}$  is the purely electronic optical cross section and  $\omega$  and  $\Omega$  are the phonon frequencies of the ground and excited states, respectively. Other symbols are explained in Figure 2.6. This model predicts a change of the shape of  $\sigma(h\nu)$  via the temperature. Using different experiments, two ionization energies can be measured: the optical ionization energy  $E_{\text{opt}}$  and the thermal ionization threshold  $E_{\text{th}}$ . The difference between these energies is proportional to the lattice relaxation energy  $E_{\text{rel}}$ .

### 2.3 3d IONS IN SEMICONDUCTORS

Transition metals belonging to the iron group have partly-filled 3d shells, with electronic configurations  $3d^1 4s^2$  to  $3d^9 4s^2$ . Defects produced by transition metals in semiconductors

have been extensively studied both experimentally and theoretically. A theoretical model describing the electronic properties of transition metal impurities was proposed by Ludwig and Woodbury (1962). The model was originally created to explain transition metal defects in silicon (Ludwig and Woodbury, 1960). It has been also applied for describing 3d ions in diamond (Isoya *et al.*, 1990*a,b*; Nadolinny *et al.*, 1999; Mason *et al.*, 1999; Twitchen *et al.*, 2000). The model predicts that at the interstitial non-bonding site the 4s electrons of free ions having an electronic configuration  $3d^n 4s^m$  are transferred to the 3d shell and the electronic configuration becomes  $3d^{n+m}$ . In a cubic crystal field the five 3d states are split according to the  $e$  and  $t_2$  irreducible presentations of the cubic group (Abragam and Bleaney, 1970). The threefold-degenerate  $t_2$  states lie lower in energy, as it is likely that the octahedral crystal field from the next-nearest neighbors be stronger than the tetrahedral field from the nearest neighbors,  $\Delta > 0$  ( $\Delta$  is the energy difference between the  $t_2$  and  $e$  states). At the substitutional site the ions are expected to have a configuration  $3d^{n+m-4}$ , since the 4s electrons are added to the 3d shell and four electrons are required to complete the tetrahedral bonding to the four neighbors. The tetrahedral field of the nearest neighbors split the 3d states into the subsets  $e$  and  $t_2$ , with  $e$  being lower in energy,  $\Delta < 0$ . The filling of the one-electron 3d states is shown schematically in Figure 2.7. Ludwig and Woodbury (1960) proposed that for silicon the filling of the levels should be made in a way that the system have a maximum spin consistent with the Hund's rule in free atoms. This is the weak crystal field limit, i.e, the electron-electron interaction dominates over the cubic field splitting  $\Delta$ . Alternatively, cases with strong cubic field favor configurations where the higher energy orbitals are only occupied when the lower energy ones are completely filled. This corresponds to the low spin configuration. It is not yet established whether the weak- or strong-field coupling schema apply for 3d elements in diamond. Up to now, there is only the example of substitutional  $\text{Ni}^-$  with the  $3d^7$  configuration giving rise to a spin of  $S = \frac{3}{2}$  for both approximations.

Another description of the substitutional transition element impurities near the end of the  $d$  series in silicon has been proposed by Watkins (1983). In this theory, named the vacancy model, the substitutional transition metal ion is placed in a vacancy. The 3d states of the transition element interact with the vacancy  $t_2$  gap states, which result from the vacancy dangling bonds. This weak admixture of the  $d$  states of the transition ion with  $t_2$  symmetry with the  $t_2$  states of the vacancy, results in the formation of  $t_2$  bonding states in the valence band and  $t_2$  antibonding states in the energy gap. Therefore the  $t_2$  states in the gap have

Ion	Interstitial (octahedral)		Substitutional (tetrahedral)		
	Cr <sup>+</sup> , Mn <sup>2+</sup>	Ni <sup>+</sup>	Mn <sup>2-</sup>	Ni <sup>-</sup>	Ni <sup>2-</sup>
Configuration	3d <sup>5</sup>	3d <sup>8</sup>	3d <sup>5</sup>	3d <sup>7</sup>	3d <sup>8</sup>
	t <sub>2</sub> <sup>3</sup> e <sup>2</sup>	t <sub>2</sub> <sup>6</sup> e <sup>3</sup>	e <sup>2</sup> t <sub>2</sub> <sup>3</sup>	e <sup>4</sup> t <sub>2</sub> <sup>3</sup>	e <sup>4</sup> t <sub>2</sub> <sup>4</sup>
Spin	5/2	1/2	5/2	3/2	1

**Figure 2.7:** Energy level scheme of  $3d$  ions as predicted by the Ludwig-Woodbury model. The ions shown are merely indicative examples that would be explained by the model.

nearly pure vacancy character. According to the vacancy model a substitutional nickel in the charge states Ni<sup>+</sup>, Ni<sup>0</sup>, and Ni<sup>-</sup> are expected to have structure resulting from symmetry-lowering Jahn-Teller distortions identical to the experienced by the same charge states of the single vacancy (V<sup>+</sup>, V<sup>0</sup>, and V<sup>-</sup>). In silicon, both the negatively charged vacancy V<sup>-</sup> and the substitutional Ni<sup>-</sup> defects have orthorhombic symmetry and spin  $S = 1/2$  (Watkins and Williams, 1995). The only well known nickel defect in diamond is substitutional nickel in the negative charge state. This center retains the  $T_d$  symmetry and has effective spin  $S = 3/2$ . In diamond, the ground state of V<sup>-</sup> is found to be an orbitally nondegenerate  $^4A_2$  state (electronic configuration  $a_1^2t_2^3$ ), that is not subjected to Jahn-Teller distortions (Isoya *et al.*, 1992). Both the Ludwig-Woodbury model and the vacancy model can be used to explain the behavior of this defect. One of the major differences between them is based on the fact that the vacancy model predicts that the unpaired electrons are primarily located in the partially filled antibonding orbitals which are similar to the dangling bonds of the vacancy, whereas in the Ludwig-Woodbury model the  $sp^3$  bonds are full-filled with electrons transferred from the  $3d$  orbitals and unpaired electrons are regarded as associated with the  $3d$  ion.

## 2.4 INFRARED VIBRATIONAL SPECTROSCOPY

Infrared radiation covers the  $10\text{-}10^4\text{ cm}^{-1}$  region of the electromagnetic spectrum. Among the applications of the infrared spectroscopy for studying semiconductors are the determination of band gap energies, impurity type and concentration, carrier density and mobility, sample resistivity, and layer thickness. In the silicon industry, it has been successfully applied in the measurement of the concentration of interstitial oxygen. In this work, this technique is used as a valuable method of measuring impurity concentrations.

### 2.4.1 LATTICE VIBRATIONS

The lattice of a semiconductor supports characteristic vibrational modes whose frequency-wavenumber relation can be calculated from classical solutions of the atomic motion equations. This formalism assumes that the atoms are linked by spring-like restoring forces, yielding normal modes that are either optic or acoustic (Kittel, 1996). In optical modes the atoms of opposite charge vibrate out of phase to give an oscillating dipole moment which interacts with infrared light. However, it is often necessary to treat the lattice vibrations as quantized entities. Phonons are quanta of mechanical lattice waves which are identified by their angular frequency  $\omega$  and wavevector  $\mathbf{k}$ , possessing energy  $\hbar\omega$  and momentum  $\hbar\mathbf{k}$ . The excitation of phonons in a perfect crystal originates an infrared absorption spectrum which reflects the density of phonon states.

An impurity atom destroys the translational symmetry of the lattice, changes the vibrational behavior of its environment, and leads to new vibrational modes. Any new mode may overlap with existing modes of the perfect crystal (resonant modes), yielding changes in the vibration density of states, or appear in spectral regions whose frequencies are forbidden for the intrinsic material (localized modes), which means that such vibrational modes cannot propagate through the crystal. There are two classes of localized modes. These are, the local modes which lie above the maximum frequency (Raman frequency  $\nu_{\text{Raman}}$ ) allowed by the non-perturbed crystal, and the gap modes which appear within forbidden regions of the phonon density of states. It is not possible to have gap modes in diamond, since the phonons are continuously allowed for frequencies  $0 \leq \nu \leq \nu_{\text{Raman}}$ , with  $\nu_{\text{Raman}} = 1332\text{ cm}^{-1}$ .

### 2.4.2 INFRARED SPECTRUM

The absorption and emission of phonons, occurring by interaction of electromagnetic radiation with lattice vibrations, requires the existence of dipolar moments in the crystal. Due to the translational symmetry, the condition of wavevector  $\mathbf{k}$  conservation must be satisfied. The resonance absorption occurs through the excitation of phonons with  $|\mathbf{k}| \approx 0$  in view of the long wavelengths of the relevant infrared electromagnetic radiation. The electric dipole moment  $\mathbf{p}$  induced by a group of atoms oscillating about their equilibrium positions with a normal mode  $Q$ , can be expanded in a Taylor series of  $Q$ ,

$$\mathbf{p} = \mathbf{p}_0 + \left( \frac{d\mathbf{p}}{dQ} \right)_0 Q + \left( \frac{d^2\mathbf{p}}{dQ^2} \right)_0 Q^2 + \dots, \quad (2.86)$$

where  $\mathbf{p}_0$  is the dipole moment which is independent from the vibrational spectra. The derivatives are to be taken at the equilibrium position. The second term defines infrared absorption spectra of first order. The infrared absorption through one-phonon excitation is forbidden in monatomic homopolar crystals like diamond (Lax and Burstein, 1955). The intrinsic infrared absorption of diamond is due to multi-phonon processes (Ramdas, 2001).

The probability  $W$  of an electric dipole transition from an initial state  $|i\rangle$  to a final state  $|f\rangle$  is proportional to,

$$W \propto |\langle i | \hat{\mathbf{e}} \cdot \mathbf{p} | f \rangle|^2 \delta[h\nu - (E_f - E_i)], \quad (2.87)$$

where  $\hat{\mathbf{e}}$  is polarization direction of the external electric field,  $h\nu$  is the photon quanta, and  $(E_f - E_i)$  is the difference in energy between the two states. Only odd terms from Equation (2.86) will contribute to a non-zero transition probability. The absorption coefficient  $\alpha$  is the energy per time and per volume that is removed from a light beam with unitary intensity. If the light absorption is due to centers with concentration  $N$ , it comes

$$\alpha(v) = \frac{WN}{N_{\text{ph}}c}, \quad (2.88)$$

where  $N_{\text{ph}}$  is the number of photons per volume and  $c$  is the velocity of light. The absorption coefficient has units of  $\text{cm}^{-1}$ , and is the quantity that is measured during an optical absorption measurement. This consist on the determination of the relation between the intensity of the incident beam  $I_0(v)$  and that transmitted by the sample  $I(v)$ , as a function of the photon frequency. This ratio depends on the absorption coefficient as

$$\frac{I(v)}{I_0(v)} = \frac{(1 - R)^2 e^{-\alpha d}}{1 - R^2 e^{-2\alpha d}}, \quad (2.89)$$

with  $d$  being the sample thickness, if we take into account that a fraction of radiation  $R$  is reflected in each interface. The integrated absorption of a non-degenerate mode with effective mass  $m$  is

$$\int \alpha(\nu) d\nu = \frac{\pi e^2 \hbar}{2\epsilon_0 m c} N f, \quad (2.90)$$

where  $f$  is called the oscillator strength. The amplitude of a local vibrational mode line is expected to be proportional to the concentration of defects which induce this mode. Each type of infrared active defect in a sample contributes to the observed absorption. If  $\alpha_i(\nu)$  is the absorption coefficient at the frequency  $\nu$  per concentration unit of the defect  $i$ , the total absorption is

$$\alpha_T(\nu) = \sum_i c_i \alpha_i(\nu), \quad (2.91)$$

where  $c_i$  is the concentration of centers  $i$ .



# CHAPTER 3

## SAMPLE CHARACTERIZATION

### 3.1 INTRODUCTION

The present work is focused on the study of single crystal diamonds grown at high pressure and high temperature (HPHT) from Ni-containing solvent / catalysts. As pointed out in Section 1.5, diamonds are classified through the amount and the form of nitrogen that they incorporated. Nitrogen present in diamond induces absorption in the one-phonon region of the IR absorption spectra. The different forms of nitrogen incorporation give rise to characteristic spectra, which can be used to estimate the concentration of nitrogen impurities (Lawson *et al.*, 1998), see Section 1.5. To attain a rough characterization of the crystals, optical absorption measurements in the IR region were performed and the concentration of nitrogen defects determined.

An important characteristic of HPHT diamond grown from Ni solvents is the amount of nickel incorporated as a dispersed impurity. Substitutional nickel in the negative charge state  $\text{Ni}_\text{s}^-$  is responsible for the well known W8 EPR signal. In the context of characterization of the crystals, EPR spectra were measured to determine the concentration of  $\text{Ni}_\text{s}^-$  centers. Such measurements led to the estimation of the amount of nickel incorporated during the synthesis of the crystals.

### 3.2 DIAMOND SAMPLES

In Table 3.1, a representative set of HPHT diamonds selected from the studied group of samples is listed. The crystals were supplied by Dr. Hisao Kanda from the National Institute for

**Table 3.1:** Representative set of diamonds used in this study and composition of the solvent metals used in their synthesis at HPHT. Subscripts represent the weight percentage of the components of the metal solvent alloys. Two of the crystals (F and G) were subjected to an annealing after the growth.

Sample	Solvent metal	Post-growth treatment
A	Ni	
B	Ni	
C	Ni	
D	Ni	
E	Ni	
F	Ni	6 GPa, 1600°C, 4 hours
G	Ni	6 GPa, 1600°C, 4 hours
H	Ni <sub>0.8</sub> -Fe <sub>0.2</sub>	
I	Ni <sub>0.8</sub> -Fe <sub>0.2</sub>	
J	Ni <sub>0.98</sub> -Ti <sub>0.02</sub>	
K	Ni <sub>0.98</sub> -Ti <sub>0.02</sub>	
L	Ni-Fe-Ti-Al	

Research in Inorganic Materials (NIRIM), Japan, through a collaboration between NIRIM and the Department of Physics of the University of Aveiro. The samples were grown by the temperature gradient method at temperatures in the range 1400-1500°C under an hydrostatic pressure of about 6 GPa. The growth temperatures were within the range 1400 – 1500°C. All samples were grown from a seed crystal using a solution of carbon and a nickel-containing catalyst. A small amount of Ti was added to the metal solvent when growing samples J and K. Nitrogen getters, like Ti and Al, are normally used to synthesize diamond with low concentration of nitrogen impurities. Samples F and G suffered a post-growth heat treatment for 4 hours at 1600°C under a stabilizing hydrostatic pressure of 6 GPa. This heat treatment was performed in the same equipment as used to grow the crystals. Samples D to G were mechanically polished into a parallelepiped shape with edges of  $\sim 1$  mm length and with faces parallel to  $\{110\}$  and  $\{100\}$  crystallographic planes.

### 3.3 INFRARED ABSORPTION SPECTRA

Infrared absorption spectra were measured on a Bruker IFS66V Fourier-transform spectrometer at the Department of Physics of the University of Aveiro. This system is equipped with a Ge/KBr beam splitter, a globar as light source and a silicon detector. The spectrometer includes a data acquisition and a computer based analysis system. The equipment covers the range from  $400 - 4800 \text{ cm}^{-1}$  at  $0.24 \text{ cm}^{-1}$  resolution. All spectra were recorded at room temperature. The infrared spectra intensity were calibrated through the absorption value at  $2000 \text{ cm}^{-1}$ , which is known to be  $12.3 \text{ cm}^{-1}$  for all diamonds (Davies, 1977*b*).

A typical IR absorption spectrum obtained for the sample A is shown in Figure 3.1. Isolated

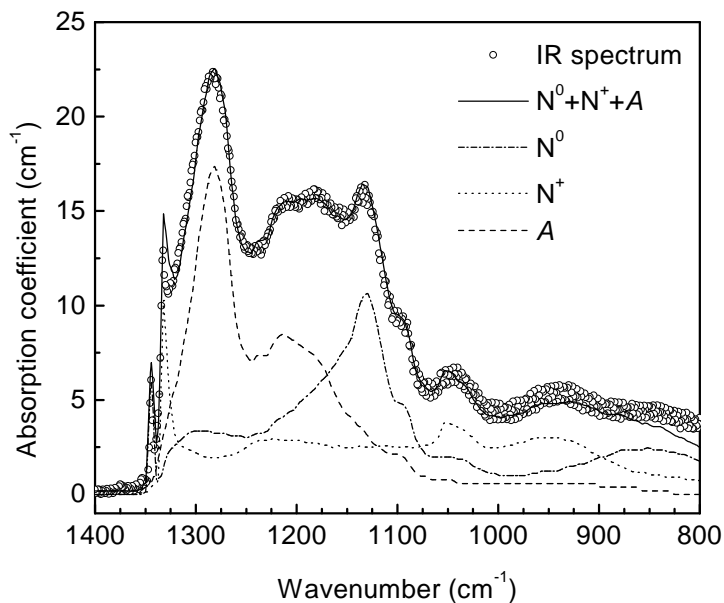


**Figure 3.1:** IR absorption spectrum of sample A measured at room temperature. The spectrum is a mixture of the components of the  $N^0$ ,  $N^+$ , and  $A$  aggregates.

substitutional nitrogen, in the neutral and positively charged states, as well as nitrogen aggregates ( $A$  centers) induce characteristic absorption in the one-phonon region. The spectrum in Figure 3.1 is an admixture of these individual components and was reconstructed using numerical minimization techniques. The concentrations of the different forms of nitrogen in the samples were determined using the relationships between the nitrogen concentration and infrared absorption coefficients given in Table 1.2.

The values of the nitrogen concentrations obtained in this way are shown in Table 3.2. Diamond samples A to I exhibit an high amount of nitrogen in the form of dispersed substitutional centers and *A* aggregates. Normally, in as-grown HPHT diamonds nitrogen is mainly incorporated in the single substitutional forms  $N^0$  and  $N^+$ . The presence of a significant amount of *A* defects in as-grown samples shows that nitrogen aggregation took place during growth. This process is stronger for increasing growth temperatures (Kupriyanov

**Table 3.2:** Concentrations of the main impurity-related defects in HPHT diamond grown with Ni-containing solvents determined from IR absorption spectroscopy. The concentrations of the  $N_s^-$  center were determined with EPR using the concentration of  $N_s^0$  centers (P1 EPR spectrum) measured by IR absorption as calibration.

Sample	Solvent metal	Concentration (ppm) $\pm 20\%$				
		$N_s^0$	$N_s^+$	<i>A</i>	<i>B</i>	$N_s^-$
A	Ni	263	57	285	0	62
B	Ni	191	39	119	1	36
C	Ni	185	40	80	1	42
D	Ni	205	69	32	0	150
E	Ni	213	54	102	0	133
F	Ni	77	26	249	2	47
G	Ni	82	23	254	1	38
H	Ni <sub>0.8</sub> -Fe <sub>0.2</sub>	205	42	73	0	16
I	Ni <sub>0.8</sub> -Fe <sub>0.2</sub>	124	27	48	0	13
J	Ni <sub>0.98</sub> -Ti <sub>0.02</sub>	10	7	0	0	3.1
K	Ni <sub>0.98</sub> -Ti <sub>0.02</sub>	16	9	0	0	2.5
L	Ni-Fe-Ti-Al	< 1	< 1	0	0	< 1

*et al.*, 2001). The deviations observed in the concentration of nitrogen defects in the as-grown samples A to E result from differences in the growth temperature. The concentration of *B* aggregates in the used diamonds was found to be negligible.

The crystals synthesized with the use of nitrogen getters (J to L) show a considerably lower concentration of nitrogen impurities. In these crystals, nitrogen is only present in the form

of single substitutional centers in the neutral and positive charge states.

## 3.4 EPR SPECTRA

### 3.4.1 EXPERIMENT

Continuous wave EPR measurements reported in the present work were made at the Department of Physics of the University of Aveiro, Portugal, and at the Institute for Solid State Physics of the Technical University of Berlin, Germany. In both places Bruker ESP 300E spectrometers operating in the absorption mode were used. The equipments were supplied with  $X$ - ( $\nu \sim 9.5$  GHz) and  $Q$ -band ( $\nu \sim 34$  GHz) microwave bridges. In the  $X$ -band, a rectangular  $TE_{102}$  or a cylindrical  $TE_{011}$  microwave resonator were used, whereas the  $Q$ -band measurements were performed using cylindrical cavities operating in the  $TE_{011}$  mode. Measurement temperatures lower than the room temperature were achieved in the  $X$ -band by means of a thermostatted Oxford Instruments ESR 900 helium gas flow cryostat. The system was made up of a vacuum isolated quartz dewar tube inserted through the microwave cavity. Here, the sample temperature was monitored with a AuFe/Ch thermocouple placed at 10 mm down stream from the sample with the reference junction plunged in liquid nitrogen. An overpressure of dry nitrogen stream was maintained within the waveguide and cavity to prevent moisture condensation. For measuring EPR in the  $Q$ -band at cryogenic temperatures, an Oxford Instruments CF935 continuous flow helium cryostat was used. This cryostat was wired with a AuFe(0.07%)/Chromel thermocouple. In the  $X$ - and  $Q$ -band measurements was used an Oxford Instruments ITC automatic temperature controller that regulates the temperature of the gas blowing past the sample with a maximum precision of  $\pm 0.1$  K at 4 K. EPR measurements at cryogenic temperatures required the use of low microwave power to avoid a saturation of the signals owing to the low relaxation rates at this temperature.

The microwave frequency and the static magnetic field were measured by means of Hewlett-Packard frequency counters and a Bruker ER035M NMR gaussmeter, respectively. The NMR probehead was placed close to one of the pole pieces of the magnet at the same height as the resonant cavity. However, there is always a small discrepancy between the magnetic field experienced by the sample and that observed by the NMR sonde. To further minimize errors in the determination of the spin Hamiltonian parameters, the magnetic field value was

corrected making use of  $g$ -standards (like the well known P1 center in diamond).

In the  $X$ -band experiments, the samples were mounted at the bottom of a suprasil synthetic quartz rod which was utilized as sample holder. To measure the crystals in the  $Q$ -band, thin synthetic quartz tubes were used as sample holders. A different quartz tube was made for each sample depending on the dimensions of the crystal. The samples were fixed inside these tubes by the use of a cryogenic glow. The suprasil quartz and glow used to fix the samples to the holders were found to be free of any detectable EPR signal. The samples were oriented with respect to the external magnetic field  $\mathbf{B}$  either using  $\{111\}$  and  $\{100\}$  growth facets or by faces polished parallel to the main crystallographic planes. An one-axis goniometer permitted the rotation of the sample in a plane that contains  $\mathbf{B}$  and that is perpendicular to the axis of the sample holder. In order to guarantee thermal equilibrium in the occupation of the different defect states the EPR measurements were done keeping the samples in dark.

### 3.4.2 RESULTS

The substitutional nitrogen center  $N_s^0$  gives rise to the well known P1 EPR spectrum with a three-line hyperfine structure due to the interaction with a  $I = 1$  nitrogen nucleus, see Figure 3.2. The  $N_s^0$  center is detectable both by EPR and IR absorption. Thus, its concentration determined by the IR absorption, can be used for the determination of the W8 defect concentration by EPR studies. The relative concentrations of the P1 and the W8 paramagnetic defects were determined by comparing the intensity of their EPR spectra. Figure 3.2 shows the EPR spectrum of the sample B, containing the lines of the W8 and P1 centers. In order to avoid any saturation effects, the dependence of the EPR signal intensity  $I_{\text{EPR}}$  on the applied microwave power  $P_0$  was measured for the W8 and P1 spectra. The values of  $I_{\text{EPR}}$  were determined by fitting the lines of the experimental spectra with the first-derivative of Lorentzian functions (see Appendix A). In Section 2.1.8, the main variables which influence the intensity of an EPR line are summarized. As the W8 and P1 lines were always observed upon the same experimental conditions, their intensity ratio is merely due to deviations in the population difference  $\Delta n$  of the states involved in the monitored transitions and also due to transition probability differences.

The W8 line at  $g = 2.032$  corresponds to the transition  $M_S = -\frac{1}{2} \leftrightarrow \frac{1}{2}$  of a  $S = \frac{3}{2}$  system (Isoya *et al.*, 1990b). As  $D \simeq 0$ , the three allowed transitions with  $\Delta M_S = \pm 1$ , shown

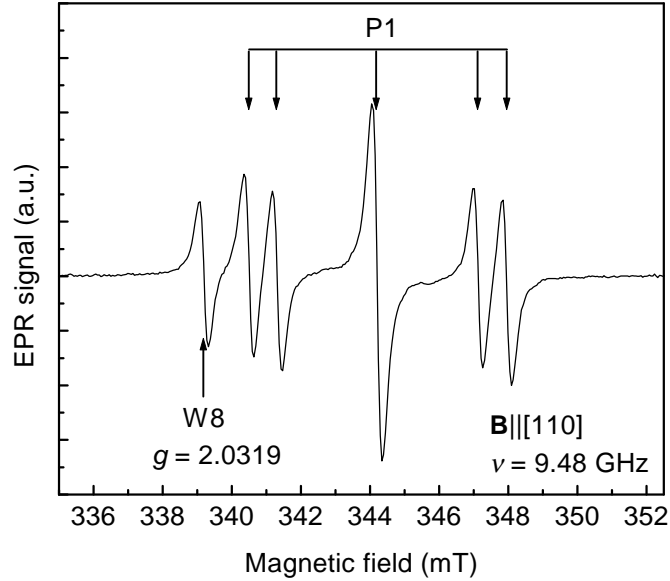


**Figure 3.2:** X-band EPR spectra of the well known P1 and W8 centers measured in sample B. The spectrum was obtained at 50 K with the external magnetic field  $\mathbf{B}$  parallel to an  $\langle 110 \rangle$  direction.

in Figure 2.2, occur at the same magnetic field. However, the transitions  $M_S = \pm\frac{3}{2} \leftrightarrow \pm\frac{1}{2}$  are undetectable due to a random strain induced broadening. As both transitions which are observed in the W8 and P1 centers are of the type  $M_S = -\frac{1}{2} \leftrightarrow \frac{1}{2}$ , their probabilities are equal. Assuming a Boltzmann distribution of the spin levels, we easily obtain that for the used temperatures ( $> 50$  K) the ratio between  $\Delta n$  and  $n$  at the  $M_S = -\frac{1}{2} \leftrightarrow \frac{1}{2}$  transition of the W8 center is approximately one-half of the one that is calculated for the same transition of an  $S = \frac{1}{2}$  system. Thus, to compare the spectral intensity of the W8 with the intensity of the P1, one must divide the latter by two. The concentrations of W8 defects estimated in this manner are shown in Table 3.2.

Crystals synthesized with a pure nickel catalyst exhibit a higher concentration of  $\text{Ni}_s^-$  defects than the samples grown from a nickel-containing alloy. In samples where the concentration of nitrogen defects is considerably lower (J, K, and L), the incorporation of nickel in the form of W8 centers was also observed to be smaller.

Along with the dominant P1 and W8 lines, the EPR spectra of the studied set of samples ev-

identified also the presence of other peaks produced by several nickel-containing paramagnetic defects described in the literature (see Subsections 1.6.1 and 1.7.2). A list of paramagnetic centers detected in the investigated crystals is given in Table 3.3. In the samples D to G the

**Table 3.3:** Paramagnetic centers detected in the set of samples shown in Table 3.1.

Sample	Solvent metal	Paramagnetic centers
A	Ni	P1, W8, AB5, AB1, AB3
B	Ni	P1, W8, AB5, AB1, AB3
C	Ni	P1, W8, AB5, AB1, AB3
D	Ni	P1, W8, NE1, NE2, NE5, AB5, AB1, AB3
E	Ni	P1, W8, NE1, NE2, NE5, AB5, AB1, AB3
F	Ni	P1, W8, NE1, NE2, NE3, AB1-AB6
G	Ni	P1, W8, NE1, NE2, NE3, AB1-AB6
H	Ni <sub>0.8</sub> -Fe <sub>0.2</sub>	P1, W8, AB5
I	Ni <sub>0.8</sub> -Fe <sub>0.2</sub>	P1, W8, AB5
J	Ni <sub>0.98</sub> -Ti <sub>0.02</sub>	P1, W8, NIRIM1, NIRIM2
K	Ni <sub>0.98</sub> -Ti <sub>0.02</sub>	P1, W8, NIRIM1
L	Ni-Fe-Ti-Al	P1, W8

spectra of some of the nickel- and nitrogen-containing defects originally found by Nadolinny *et al.* (1999) were observed. The NE1, NE2 and NE5 centers were detected in samples D and E, whereas in the annealed samples F and G the NE1 to NE3 centers were observed. The EPR spectrum Figure 3.3, obtained from sample F, shows the lines of the NE1 and NE2 paramagnetic centers. The spectra of the  $S = \frac{1}{2}$  nickel-nitrogen complexes were identified through their characteristic angular dependence of the EPR line positions by rotation of the magnetic field in a  $\{110\}$  plane. These angular dependencies were calculated with the spin Hamiltonian

$$\hat{\mathcal{H}} = \beta_e \mathbf{B} \cdot \mathbf{g} \cdot \hat{\mathbf{S}} + \sum_i \hat{\mathbf{S}} \cdot \mathbf{A}_i \cdot \hat{\mathbf{I}}_i, \quad (3.1)$$

and the  $g$ -values and hyperfine parameters  $\mathbf{A}_i$  given by Nadolinny *et al.* (1999) for the observed interaction with the involved  $^{14}\text{N}$  nuclei ( $I = 1$ ). The hyperfine interaction with the different nuclei and the low point symmetry (monoclinic or triclinic) of the centers produce

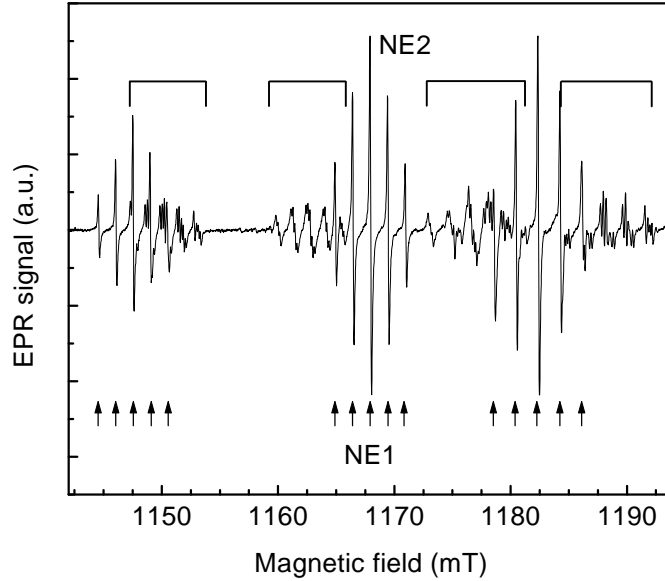


**Figure 3.3:** Section of the  $Q$ -band EPR spectrum of sample F showing lines of the NE1 and NE2 centers. The lines were recorded at room temperature with  $\mathbf{B}$  along a  $\langle 110 \rangle$  direction.

complex spectra. The observed formation of these centers upon high temperature annealing was interpreted by Nadolinny *et al.* (1999) as being due to aggregation of nitrogen to a nickel defect. The authors argue that the nickel center to which nitrogen migrates is the paramagnetic NE4 defect with trigonal symmetry (Nadolinny and Yelissev, 1994; Nadolinny *et al.*, 1997). We failed to observe any EPR signal from NE4 centers in all the studied as-grown and annealed diamond samples, though the nickel-nitrogen complexes NE1-NE3 and NE5 were detected in a number of these samples. Among which the samples D to G of Table 3.3 are representative examples. In spite of this, the detection of some of the nickel-nitrogen defects in the annealed samples F and G corroborates the statement of Nadolinny *et al.* (1999) that these centers are produced upon high temperature annealing of HPHT diamond. However, we believe that the defect which originates the formation of the nickel-nitrogen paramagnetic complexes is still unknown. Further studies must be carried out to attain an unambiguous determination of the precursor of these centers in diamond. The detection of nickel-nitrogen defects in the as-grown samples D and E shows that the nitrogen aggregation process occurred during the growth of these crystals. This argument is supported by the observation of aggregated nitrogen defects ( $A$  centers) in the same as-grown samples (D and

E). The aggregation mechanism took place probably due to a slightly higher temperature used to synthesize these crystals. In the same crystals, the concentration of W8 defects is considerably higher than in the other as-grown crystals. This indicates that the formation of nickel-nitrogen complexes during the growth process is more likely in crystals exhibiting an higher amount of incorporated nickel.

As previously observed by Isoya *et al.* (1990b), the NIRIM1 and NIRIM2 defects were detected in samples grown with the addition of a nitrogen getter to the solvent / catalyst. The EPR spectrum NIRIM1 consists of a single isotropic line at  $g = 2.0112$  when measured at temperatures higher than 20 K. The NIRIM2 spectrum was identified through its characteristic trigonal angular dependence upon rotation of the external magnetic field.

The  $X$ - and  $Q$ -band EPR spectra of our crystals have shown in addition to the EPR centers described in the literature some new line sets. A detailed study of these lines revealed that they are induced by six defects, which in the tradition of naming EPR centers in diamond were labeled as AB1 to AB6 (**A**veiro-**B**erlin). The occurrence of these defects in the various samples is listed in Table 3.3. A detailed description of the paramagnetic properties of these defects is given in Chapter 4.

# CHAPTER 4

## THE AB PARAMAGNETIC CENTERS

### 4.1 INTRODUCTION

As a consequence of the typical small spin-orbit coupling observed for impurities in diamond, many centers have EPR transitions near to the free electron  $g$ -value  $g_e$  (Baker and Newton, 1994). This makes their differentiation difficult, especially using low microwave frequencies, since the transitions of the different centers overlap very strongly. Carefully controlled experiments at different microwave frequencies ( $X$ - and  $Q$ -band) and appropriate choice of microwave power and sample temperature enabled the detection of six new paramagnetic defects, named AB1 to AB6 (AB centers), in the studied crystals (Neves *et al.*, 1999*b*, 2000; Pereira *et al.*, 2002*b*). A detailed analysis of the EPR spectra of the newly found centers is given in this chapter. The spins and symmetries of the AB centers were established through the investigation of the anisotropic properties of their EPR spectra. The involvement of nickel in the structure of these paramagnetic centers is putted forward. In addition, the processes which would lead to the formation of the new paramagnetic centers are discussed and some plausible models are proposed.

### 4.2 CENTERS AB1 AND AB3

#### 4.2.1 EPR SPECTRA OF THE AB1 AND AB3

Figure 4.1 shows two EPR spectra of sample B obtained with the external magnetic field  $\mathbf{B}$  parallel to the main crystallographic directions  $[110]$  (a) and  $[001]$  (b). The main features of

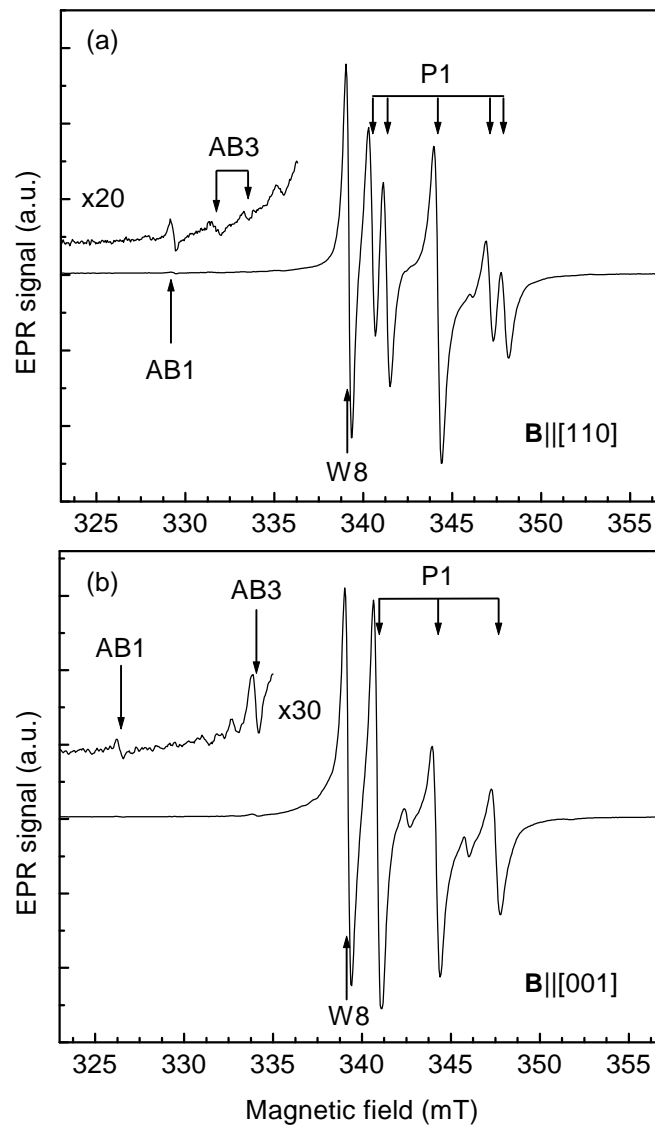


**Figure 4.1:** EPR spectra of sample B measured in the X-band at 50 K with  $\mathbf{B}$  along the directions [110] (a) and [001] (b). The EPR lines of the new AB1 and AB3 centers appear when a relatively high microwave power ( $> 0.5$  mW) is used. At such microwave power levels the P1 and W8 lines are measured upon saturation conditions.

the spectra are the typical P1 lines and the  $g = 2.0319$  line of the  $\text{Ni}_g^-$  center. In addition, several small unidentified lines with low intensity were observed. These lines are labeled AB1 and AB3 in the spectra of Figure 4.1. The AB1 and AB3 lines were only observed at temperatures lower than 150 K. Below 20 K, saturation effects impaired the observation of

well-resolved spectra, even at the lowest available microwave power of 10 nW. No apparent motional effects or shifts of the EPR line positions could be detected in the temperature range of the experiments. The AB1 and AB3 spectra were observed in some of the as-grown and annealed samples, see Table 3.3.

The dependence of the AB1 and AB3 line positions on the direction of the external magnetic field  $\mathbf{B}$  was observed by recording the EPR spectrum for discrete orientations of  $\mathbf{B}$  in the  $(1\bar{1}0)$  plane, going from  $[110]$  to  $[001]$  in steps of  $5^\circ$ . In cubic crystals, the anisotropy of EPR spectra is usually studied in a  $\{110\}$  plane, because it embraces the three main crystallographic directions  $\langle 110 \rangle$ ,  $\langle 111 \rangle$ , and  $\langle 001 \rangle$ . In such a way, we can easily determine the principal values of the different tensors contained in the spin Hamiltonian from a direct inspection of the angular plot of the EPR line positions (see the example of Subsection 2.1.5). Figure 4.2 shows the angular variation of the positions of the AB1 and AB3 EPR lines measured in this way. The data were obtained from  $Q$ -band measurements, making use of the better resolution achieved with an higher frequency. The two sets of lines have shown a distinct saturation behaviour, proving that they belong to spin transitions of two different centers (see Subsection 2.1.6). Analyzing the simultaneously measured angular dependence of the well known P1 hyperfine structure, a small misorientation by  $2^\circ$  of the  $[1\bar{1}0]$  rotation axis was determined. The angular dependence of the AB1 and AB3 spectra are typical of  $S = \frac{1}{2}$  systems with trigonal and orthorhombic-I symmetry, respectively. The line positions can be well described with the spin Hamiltonian

$$\hat{\mathcal{H}} = \beta_e \mathbf{B} \cdot \mathbf{g} \cdot \hat{\mathbf{S}}, \quad (4.1)$$

with  $S = \frac{1}{2}$  and using the  $g$ -values given in Table 4.1. For a rotation of the magnetic field  $\mathbf{B}$  in a  $\{110\}$  plane, the  $g$ -values of the spin Hamiltonian (4.1) have the following angular dependence:

$$g^2 = \left[ \frac{1}{2}(\mathbf{g}\mathbf{g})_{xx} + (\mathbf{g}\mathbf{g})_{xy} + \frac{1}{2}(\mathbf{g}\mathbf{g})_{yy} \right] \sin^2 \theta + \sqrt{2} [(\mathbf{g}\mathbf{g})_{xz} + (\mathbf{g}\mathbf{g})_{yz}] \cos \theta \sin \theta + (\mathbf{g}\mathbf{g})_{zz} \cos^2 \theta, \quad (4.2)$$

since  $\phi = \pi/4$  in Equation (2.47). The peak-to-peak linewidth  $\Delta B_{\text{pp}}$  of the spectral lines is about 0.3 mT at 70 K. The overlapping of the lines and their small intensity did not allowed a reliable quantification of possible changes of  $\Delta B_{\text{pp}}$  with the direction of  $\mathbf{B}$ . No sensitive change of the linewidth was observed by detecting the lines using different microwave frequencies, i.e., in the  $X$ - and  $Q$ -band.

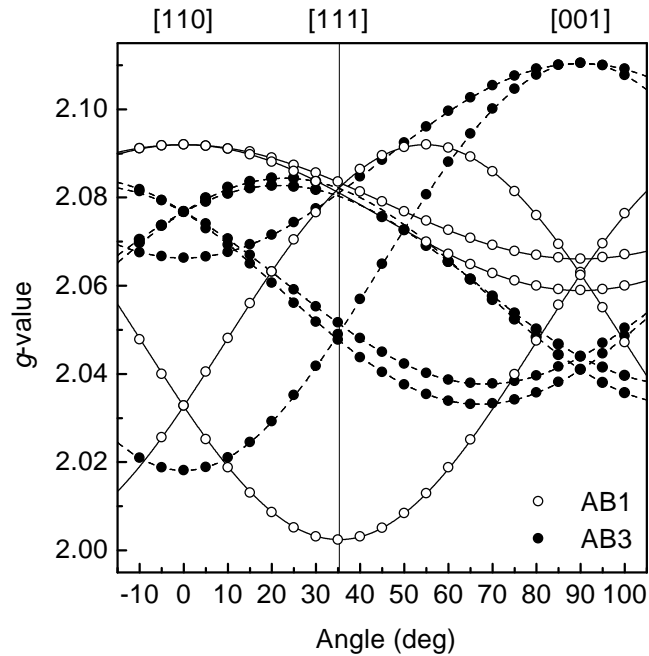


**Figure 4.2:** Angular dependence of the AB1 ( $\circ$ ) and AB3 ( $\bullet$ ) EPR line positions upon rotation of the magnetic field in a plane very close to  $(1\bar{1}0)$ . The zero angle correspond to the direction  $[110]$ . The open points represent the experimental data and the solid lines are angular dependencies calculated from the spin Hamiltonian (4.1) using the parameters given in Table 4.1.

As mentioned in Section 1.6, Pawlik *et al.* (1998) studied the defect responsible for the MCDA doublet at 1.72 eV using the ODEPR technique and assigned this trigonal defect to the NE4 center (Nadolinny and Yelisseyev, 1994). In Table 4.1, the  $g$ -values found for the 1.72 eV system together with the values reported by Nadolinny and Yelisseyev (1994) for the NE4 center are listed. Comparing the  $g$ -values of the trigonal centers AB1 and NE4 with the values determined from the angular dependence of the ODEPR measurements we see that the AB1 data approach the  $g$ -values of the 1.72 eV band much better than the values published for the NE4 center. This suggests that the 1.72 eV doublet is not produced by internal electronic transitions occurring in the NE4, but is related to transitions in the AB1 center.

**Table 4.1:**  $g$ -values and center symmetries for the AB1 and AB3 centers with  $S = 1/2$ . For comparison the data for the 1.72 eV MCDA doublet (Pawlik *et al.*, 1998) and for the NE4 center (Nadolinny and Yelisseyev, 1994; Nadolinny *et al.*, 1997) are also shown.

Center	Symmetry	Spin	$g$ -values	$\Delta B_{pp}$ (mT)
AB1	Trigonal	$\frac{1}{2}$	$g_{\parallel} = 2.0029(3) \parallel [111]$ $g_{\perp} = 2.0925(3) \perp [111]$	$0.30 \pm 0.05$
AB3	Rhombic-I	$\frac{1}{2}$	$g_1 = 2.1113(3) \parallel [001]$ $g_2 = 2.0671(3) \parallel [110]$ $g_3 = 2.0189(3) \parallel [1\bar{1}0]$	$0.30 \pm 0.05$
1.72 eV	Trigonal	$\frac{1}{2}$	$g_{\parallel} = 2.004(5) \parallel [111]$ $g_{\perp} = 2.093(5) \perp [111]$	–
NE4	Trigonal	$\frac{1}{2}$	$g_{\parallel} = 2.0227 \parallel [111]$ $g_{\perp} = 2.0988 \perp [111]$	not supplied

#### 4.2.2 NATURE OF THE AB1 AND AB3 CENTERS

Some of the power of the EPR technique comes from the possibility of achieving a clear identification of the atomic species involved in a given paramagnetic system. However, this is only possible in cases where the hyperfine structure of the spectrum gives an unambiguously fingerprint. The lack of any resolved hyperfine structure in the AB1 and AB3 spectra prevents such direct identification of the chemical nature of these defects. However, there are some facts which allows a tentatively assignment.

Because these defects are observed in high temperature treated samples it can be excluded that they are formed by intrinsic defects only. Annealing studies of electron irradiated pure diamonds (natural type II) have shown that, the large number of intrinsic defects produced by the electron irradiation can be almost completely annealed out at temperatures considerably lower than 1400°C (Ammerlaan, 1990).

Unlike most of the paramagnetic defects in diamond, the  $g$ -tensor of the AB1 and AB3 defects exhibit a quite large deviation  $\Delta g = g - I g_e$  from the free electron value ( $g_e = 2.002319$ ), with  $I$  being the unit matrix. Such deviation results from an admixture, via the spin-orbit interaction  $\lambda \mathbf{L} \cdot \mathbf{S}$ , of the excited states at energy  $\Delta$  from the ground state.

It is shown that this deviation is approximately given by  $\Delta g \sim -\lambda/\Delta$  for singlet orbital ground states (see Section 2.1.2). Moreover, it is found that the spin-orbit parameter  $\lambda$  is relatively large for transition metal ions (see for instance the Tables 7.6 and 7.7 given in the book of Abragam and Bleaney (1970)). Furthermore, the  $g$ -values measured for the defects in diamond which have been unambiguously identified as being related to transition metals in diamond, namely, the Ni-related center W8 (Samoilovich *et al.*, 1971) and the Co-containing defect O4 (Twitchen *et al.*, 2000), are found to be strongly deviated from  $g_e$ . Hence, the  $g$ -values measured for the AB1 and AB3 centers indicate that a transition metal is a likely constituent of these defects. This conclusion is also motivated by the fact that, the magnitude of the departures of  $g$  from the free electron value  $g_e$  observed here for the AB1 and AB3 paramagnetic centers have the same order of magnitude as those determined for other transition metal related defects in semiconductors (Pilbrow, 1990).

The lack of any hyperfine structure in the spectra limits the possibilities to the elements with an high natural abundance of isotopes with  $I = 0$ , namely, Ti, Cr, Fe, Ni, and Zn. The sign of the deviation  $\Delta g$  observed in the  $g$ -values of the AB1 and AB3 centers shows that  $\lambda < 0$ . A positive spin-orbit term is indicative of a transition metal ion having a more than half-filled  $d$ -shell (Abragam and Bleaney, 1970). Thus, we may exclude titanium and chromium. Moreover, the incorporation of these elements into diamond is less probable owing to their large atomic radii (Winter, 2002). Since the AB1 and AB3 centers appeared in diamonds grown from Ni-containing catalysts, it is reasonable to assume that the transition metal involved in them is nickel.

The observed magnitudes and symmetries of the crystal field distortions suggest an association of a nickel ion in substitutional or interstitial site with other defects. These defects may be vacancies, interstitials, and/or impurities. The narrow lines of the AB1 and AB3 spectra suggest a possible association of nickel with an atom without nuclear spin. For example, oxygen is an element with a nearly 100% abundant isotope of spin  $I = 0$ , which is known to be present in diamond in relatively high concentrations (Sellschop, 1992). However, oxygen seems to be somehow hidden in the lattice, as it was never detected as a constituent of any point defect in diamond. Alternatively, the impurity involved may have an abundant isotope with non-zero nuclear spin, but then the hyperfine parameter  $A$  should be very small. In this situation, an obvious candidate is nitrogen, since it is found in high concentrations in the studied samples. If nitrogen is directly involved in the AB1 and AB3 centers, it would

produce an hyperfine structure in the EPR spectra, resulting from the coupling between the spin of the unpaired electron and the nuclear spin of  $^{14}\text{N}$  ( $I = 1$ , natural abundance 99.63%). Taking into account the linewidths of the AB1 and AB3 EPR lines (see Table 4.1), we assume that such a structure would be resolved in the spectra for hyperfine parameters greater than  $A_{\min} \sim 7$  MHz. All the known nickel-nitrogen complexes in diamond have  $A$ -values for neighboring  $^{14}\text{N}$  atoms considerably higher than this value (Nadolinny *et al.*, 1999). Only for one of the three nitrogen atoms of the NE2 center these values are of the same order of magnitude as  $A_{\min}$  (Nadolinny *et al.*, 1999). Thus, if nitrogen is present, the structure of the defects should account for a very small hyperfine interaction with  $^{14}\text{N}$ .

It is interesting to note that the as-grown samples which exhibit the presence of the AB1 and AB3 centers are those samples where the concentration of W8 centers is higher. This shows that the conditions needed during the growth of the crystals to generate the AB1 and AB3 defects in detectable amounts, correspond to those which result in an higher incorporation of W8 centers. Nickel being larger than carbon could act during the crystals synthesis as a center for generation of vacancies and carbon interstitials, which in turn interact with nickel atoms and/or other imperfections to form the observed defects. This means that, the AB1 and AB3 defects are likely complexes of nickel associated with vacancies or self-interstitials.

## 4.3 CENTER AB5

### 4.3.1 THE AB5 SPECTRUM

A new spectrum, labeled AB5, with lines in a very wide magnetic field region was detected in some of the studied samples. The AB5 lines measured with the external magnetic field oriented closely to the main crystallographic directions are shown in Figure 4.3. The spectra were obtained on sample F in the  $Q$ -band at 6 K. At such low temperatures, the AB5 lines exhibit for the available microwave power range a lineshape typical of fast-passage conditions (Weger, 1960), indicating a large spin-lattice relaxation time. The anisotropic properties of the AB5 EPR lines were studied at 6 K to rule out any motional effects. The angular dependence of the EPR line positions measured at  $\sim 34$  GHz is presented in Figure 4.4 for rotation of the external magnetic field in a plane close to  $\{110\}$ . The line

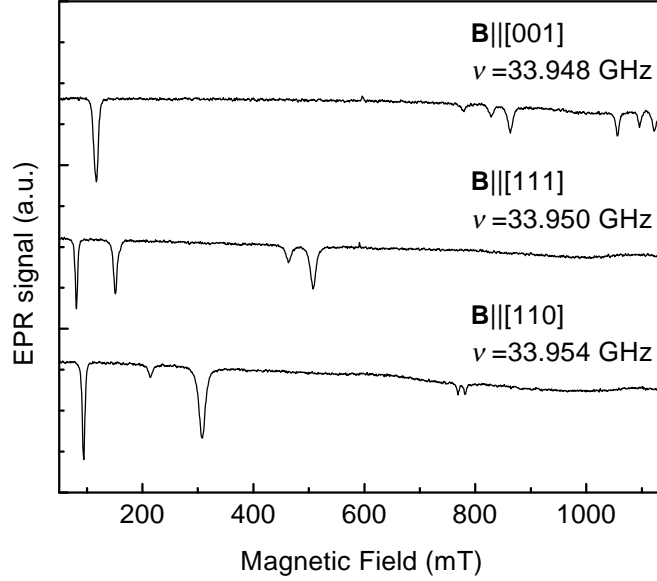


**Figure 4.3:** Wide-scan EPR spectra of sample F showing the presence of the AB5 lines. The spectra were recorded at 6 K in rapid-passage conditions for  $\mathbf{B}$  along the main crystallographic directions (1 mW microwave power, 100 kHz modulation frequency and 0.1 mT modulation amplitude).

positions can be well described by the spin Hamiltonian

$$\hat{\mathcal{H}} = \beta_e [g_{\parallel} B_Z \hat{S}_Z + g_{\perp} (B_X \hat{S}_X + B_Y \hat{S}_Y)] + D [\hat{S}_Z^2 - S(S+1)/3], \quad (4.3)$$

with  $S = 1$ . The best fit parameters are given in Table 4.2. The curves in Figure 4.4 are calculated using these parameters for 6 K and are in a very good agreement with the experimental data. Some of the lines disappear for a few orientations, because the transition probability is dependent on the direction of the applied magnetic field  $\mathbf{B}$ . Avoiding saturation effects the linewidth  $\Delta B_{pp}$  of the various AB5 transitions is found to be strongly dependent on the magnetic field orientation. At room temperature linewidths in the range from 2.0 to 11 mT were observed.

The variations of the AB5 EPR resonances measured at room temperature have the same pattern as those obtained at 6 K, see Figure 4.5. However, by fitting this angular dependence with the spin Hamiltonian (4.3) we detect a small decrease of the zero-field splitting  $D$  as compared to the value measured at 6 K. The order of magnitude of this shift is within the

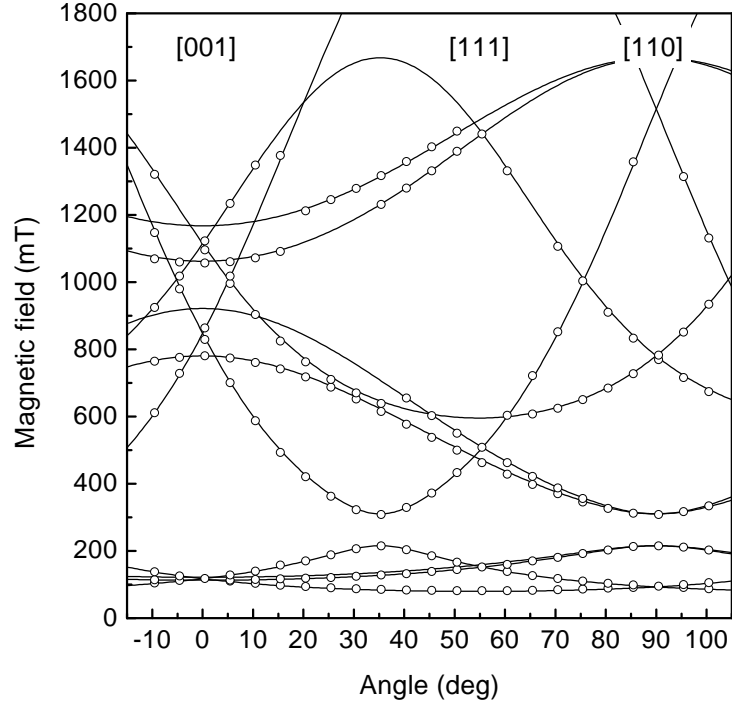


**Figure 4.4:** Angular dependence of the AB5 EPR lines measured in the  $Q$ -band at 6 K ( $\nu = 33.95$  GHz). Unlike the AB1 and AB3 centers, the AB5 lines were also detectable at room temperature. The magnetic field was rotated in a plane close to  $\{110\}$ . The open points represent the experimental data and the solid lines are angular dependencies calculated using the spin Hamiltonian (4.3) and the parameters given in Table 4.2 for 6 K. We detected a small misorientation of the rotation plane of  $\mathbf{B}$  relative to the  $(1\bar{1}0)$  plane, as it was observed in the angular variations of the AB1 and AB3 lines.

values which are expected to result from the thermal expansion of the diamond lattice.

Due to the large zero-field splitting, the EPR spectrum pattern has a very wide angular dependence and the EPR lines exhibit strong deviations for small differences in the orientation of the magnetic field  $\mathbf{B}$ . Moreover, as  $9.5 \text{ GHz} < D < 34 \text{ GHz}$ , the line positions and line intensities exhibit strong differences in the angular dependencies observed in the  $X$ - and  $Q$ -band, which hinders the detection of the AB5 center. Figure 4.6 shows the angular dependence of the EPR resonances related with the AB5 center measured in the  $X$ -band. Nevertheless, our EPR studies on the set of HPHT synthetic diamonds grown using pure

**Table 4.2:** Spin Hamiltonian parameters for the AB5 defect in diamond. The given values of the parameter  $D$  were determined from the angular dependence of the AB5 EPR lines observed at 6 K and at room temperature. The sign of the zero-field splitting  $D$  was determined from the relative intensity of the AB5 lines measured in the  $X$ -band (see Subsection 4.3.2).

Center	Symmetry	Spin	$g$ -values	Zero-field splitting (GHz)	$\Delta B_{pp}$ (mT)
AB5	Trigonal	1	$g_{\parallel} = 2.037(3)$	$D = -31.68(3)$ at 6 K	–
			$g_{\perp} = 2.022(3)$	$D = -28.77(3)$ at 300 K	2.0 – 11.0

nickel or nickel-alloys reveal that this center, along with W8 and P1, is always detectable in as-grown crystals synthesized without nitrogen getters (see Table 3.3). On the other hand, the corresponding EPR spectrum is absent in samples with low nitrogen content. As shown in Table 3.2, the former type of diamond shows a stronger incorporation of both nitrogen and nickel in comparison with samples synthesized using nitrogen getters. This suggests that, along with nickel, nitrogen is a probable constituent of the AB5 defects.

#### 4.3.2 THE SIGN OF $D$

The sign of the zero-field parameter  $D$  has generally no influence on the line positions of an EPR spectrum. Therefore, its sign must be determined from a different type of experiment. Normally, this can be obtained from the analysis of the relative intensity of specially selected EPR transitions.

The spin Hamiltonian (4.3) yields for  $S = 1$  the following matrix using the eigenfunctions  $|M_S\rangle = |+1\rangle, |0\rangle$  and  $|-1\rangle$  of  $\hat{S}_Z$  as a basis set:

$$\begin{bmatrix} \beta_e g_{\parallel} B_Z + \frac{1}{3} D & \frac{1}{\sqrt{2}} \beta_e g_{\perp} (B_X - iB_Y) & 0 \\ \frac{1}{\sqrt{2}} \beta_e g_{\perp} (B_X + iB_Y) & -\frac{2}{3} D & \frac{1}{\sqrt{2}} \beta_e g_{\perp} (B_X - iB_Y) \\ 0 & \frac{1}{\sqrt{2}} \beta_e g_{\perp} (B_X + iB_Y) & -\beta_e g_{\parallel} B_Z + \frac{1}{3} D \end{bmatrix}, \quad (4.4)$$

with the quantization axis  $Z$  being parallel to the axis of  $g_{\parallel}$  and  $D$ . In the special case of  $\mathbf{B}$  being parallel to the principal axis  $\mathbf{Z}$  of the trigonal center, its secular determinant leads to

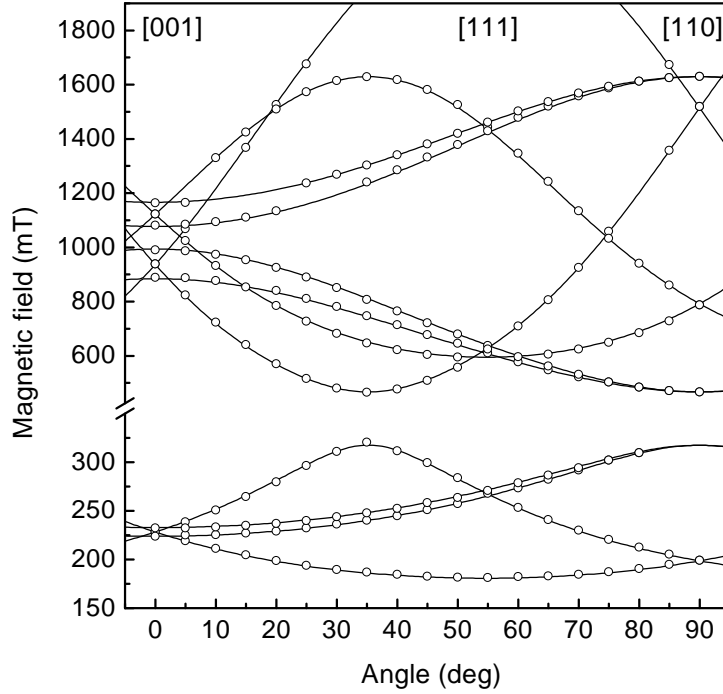


**Figure 4.5:** Angular dependence of the AB5 EPR lines upon rotation of the magnetic field in the  $(\bar{1}10)$  plane from  $[001]$  to  $[110]$  ( $\nu = 33.92$  GHz). The measurements were performed at room temperature in the  $Q$ -band. The open points represent the experimental data and solid lines are the angular dependencies calculated from the spin Hamiltonian (4.3) using the parameters given in Table 4.2 for room temperature.

the following eigenvalues:

$$U_{\pm 1} = \frac{1}{3} D \pm \beta_e g_{\parallel} B_Z \quad (4.5)$$

$$U_0 = -\frac{2}{3} D \quad (4.6)$$

and corresponding wavefunctions

$$T_{\pm 1} = |\pm 1\rangle \quad (4.7)$$

$$T_0 = |0\rangle. \quad (4.8)$$

The resulting energy-level diagram for  $\mathbf{B} \parallel [111]$  assuming  $D < 0$  is shown in Figure 4.7. This splitting pattern holds just for the particular equivalent orientation of the defect with

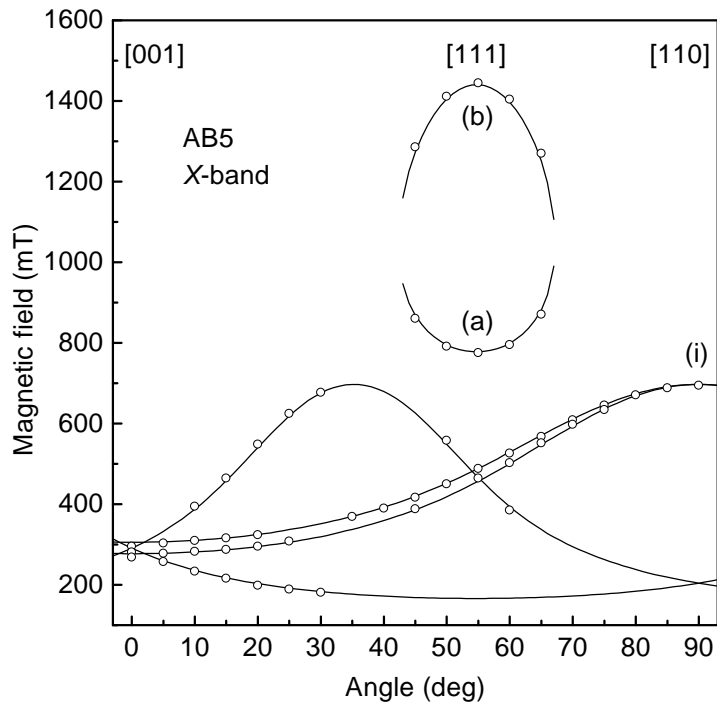


**Figure 4.6:** Anisotropy of the AB5 spectrum by rotation of the magnetic field in a plane close to  $\{110\}$  measured in the X-band at 50 K ( $\nu = 9.48$  GHz). The open points represent the experimental data and solid lines are the angular dependencies calculated from the spin Hamiltonian (4.3) using the  $g$ -values given in Table 4.2 and a parameter  $|D| = 31.6$  GHz. The lines are labeled according to the EPR transitions: (a) and (b) =  $|+1\rangle \leftrightarrow |0\rangle$ , (i) =  $|+1\rangle \leftrightarrow |-1\rangle$ .

the main direction  $\mathbf{Z}$  parallel to  $\mathbf{B}$ . In the X-band, three different transitions between the spin states are possible, namely, two  $\Delta M_S = \pm 1$  transitions, labeled (a) and (b) in Figure 4.7, and one  $\Delta M_S = \pm 2$  transition, labeled (c). For  $\mathbf{B}_1 \perp \mathbf{B}$  the transitions (a) and (b) are allowed transitions, whereas transition (c) is a so-called "forbidden" transition. The transitions (a) and (b) occur between the same states, but differ in their magnetic field position and EPR intensity  $I_{\text{EPR}}$ . The position of transitions (a) and (b) is highlighted in the angular dependence of the AB5 lines shown in Figure 4.6. In cases where the eigenfunctions are dependent on the magnitude of the magnetic field  $B$ , the transition probability and therefore also the EPR intensity is affected by the magnetic field position of the transition.

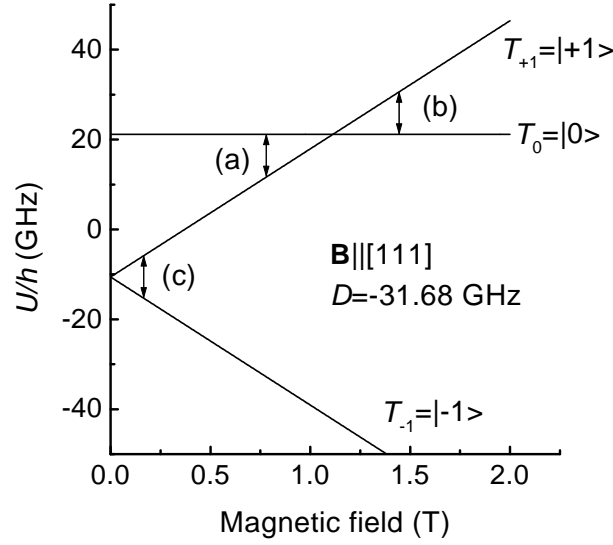


**Figure 4.7:** Energy-level diagram for the AB5 center with  $S = 1$  as a function of an applied magnetic field  $\mathbf{B}$  along  $[111]$  assuming  $D = -31.68$  GHz. The three possible transitions in the X-band are indicated by arrows (a), (b) and (c). If  $D > 0$  the ordering of the levels is inverted.

In the considered special case with  $\mathbf{B} \parallel \mathbf{Z}$  the eigenfunctions are, according to Equations (4.7) and (4.8), independent on  $B$ . Thus, the difference in the EPR intensities of the transitions (a) and (b) are determined only by their different values of the difference  $\Delta n$  between the populations of the states involved in these transitions. If  $D < 0$ , then  $\Delta n$  corresponds to the population difference between  $n_{+1}$  and  $n_0$ , which are the populations of the states  $T_{+1}$  and  $T_0$ , respectively. The difference between the  $\Delta n$  values of transitions (a) and (b) results from the different population of the spin states of the three level system and is dependent on the ordering of the spin states, which is determined by the sign of  $D$ . The values of  $\Delta n$  at the lower (a) and at the higher (b) resonance fields, assuming that the spin system is in the thermal equilibrium, are given by

$$\Delta n_{a,b} = n \frac{e^{\pm\beta h\nu} - 1}{1 + e^{\pm\beta h\nu} + e^{-\beta(2D \pm h\nu)}} \quad (4.9)$$

where the (+) and (-) signs hold for the (a) and (b) transitions, respectively, if  $D < 0$  and vice-versa for  $D > 0$ . Here,  $n$  is the number of AB5 centers and  $\beta$  equals  $(kT)^{-1}$ .  $T$  and  $k$  are the measurement temperature and the Boltzmann constant, respectively. Using

Equation (4.9) it is easily found that,

$$|\Delta n_a| - |\Delta n_b| > 0 \quad \text{for } D < 0 \quad (4.10)$$

$$|\Delta n_a| - |\Delta n_b| < 0 \quad \text{for } D > 0 \quad (4.11)$$

Thus, the sign of the difference between the intensity of the EPR lines (a) and (b) can be used for the determination of the  $D$  sign. However, only small differences in the intensity of the (a) and (b) lines were observed. These lines are presented in Figure 4.8 for an  $X$ -band measurement at 60 K with  $\mathbf{B}$  parallel to  $\mathbf{Z}$ . Therefore, the measurements were performed at

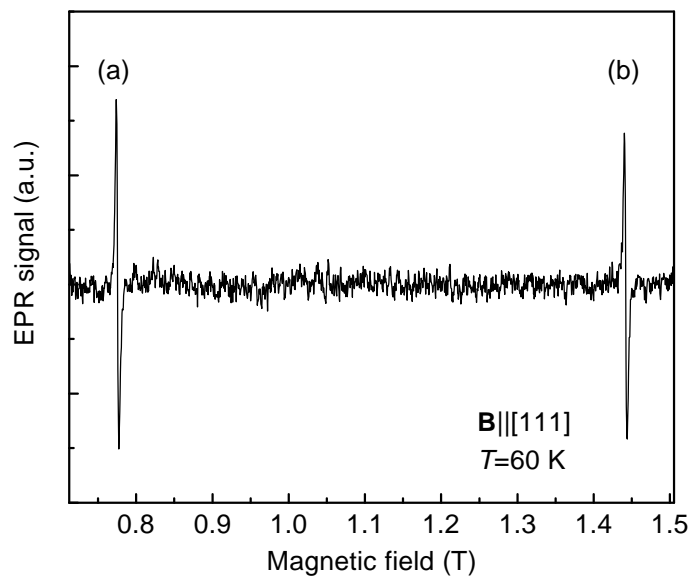


**Figure 4.8:** Part of the  $X$ -band EPR spectrum of the AB5 center measured at  $T = 60$  K showing the lines related to the transitions (a) and (b).

different temperatures in the range 60 – 130 K to determine the sign of  $D$ . Saturation effects which can affect the intensity differences between line (a) and (b) were avoided by choosing a suitable low microwave power. The intensities  $I_{\text{EPR}}^a$  and  $I_{\text{EPR}}^b$  of the EPR lines (a) and (b) were estimated through fitting the experimental lines with first-derivative Lorentzian functions. The temperature dependence of the obtained values ( $I_{\text{EPR}}^a - I_{\text{EPR}}^b$ ) is represented in Figure 4.9, together with the theoretical predictions for both a negative (solid line) and a positive (dashed line) parameter  $D$ . Despite of the scattering of the experimental values of ( $I_{\text{EPR}}^a - I_{\text{EPR}}^b$ ), a fit with the theoretical dependence is only possible assuming a negative

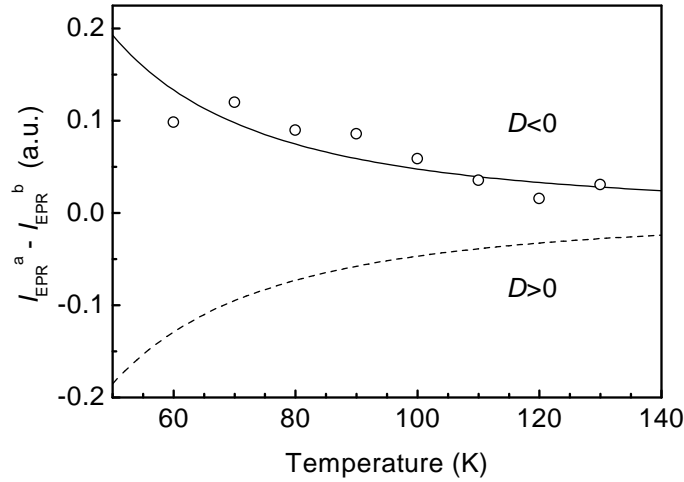


**Figure 4.9:** Temperature dependence of the intensities of the transition (a) and (b). The solid and dashed lines are calculated using Equation (4.9) for  $D < 0$  and  $D > 0$ , respectively.

sign for the zero-field splitting constant  $D$ .

### 4.3.3 MODEL OF THE AB5 CENTER

Nickel has been identified as an impurity forming localized electronic states in diamond. These defects have been described qualitatively on the basis of the simple Ludwig-Woodbury model, developed by Ludwig and Woodbury (1960) to describe transition metal impurities in semiconductors (see Section 2.3). This model was successfully applied to explain the negatively charged nickel in substitutional site  $\text{Ni}_s^-$  (Isoya *et al.*, 1990a). Furthermore, this theory was also used to justify the model proposed for the NIRIM1 paramagnetic defect of interstitial nickel in the positive charge state  $\text{Ni}_i^+$  (Isoya *et al.*, 1990b). More recently, Mason *et al.* (1999) used the Ludwig-Woodbury model to explain the MCDA and Zeeman-MCDA data obtained on the 1.40 eV optical absorption band. Based on a detailed analysis, the authors assigned the 1.40 eV system to  $\text{Ni}^+$  in a trigonally distorted tetrahedral interstitial site.

As in the case of the AB1 and AB3 centers, the measured  $g$ -values of the AB5 center deviate considerably from the free electron value  $g_e = 2.002319$ . As pointed out above, such deviation is symptomatic of a defect containing a transition metal ion in its structure. The observed

positive departures  $\Delta g$  of the  $g$ -values from the free spin value  $g_e$  indicate that the involved transition metal ion has a more than half-filled  $d$  shell, since these have negative spin-orbit coupling parameters  $\lambda$ . Among the possible transition metal elements, the most likely to be involved in the AB5 paramagnetic center is nickel. This statement is based on the fact that the studied samples were grown using nickel-containing solvent / catalysts and that the center is not detectable in the samples which evidence a considerably lower incorporation of nickel during growth (samples J to L).

A spin  $S = 1$  is consistent with a  $3d^8$  electronic configuration of a transition metal ion in cubic coordination. In the framework of the Ludwig-Woodbury model, a  $3d^8$  electronic configuration corresponds to a  $\text{Ni}^{2+}$  ion at an interstitial site or to a substitutional  $\text{Ni}^{2-}$  ion. The filling of the  $3d$  states in both cases is shown in Figure 4.10. Taking into account

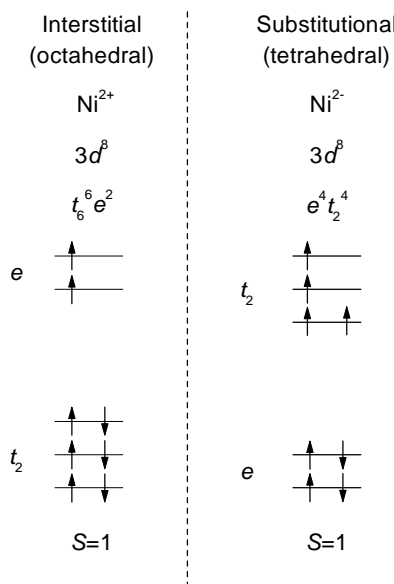


**Figure 4.10:** Valence states filling scheme of a transition metal with  $3d^8$  configuration in octahedral and tetrahedral crystal field. In the framework of the Ludwig-Woodbury model these may correspond to interstitial  $\text{Ni}^{2+}$  and substitutional  $\text{Ni}^{2-}$ , respectively.

the high concentration of the nitrogen donors  $\text{N}_s^0$  in the samples which exhibit the presence of AB5 centers, we believe that the latter configuration is the most probable one. The estimated concentration of  $\text{N}^+$  defects in the same samples is sufficiently high to provide charge compensation to nickel defects in the negative charge state. However, in such a case

the position of the Fermi level in comparison to the level of the AB5 center is decisive. Substitutional nitrogen is generally assumed to be the defect which determines the Fermi energy in diamond, since it is the dominant defect. Thus, the defect energy level of the AB5 center should be located below the thermodynamic filling level of the substitutional  $N^0$  center in order to have a negative charge state. In Chapter 6 the gap states induced by the AB5 defect and some other nickel-related centers will be investigated.

The parameter  $D$  measured for the AB5 center arises from different mechanisms. In Subsection 2.1.2, two of these mechanisms are mentioned: (i) the interaction with the local environment through the spin-orbit coupling that is given by Equation (2.19), and (ii) the spin-spin magnetic interaction. From Equations (2.17) and (2.19) is easily shown that,

$$D_{\text{so}} = \frac{\lambda}{2} \left[ g_Z - \frac{1}{2}(g_X + g_Y) \right], \quad (4.12)$$

$$E_{\text{so}} = \frac{\lambda}{4} (g_X - g_Y), \quad (4.13)$$

where  $(X, Y, Z)$  denote for the principal directions of the system. It is important to note that the expressions (4.12) and (4.13) are deduced only for unpaired electrons in orbitals centered on the same nucleus. This would be the case of electrons in the  $3d$  states of a transition metal ion. Using Equation (4.12), the contribution of the spin-orbit coupling to the parameter  $D$  can be estimated for orbital singlet states, if the spin-orbit parameter  $\lambda$  is known. Abragam and Bleaney (1970) give values of  $\lambda$  for several free  $3d$  ions. The value of  $\lambda$  determined experimentally for a free nickel ion with electronic configuration  $3d^8$  is found to be  $-9713$  GHz ( $-324$   $\text{cm}^{-1}$ ). With this uncorrected  $\lambda$  value we obtain with the  $g$ -values for the AB5 center,

$$g_Z = g_{\parallel} = 2.037; \quad (4.14)$$

$$g_X = g_Y = g_{\perp} = 2.022, \quad (4.15)$$

the following values for the contribution of the spin-orbit coupling to the zero-field splitting constants:

$$D_{\text{so}} = -73 \pm 11 \text{ GHz}, \quad (4.16)$$

$$E_{\text{so}} = 0 \text{ GHz}. \quad (4.17)$$

The calculated value of  $D_{\text{so}}$  is noticeably larger than the values of  $D$  given in Table 4.2, which were determined experimentally for the AB5 center. This observation suggests that

the zero-field splitting parameter  $D$  is mainly due to the interaction between the ground state and excited states via the spin-orbit coupling. The discrepancy between  $D_{so}$  and  $D$  can be attributed to bonding effects that produce a reduction of the effective value of the spin-orbit coupling parameter in the complex  $\lambda'$  as compared to the value  $\lambda$  of the free ion. This smaller value of the apparent spin-orbit parameter is generally observed in transition metal ions in solids (Abragam and Bleaney, 1970). Here, the difference between the measured parameter  $D$  and the value calculated using Equation (4.12) suggests a ratio  $\lambda'/\lambda$  of about 0.43.

As was pointed out above, the linewidth of the AB5 lines is relatively large and angular dependent. This may result from random strains in the sample which cause a small variation of the zero-field splitting and/or form an unresolved hyperfine interaction with a neighboring impurity with non-zero nuclear spin, like nitrogen. Thus, a simple model for the AB5 defect is a substitutional  $\text{Ni}^{2-}$  associated with a nearest-neighbor  $\text{N}^0$  atom. This results in a defect with  $C_{3v}$  symmetry. A scheme of such model for the AB5 paramagnetic center is shown in Figure 4.11. Alternatively, it can be a simple substitutional  $\text{Ni}^{2-}$  ion which undergoes a Jahn-Teller distortion to trigonal symmetry.

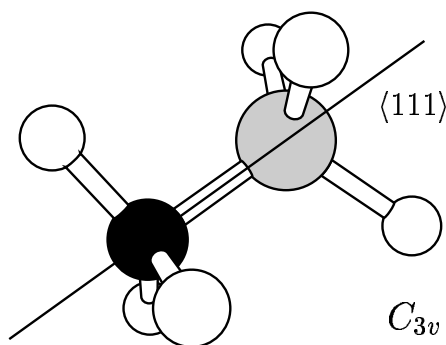


**Figure 4.11:** Atomic model considered for the AB5 center. The nickel and nitrogen atoms substitute two nearest-neighbor carbon atoms to form a negatively charged nickel-nitrogen complex with  $C_{3v}$  symmetry. The line represents the  $C_3$  trigonal axis  $\langle 111 \rangle$ .

## 4.4 THE AB2, AB4, AND AB6 CENTERS

### 4.4.1 EPR SPECTRA OF THE AB2, AB4, AND AB6

In the EPR spectra of the annealed samples, another set of previously unreported lines, was observed. The dependence of the intensity of these EPR lines on the applied microwave power reveal that these lines correspond to three different paramagnetic systems. The spectrum of the annealed crystal F is shown in Figure 4.12. This spectrum was recorded at 70 K using

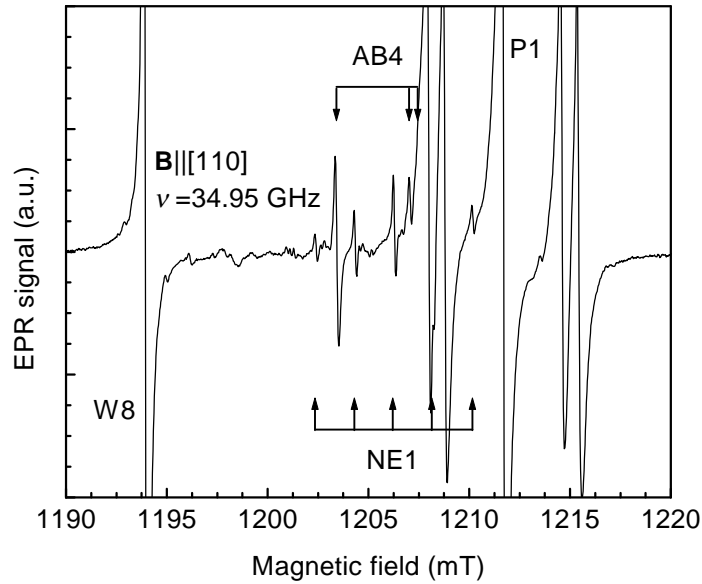


**Figure 4.12:** *Q*-band EPR spectrum of the annealed sample F showing the AB4 defect lines. The spectrum was measured at 70 K with the magnetic field  $\mathbf{B}$  parallel to [110] (100 kHz modulation frequency, 0.1 mT modulation amplitude and 0.2  $\mu\text{W}$  microwave power).

a low microwave power (0.2  $\mu\text{W}$ ) and the magnetic field applied in a direction parallel to  $\langle 110 \rangle$ . In this spectrum, we also observe as usual a trace of the P1 center and an isotropic line induced by the  $\text{Ni}_s^-$  defect. By a simulation of the EPR line positions with the spin Hamiltonian parameters given in the literature, another spectrum with a five-line hyperfine structure was identified as being the NE1 defect (Nadolinny *et al.*, 1999). EPR studies at room temperature and in a lower magnetic field range permitted also the detection of the NE2 paramagnetic center in the annealed samples F and G (see Figure 3.3). Besides,

lines corresponding to a new center named AB4 were detected. The variation of the  $g$ -values calculated from the dependence of the AB4 line positions with the direction of the applied magnetic field is shown in Figure 4.13. These correspond to a rotation of the external

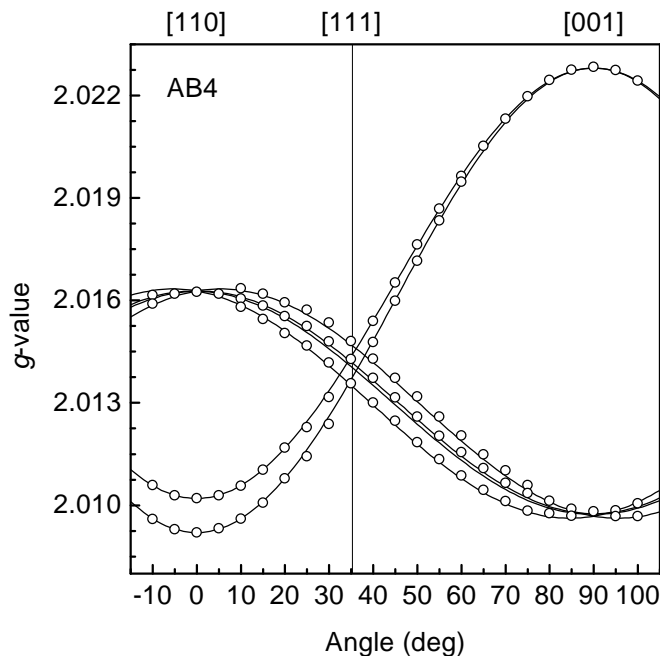


**Figure 4.13:**  $g$ -value variations of the AB4 EPR spectrum produced by rotation of the magnetic field in a plane very close to  $\{110\}$ . The zero angle correspond to the direction  $[110]$ . The open points represent the experimental data obtained in the  $Q$ -band and solid lines are the angular variations calculated from the spin Hamiltonian (4.1) using the parameters given in Table 4.1.

magnetic field in a  $\{110\}$  crystallographic plane. According to the experimental data plotted in Figure 4.13, the AB4 lines are produced by a  $S = \frac{1}{2}$  center with orthorhombic-I symmetry, exhibiting only a weak distortion from tetragonal symmetry. The positions of the EPR lines can be well described with the spin Hamiltonian (4.1), which contains only the anisotropic Zeeman term, and the  $g$ -values given in Table 4.3.

In addition to the AB4 lines, several unidentified lines with low intensity were observed in the spectrum of Figure 4.12. At an higher microwave power (0.8 mW) the lines related to the P1, NE1, NE2, and AB4 almost vanish in the EPR spectrum of sample F due to microwave

**Table 4.3:** Measured  $g$ -values and determined symmetries of the new  $S = \frac{1}{2}$  centers named AB2, AB4, and AB6.

Center	Symmetry	Spin	$g$ -values	$\Delta B_{pp}$ (mT)
AB2	Trigonal	$\frac{1}{2}$	$g_{\parallel} = 2.0080(3) \parallel [111]$ $g_{\perp} = 2.0680(3) \perp [111]$	$0.15 \pm 0.05$
AB4	Rhombic-I	$\frac{1}{2}$	$g_1 = 2.0228(3) \parallel [001]$ $g_2 = 2.0102(3) \parallel [110]$ $g_3 = 2.0092(3) \parallel [1\bar{1}0]$	$0.12 \pm 0.05$
AB6	Triclinic	$\frac{1}{2}$	$g_1 = 2.0750(3) \parallel [0.60316, 0.56822, 0.55975]$ $g_2 = 2.0252(3) \parallel [-0.00987, 0.70704, -0.70711]$ $g_3 = 2.0193(3) \parallel [-0.79756, 0.42097, 0.43207]$	$0.30 \pm 0.05$

power saturation and the spectrum becomes dominated by the group of lines shown in Figure 4.14. The spectrum of Figure 4.14 was recorded in the  $Q$ -band with the external magnetic field aligned parallel to a  $\langle 110 \rangle$  direction. In this spectrum we detect the AB1 and AB3 peaks, which were identified by their characteristic angular dependencies described in Section 4.2, and the presence of NE3 defects, with its complicated spectrum resulting from a complex of one nickel and three nitrogen atoms (Nadolinny *et al.*, 1999). The behavior of the intensity of other lines, named AB2 and AB6, with the applied microwave power indicate that they are induced by two distinct paramagnetic systems. The angular variation of the AB2 resonances was studied with  $\mathbf{B}$  rotating in a  $\{110\}$  plane. As our EPR spectra usually exhibit a great number of closely spaced lines, they strongly overlap for arbitrary directions of  $\mathbf{B}$ . Thus, to separate well the AB2 spectrum, the acquisition parameters were carefully chosen to maximize the intensity of the AB2 lines relatively to the other peaks. However, due to the complexity of the spectra, it was not possible to monitor exclusively the lines produced by the AB2 defects. Thus, the angular behavior of the AB2 lines was obtained from the full analysis of the spectra and by carefully excluding the lines which belong to other paramagnetic defects. The  $g$ -values resulting from such an analysis of the experimental data are plotted in Figure 4.15. These show the typical angular dependence of a center with trigonal symmetry. Fitting the experimental data with the spin Hamiltonian (4.1) gives the

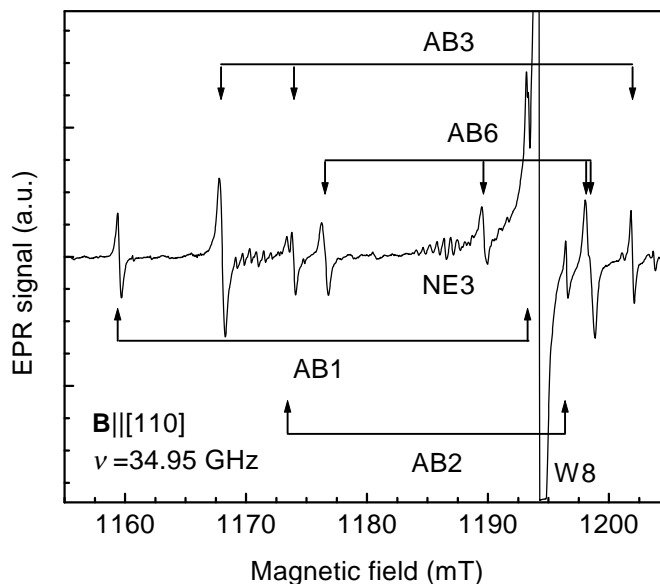


**Figure 4.14:** *Q*-band EPR spectrum of the annealed sample F showing the AB2 and AB6 peaks, together with the AB1, AB3, W8 and NE3 centers lines. The spectrum was measured at 70 K with the magnetic field  $\mathbf{B}$  parallel to  $\langle 110 \rangle$  (100 kHz modulation frequency, 0.1 mT modulation amplitude and 0.8 mW microwave power).

$g$ -values listed in Table 4.3.

The angular dependence of the AB6 line positions was determined in a similar way as that used in the case of AB2 lines. Figure 4.16 gives a plot of the variation of the AB6 spectrum versus the angle between the direction  $[110]$  and  $\mathbf{B}$  in a plane close to the  $(1\bar{1}0)$  plane. The peak-to-peak linewidth of the AB6 EPR lines observed in the spectra recorded at 70 K was approximately 0.30 mT. Moreover, it was detected a small misorientation of the rotation plane relative to the  $(1\bar{1}0)$  plane. The correct rotation plane was determined by the simultaneous analysis of the angular dependence of the well known P1 spectrum. The solid lines in the Figure 4.16 were calculated using the spin Hamiltonian (4.1) with  $S = \frac{1}{2}$  and the  $g$ -values given in Table 4.3, and also taking into account the misorientation of the rotation plane. The simulated angular variations are in very good agreement with the experimental data, in spite of the resolution given by the linewidth of the AB6 lines. The main axes system of the  $g$ -values used to calculate the variations of the solid lines in the Figure 4.16 do

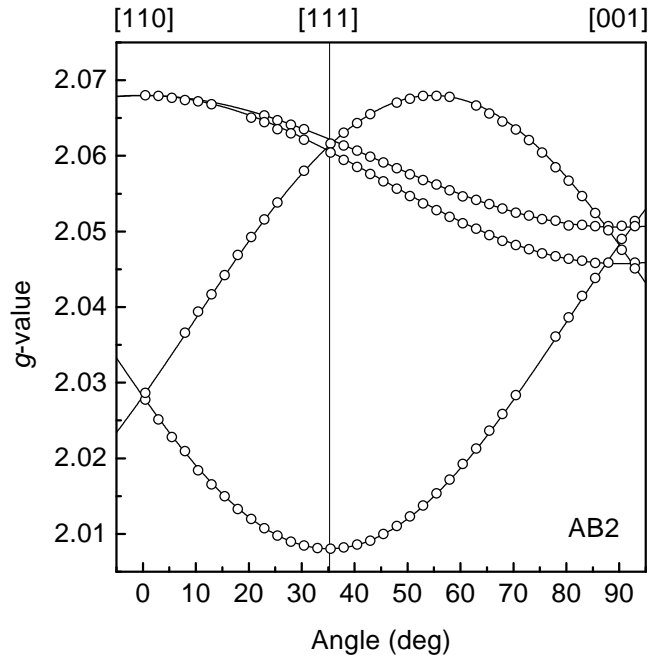


**Figure 4.15:** Angular dependence of the AB2 EPR spectrum by rotation of the magnetic field in a plane very close to  $\{110\}$ . The open points represent the experimental data and solid lines are the angular dependencies calculated from the spin Hamiltonian (4.1) using the parameters given in Table 4.3.

not fit any main crystallographic direction of the diamond structure. This means that, they correspond to a paramagnetic system which transforms according to the point symmetry groups  $C_1$  or  $C_i$  of the triclinic symmetry system. Moreover, since the principal direction of  $g_2$  is very close to  $[01\bar{1}]$ , the principal directions of the  $g$ -tensor correspond to a monoclinic-I system which experienced a very small distortion to triclinic symmetry. In the case of a triclinic defect, if the rotation of the magnetic field is performed in an arbitrary plane, each one of the 24 possible orientations of the defect have different EPR angular dependencies, whereas upon rotation within a perfect  $\{110\}$  plane only 12 angular dependencies could be distinguished. Since the rotation of the magnetic field was not performed in a perfect  $\{110\}$  plane, we must in principle observe more than 12 (maximum 24) different angular dependencies of the AB6 EPR lines, in order to distinguish between the monoclinic and triclinic symmetries. Owing to the limitations of the resolution of the spectral lines, we could not

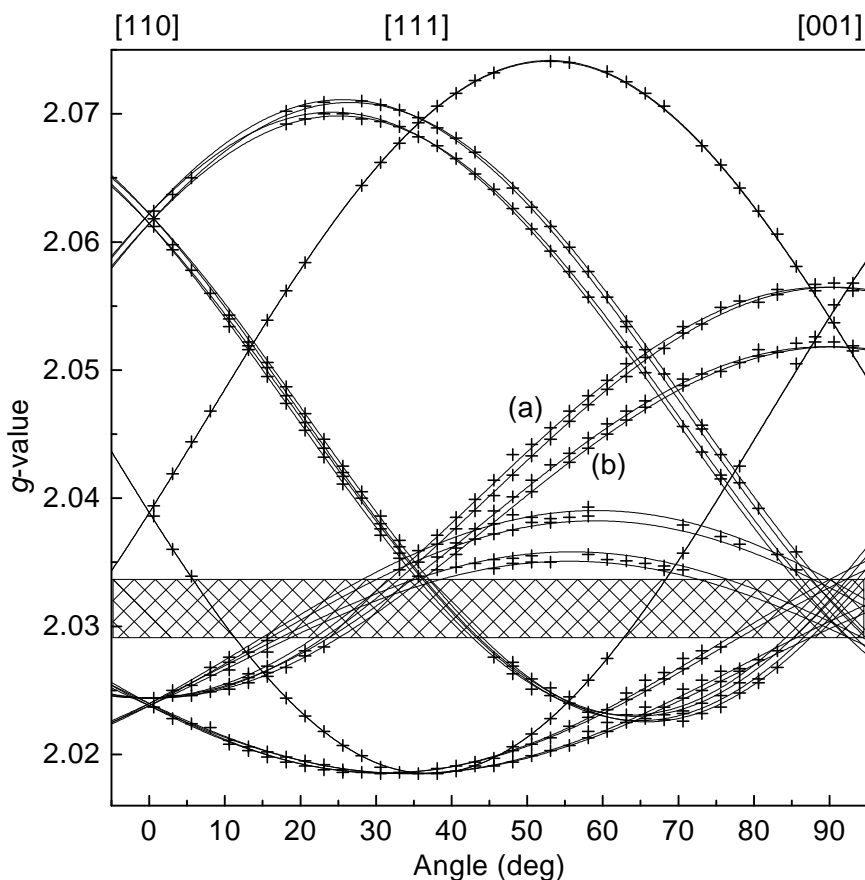


**Figure 4.16:** Angular dependence of the AB6 EPR spectrum upon rotation of the magnetic field in a plane deviated by  $2.5^\circ$  from the  $(1\bar{1}0)$  plane. The misorientation of the rotation plane was determined by simultaneously recording the anisotropic hyperfine structure of the P1 center lines. The crosses represent the experimental data and the solid lines are the angular dependencies calculated from the spin Hamiltonian (4.1) using the parameters given in Table 4.3.

observe all the 24 angular variations. However, it is clearly verified that the two pairs of peaks labeled (a) and (b) in Figure 4.16 would have the same angular dependence if we consider that the defect has monoclinic-I. The observed splitting in sets of lines (a) and (b) is only justified by assuming that the AB6 defect has a triclinic symmetry. In the shaded area of Figure 4.16 the detection of the AB6 lines was not possible due to overlapping with the strong W8 isotropic line at  $g = 2.0319$ .

The peak-to-peak linewidths of the AB4, AB2, and AB6 EPR lines observed in the spectra recorded at 70 K are approximately 0.15, 0.12 and 0.30 mT, respectively. Other paramagnetic centers, like the P1, W8, and NE1 exhibit in the same samples linewidths of 0.2, 0.15, and 0.14 mT, respectively. The strong overlapping of the EPR lines at magnetic fields corresponding to  $g \approx g_e$  hindered the observation of any significant variation of  $\Delta B_{pp}$  with the direction of the applied magnetic field.

#### 4.4.2 NATURE OF THE AB2, AB4, AND AB6 DEFECTS

The nature of the AB2, AB4, and AB6 defects is unknown up to now, because there are no indications of hyperfine interactions related with the EPR spectra of these centers. An hyperfine structure would give a fingerprint of a particular impurity. Thus, in our case a direct chemical identification by such structure was not possible. However, there are some strong hints concerning the nature of these centers.

The samples which contain the AB2, AB4, and AB6 defects were subjected to an heat treatment at 1600°C. It is established that at such temperatures the vacancy and carbon interstitial defects are highly mobile in diamond. During annealing at temperatures higher than 550°C the vacancy becomes mobile and is easily trapped by nitrogen pair centers (*A* aggregates) (Davies, 2001). Defects related with carbon interstitials are found to anneal out at temperatures of about 500°C (Twitchen *et al.*, 2001). Thus, it is expected that any defect composed only by combinations of intrinsic defects would be completely annealed out at the same temperatures as those at which the samples F and G were heat treated. Moreover, this type of defects exhibit *g*-values which are typically extremely close to  $g_e$  (Ammerlaan, 1990), in disagreement with the observed for the AB2, AB4, and AB6 centers. A common feature of the *g*-values of the AB2, AB4, and AB6 centers is that they are significantly greater than  $g_e$ . Thus, these defects should be impurity-related.

As discussed above for the AB1 and AB3 defects, the *g*-values which are measured for the AB2, AB4, and AB6 defects are quite uncommon for the defects in diamond. Since usually *g*-values very close to the free electron value  $g_e$  are measured (Ammerlaan, 1990; Baker and Newton, 1994). This indicates that it is very likely that the AB2, AB4, and AB6 defects are related with a transition metal. Since the AB2, AB3, and AB4 defects are only detected in diamonds grown with nickel as a solvent catalyst, it is reasonable to assume that they are nickel-related. Besides, the measured *g*-values, which are greater than  $g_e$ , are consistent

with a  $d^n$  electronic configuration with a more than half-filled  $d$ -shell, as would be the case of nickel.

Because no hyperfine structure could be observed, nitrogen seems not to be directly involved in these centers. At least for the AB2 and AB4 centers, the observation of relatively sharp lines (linewidths of 0.12 and 0.15 mT, respectively), indicates that it is quite unlikely that nitrogen participates in the defects within the close vicinity of the nickel ion. However, the possibility that nitrogen is present in one of the distant neighboring sites should not be ruled out. Alternatively, the observed different magnitudes and symmetries of the AB2, AB4, and AB6 lines suggest associations with other impurities with low abundance of isotopes with non-zero nuclear spin, like oxygen, or intrinsic defects. Moreover, the fact that these paramagnetic centers are only detected in annealed samples indicate that these defects are produced during the heat treatment of HPHT diamond.

From the studies of kinetics of the nitrogen aggregation it is known that the rate of aggregation is increased by the nickel concentration (see Section 1.7). This dependence was explained by the release of vacancies, which in turn assist in the migration of nitrogen, or through the release of carbon interstitials that in turn release high mobile interstitials (Fisher and Lawson, 1998; Kiflawi *et al.*, 1998). Another source of mobile defect components are defect complexes, which dissociate at certain annealing temperatures. Since these processes must occur in the vicinity of nickel, we could admit that the new centers result from substitutional nickel capturing a vacancy, or that the dissociation processes leave complexes of nickel that become paramagnetic.

## 4.5 SUMMARY

The careful analysis of the EPR spectra measured in HPHT diamonds grown with nickel-containing solvent / catalysts could distinguish for the first time a group of six paramagnetic defects, which are named here as AB1 to AB6 (AB centers). The new centers appear in the samples which exhibit an high concentration of nitrogen-related defects.

Through the analysis of the anisotropic characteristics of the EPR spectra of the AB centers their corresponding spins and symmetries were established. The spin Hamiltonian parameters were determined for all the observed defects (see Tables 4.1, 4.2, and 4.3). It is found

that all defects are spin-half systems, with the exception of the AB5 center which has spin  $S = 1$ . The AB1, AB2, and AB5 paramagnetic centers are proved to be trigonal and the AB3 and AB4 defects exhibit orthorhombic-I symmetry. It is shown that the triclinic symmetry of the AB6 center results from a small distortion of a center with monoclinic-I symmetry.

It is found that the as-grown HPHT samples where the AB1 and AB3 centers appear in detectable amounts also exhibit an higher concentration of W8 centers. The AB2, AB4, and AB6 paramagnetic centers are detected solely in diamonds which suffered post-growth heat treatments at high temperatures. EPR measurements performed with several samples, which were grown under different conditions, revealed that the AB5 center is always detectable in diamonds grown using nickel-containing solvent / catalysts without the addition of any nitrogen getter.

No hyperfine structure could be resolved in the EPR spectra of the AB1 to AB6 defects. The determined  $g$ -values strongly suggest that these centers involve a transition metal ion. The sign of the deviations  $\Delta g = g - g_e$  suggests a transition metal ion with a more than half-filled  $d$ -shell. Hence, the fact that the AB defects were detected in samples which were grown with nickel as solvent / catalysts indicate that the transition metal involved in the defects should be nickel. Nickel has only one isotope with a non-zero nuclear spin ( $I = 3/2$ ) with natural abundance of 1.13%, which would not produce a detectable hyperfine structure in the spectra.

The linewidths of the AB1-AB4, and AB6 spectral lines are small enough to exclude the presence of nitrogen in the close vicinity of these centers. It is likely that these centers are complexes of nickel and intrinsic defects that are formed during growth or upon high temperature anneal of the crystals.

In the framework of the Ludwig-Woodbury theory, a model based on substitutional nickel in the double negative charge state is proposed for the AB5 center. Here, the trigonal distortion of the tetrahedral substitutional site is assumed to be due to a neighboring nitrogen atom, which bonds to nickel to form a defect with  $C_{3v}$  symmetry. In this configuration the defect may be assumed as a nickel-nitrogen pair in the negative charge state  $(Ni_s-N_s)^-$ . The sign of the zero-field splitting  $D$  was determined through the comparison of the intensity the AB5 EPR lines. This study established that the parameter  $D$  has a negative sign.



# CHAPTER 5

## ANNEALING STUDY OF HPHT

### DIAMOND

#### 5.1 INTRODUCTION

The incorporation of transition metal ions in the diamond lattice during HPHT growth has attracted considerable attention in the last decade (see Section 1.6). It has also been found that some of the nickel-related defects are stable only in a limited range of annealing temperatures. The formation of several defects related to nickel and nitrogen during heat treatments of such HPHT diamonds has been studied. In Section 1.7, a summary of the main results found to date in the literature regarding the behavior of impurity-related defects upon high temperature heat treatments is given.

In Chapter 4 is shown that several previously unreported nickel-related paramagnetic defects are found in diamond samples growth at HPHT. The appearance and missing of such centers in the studied samples seems to indicate that some of the defects are produced upon annealing. Moreover, it is also observed that the occurrence of the new centers correlates with the amount of nickel that is incorporated in the crystals during growth.

In order to investigate the formation of the various centers and the relations between the AB1 to AB6 defects and the nickel-nitrogen complexes, detailed annealing experiments of HPHT crystals grown from nickel-containing solvent / catalysts were carried out (Pereira *et al.*, 2002c). In the present chapter, the quantitative results of these investigations are presented (Pereira *et al.*, 2002d). In particular, the formation and annealing behavior of nickel-related paramagnetic defects in nickel- and nitrogen-containing diamond subjected

to heat treatments at temperatures in excess of 1400°C is examined. The role of the AB defects in the aggregation kinetics of nitrogen during high temperature annealing and their relations with other nickel containing defects (NE centers) are discussed. In this chapter, a new paramagnetic defect (labeled AB7) detected after annealing HPHT diamond is also described (Pereira *et al.*, 2002b).

## 5.2 EXPERIMENTAL DETAILS

The crystals shown in Table 3.1, synthesized at the NIRIM (Japan) by the temperature gradient method using Ni-containing solvent / catalysts, were used in the studies presented in this chapter. In order to monitor the formation conditions of the nickel-related paramagnetic defects, we selected two crystals with different levels of nickel incorporation. This characteristic is quantified by the concentration of W8 centers measured by EPR (see Chapter 3). Moreover, the as-grown crystals to be used here should not evidence any sign of pre-annealing during growth, which can be detected through the observation of other nickel-related EPR lines than the W8 resonance. Among the available set of samples a logical choice are the samples H and J, which were grown using Ni-20 wt.% Fe and Ni-2 wt.% Ti alloys as solvent / catalysts, respectively. These diamonds were subjected to an isochronal annealing sequence in the temperature range between 1550 – 2000°C. Heat treatments were carried out using the same apparatus as for growing the crystals. EPR spectra were measured after each anneal step at suitable temperatures in the range from 4.2 to 100 K, depending on which paramagnetic center was detected.

EPR measurements were carried out on the Bruker ESP 300E spectrometer mentioned above. This equipment was mounted with *X*- and *Q*-band microwave bridges and corresponding cylindrical TE<sub>011</sub> microwave resonators. For measuring EPR at low temperatures we used an helium gas-flow cryostat for the *X*-band and an helium bath cryostat for the *Q*-band, respectively. Samples were oriented with respect to the external magnetic field **B** either by growth facets or by faces polished parallel to the main crystallographic planes.

Infrared absorption spectra were also measured in the as-grown samples and after each anneal so that the concentrations of the substitutional nitrogen defects N<sup>0</sup> could be determined throughout the annealing sequence.

## 5.3 RESULTS AND DISCUSSION

Nitrogen present in diamond induces absorption in the one-phonon region. The different forms of incorporated nitrogen give rise to characteristic spectra that can be used to estimate their respective concentrations. This was done by reconstructing the experimental IR absorption spectra as a mixture of the well known  $A$ ,  $B$ ,  $N^0$  and  $N^+$  components. Using the calibrations between the absorption coefficient  $\mu_x(y)$ , measured at the photon wave number  $x$  of the component  $y$  ( $y = N^0, N^+, A$  and  $B$ ), and the nitrogen concentration in the form  $y$  (see Table 1.2), the concentration of nitrogen in each form was estimated. The concentrations of substitutional  $N^0$  centers determined in this way were used as a calibration in the determination of the concentration of the other defects through the EPR spectra.

The various paramagnetic centers, which produce overlapping EPR lines in the  $X$ - and  $Q$ -band, were identified through their complete angular dependence upon rotation of the external magnetic field  $\mathbf{B}$  in an  $\{110\}$  crystallographic plane. These angular positions were calculated using the spin Hamiltonian,

$$\hat{\mathcal{H}} = \beta_e \mathbf{B} \cdot \mathbf{g} \cdot \hat{\mathbf{S}} + \hat{\mathbf{S}} \cdot \mathbf{D} \cdot \hat{\mathbf{S}} + \sum_i \hat{\mathbf{S}} \cdot \mathbf{A}_i \cdot \hat{\mathbf{I}}_i, \quad (5.1)$$

with parameters given in the corresponding references. The ratio between the concentration of these centers and that of the well known P1 center (substitutional  $N^0$ ) was determined by comparing their EPR spectrum intensity. In order to avoid any errors by saturation effects, the saturation behaviour of the transitions were studied by measuring the dependence of  $I_{\text{EPR}}$  on the applied microwave power  $P_0$ . For the concentrations determination the spectra were measured always upon non-saturated conditions, where  $I_{\text{EPR}} \propto (P_0)^{1/2}$ . Although the optimum experimental conditions for the detection of the P1 center are different from those of the other defects, we have carefully chosen the acquisition parameters (e.g., temperature, modulation amplitude, modulation frequency, magnetic field direction, etc.) which permitted the simultaneous observation of the lines of the P1 center and the lines of a defect with unknown concentration. In this manner, the intensity ratio of both signals is merely due to deviations in the population difference  $\Delta n$  of the states involved in the monitored transitions and the square of the matrix element of the amplitude of the excitation spin Hamiltonian  $\hat{\mathcal{H}}_1$  (see Subsection 2.1.8). In the cases where the detection of the two spectra at the same microwave power level  $P_0$  was not possible, their values of  $I_{\text{EPR}}$  were corrected according to the power dependence  $I_{\text{EPR}} \propto (P_0)^{1/2}$  for non-saturated lines. In Section 2.1.8, the principal

variables influencing the intensity of an EPR line are summarized.

A decisive quantity is the difference in the population of the levels  $\Delta n$ , which depends among other things on the concentration  $n$  of the given defect and on the energy level diagram of the considered spin manifold. For systems with  $S = \frac{1}{2}$ , like the P1 defect, the difference between the population  $n_{-1/2}$  of the lower  $M_S = -\frac{1}{2}$  level and the population  $n_{+1/2}$  of the upper  $M_S = +\frac{1}{2}$  level is given under resonance conditions by

$$\Delta n = n_{-1/2} - n_{+1/2} = n \frac{1 - e^{-\beta h\nu}}{1 + e^{-\beta h\nu}}, \quad (5.2)$$

assuming a Boltzmann population distribution. In this expression  $\beta$  and  $h\nu$  have the same meaning as in Equation (4.9). The concentration ratio between a defect having  $S = \frac{1}{2}$  and the P1 center in the same sample is equal to the ratio between the intensity of their EPR spectra, if the difference in the transition probabilities resulting from different  $g$ -values can be neglected (see Subsection 2.1.4). Such assumption is justified because the  $g$ -values of the centers under study are all close to 2. To determine the correct  $I_{\text{EPR}}$  of each spectrum their anisotropy and hyperfine structure must be taken into account. For example, in the case of a trigonal center with an EPR pattern similar to that shown in Figure 2.4, the anisotropic line  $d$  corresponds to only one of the four distinguishable center orientations. Thus, in order to compare the concentration of this center with that of another defect, we must multiply the intensity of the EPR line  $d$  by four to account for all possible orientations of the center in the lattice.

The relation between  $\Delta n$  and  $n$  of Equation (5.2) is only valid for  $S = \frac{1}{2}$  defects, thus, for systems with  $S > \frac{1}{2}$ , like AB5 center, we must consider another equation. In addition, the transitions monitored in the AB5 triplet system and in the  $S = \frac{1}{2}$  calibration defect (P1 center) have different natures. This is reflected in a difference in their transition probabilities.

The transition used to quantify the AB5 center concentration is shown in Figure 5.1. This transition is induced by applying the external magnetic field  $\mathbf{B}$  along [110] and produces the line at the EPR spectrum with magnetic field position labeled as (i) in Figure 4.6. Assuming the Boltzmann statistics, we obtain that for the used temperatures the ratio between  $\Delta n$  and  $n$  at the  $M_S = -\frac{1}{2} \leftrightarrow \frac{1}{2}$  transition of an  $S = \frac{1}{2}$  system (P1 center) is about 1.49 times the ratio obtained for the transition monitored at the AB5 center. Using the spin Hamiltonian (5.1) the wavefunctions  $T_l$  and  $T_u$  of the lower and upper states, respectively, were calculated for the resonance conditions. Taking the rotation plane of the samples as being the (1 $\bar{1}$ 0)

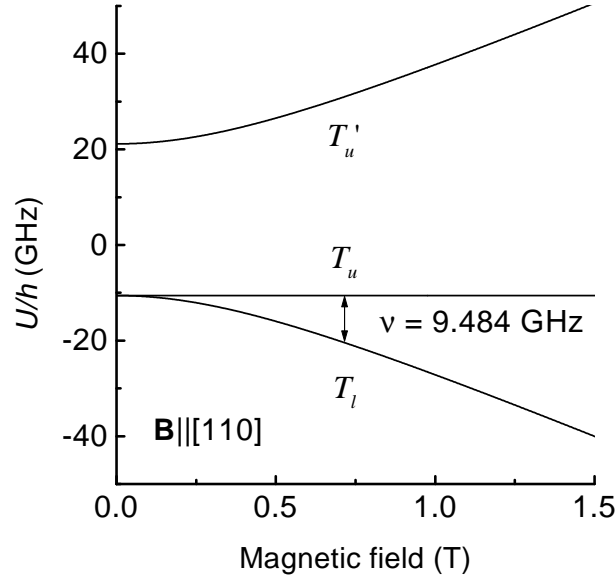


**Figure 5.1:** Energy levels for the AB5 center ( $S = 1$ ) as a function of the applied magnetic field  $\mathbf{B} \parallel [110]$  for the two equivalent orientations which have both  $g_{\parallel}$  and  $D$  along the crystallographic directions  $[\bar{1}11]$  and  $[1\bar{1}1]$ . The arrow represents the single EPR transition which is induced under such conditions in X-band measurements.

plane, the exciting magnetic field  $\mathbf{B}_1$  in the used cylindrical resonators is parallel to the direction  $[1\bar{1}0]$ . In this manner, the transition probability ratio between the transition monitored at the AB5 center and the  $M_S = -\frac{1}{2} \leftrightarrow \frac{1}{2}$  transition observed in the P1 defect is

$$\frac{|\langle T_l | \mathbf{B}_1 \cdot \mathbf{g}' \cdot \hat{\mathbf{S}} | T_u \rangle|^2}{|\langle -\frac{1}{2} | \mathbf{B}_1 \cdot \mathbf{g}'' \cdot \hat{\mathbf{S}} | +\frac{1}{2} \rangle|^2} \cong 2.498, \quad (5.3)$$

with  $\mathbf{g}'$  and  $\mathbf{g}''$  being the  $g$ -values of the AB5 and P1 defects, respectively. The measured ratio between the EPR spectra intensities of the AB5 and P1 centers was divided by the factor 2.498/1.49 for determining their relative concentrations.

### 5.3.1 ANNEALING SEQUENCE: SAMPLE J

Prior to annealing, sample J exhibited a green color that changed to brown after annealing at a temperature as high as 2000°C. It is believed that the formation of nickel-nitrogen centers during heat treatments is responsible for this color change. In Table 5.1, the concentrations of

the paramagnetic centers detected in sample J are listed throughout a sequence of isochronal heat treatments at temperatures in the range 1550–2000°C. At all annealing stages the EPR

**Table 5.1:** Concentrations of the paramagnetic centers throughout the isochronal annealing sequence. –, center was not detected; \*, center detected but EPR lines measured in fast-passage conditions, hindering the determination of its concentration.

Sample	Center (Reference)	Concentrations of centers (ppm) $\pm 20\%$				
		As-grown	Annealing (°C)			
			1550	1700	1900	2000
J	P1 (Smith <i>et al.</i> , 1959)	10	11	8	6	2.6
	W8 (Samoilovich <i>et al.</i> , 1971)	3.1	3.6	3.4	2.4	0.2
	NIRIM1 (Isoya <i>et al.</i> , 1990b)	0.21	0.18	0.27	0.10	0.05
	NIRIM2 (Isoya <i>et al.</i> , 1990b)	*	*	*	*	*
	AB7 (Table 5.2)	–	–	0.03	0.07	0.02
H	P1 (Smith <i>et al.</i> , 1959)	205	114	50	26	19
	W8 (Samoilovich <i>et al.</i> , 1971)	16	12	3.5	0.04	–
	AB5 (Table 4.2)	1.1	0.8	0.5	0.2	–
	AB1 (Table 4.1)	–	–	0.03	0.04	–
	AB3 (Table 4.1)	–	–	0.03	–	–
	AB6 (Table 4.3)	–	–	0.01	0.15	–
	NE1 (Nadolinny <i>et al.</i> , 1999)	–	–	0.6	0.22	0.15
	NE2 (Nadolinny <i>et al.</i> , 1999)	–	–	–	0.65	1.1
NE3 (Nadolinny <i>et al.</i> , 1999)	–	–	–	0.13	0.28	

measurements of sample J show the spectra of the P1, W8, NIRIM1, and NIRIM2 centers. The concentrations of the defects P1, W8, and NIRIM1 evidenced a significant decrease only after the heat treatment at 1900°C.

In accordance with the observations of Isoya *et al.* (1990b), we were not able to measure the NIRIM2 EPR lines in slow-passage conditions, which hindered the determination of its concentration. However, we could observe that the NIRIM2 defect persisted at the annealing temperature of 2000°C. Moreover, no remarkable changes were observed in the intensity of

the NIRIM2 spectrum after each anneal step, thus we may conclude that the NIRIM2 is a rather stable center. This result confirms that it is reasonable to assume that the NIRIM2 defect consists of a nickel atom associated with another defect, which would produce a very stable structure. For instance, it can be an interstitial  $\text{Ni}^+$  ion with a vacancy at a neighboring position, as it was proposed by Isoya *et al.* (1990b). It is believed that the 1.40 eV optical system is the optical analogue to the NIRIM2 EPR center (see Section 1.6.1). Photoluminescence studies of annealed diamonds growth at HPHT from nickel-containing systems also revealed that the 1.4 eV vibronic system is still present in the optical spectra of crystals that underwent heat treatments at temperatures as high as 2200°C and 2500°C (Kupriyanov *et al.*, 1999).

After annealing sample J at 1700°C, the lines related with another center labeled AB7 appeared in the EPR spectrum. The angular dependence of the AB7 EPR lines shows that this spectrum is produced by a paramagnetic defect with orthorhombic-I symmetry and spin  $S = \frac{1}{2}$  (see Section 5.3). The departures of the principal  $g$ -values from the free electron value  $g_e$  found for this center, indicate that the center probably contains a transition metal ion in its structure. The AB7 center exhibits a transitory behavior: its EPR intensity increases after anneal at 1900°C and a decrease is observed after the heat treatment at 2000°C. The AB7 center is formed at early annealing stages before nitrogen shows a significant aggregation. It might be produced through the capture of mobile vacancies and/or interstitials by a nickel-related defect.

### 5.3.2 ANNEALING SEQUENCE: SAMPLE H

The as-grown sample H exhibited the yellow color typical of nitrogen-rich diamond. Alike sample J, the color of sample H changed progressively to brown as it was sequentially annealed. In addition to the P1 center, the as-grown sample H showed the presence of W8 and AB5 defects. Heating this sample at 1550°C caused a decrease of the P1 signal, as opposed to sample J where a significant change in the P1 signal intensity was detected only after annealing at 1900°C. A similar behavior was observed for the W8 signal intensity. A decrease in the P1 concentration is accompanied by a decrease in the W8 signal intensity in both samples H and J, regardless of the differences in initial nitrogen concentration. This indicates that the main process of the nitrogen aggregation in such type of diamonds should also involve the W8 defect. This result supports the suggestion that the enhancement of nitrogen

aggregation in nickel containing diamonds is due to the generation of carbon interstitials by nickel defects which in turn produce highly mobile nitrogen interstitials (Kiflawi *et al.*, 1998; Fisher and Lawson, 1998). The process occurs when a substitutional Ni ion displaces a neighboring carbon atom, creating a nickel-vacancy defect. The released carbon interstitial can migrate to substitutional N atoms and exchange positions, creating an highly mobile N interstitial. These nitrogen atoms can then migrate to form *A* centers. Another proposed mechanism responsible for the increase of the formation rate of nitrogen pairs is based on the release of vacancies from a nickel-related complex. Nadolinny *et al.* (2000) argued that the NE4 nickel-vacancy related trigonal center is the one responsible for the release of vacancies in this process. These vacancies would be trapped by nitrogen and in this way would assist in the migration of nitrogen (Kiflawi *et al.*, 1998; Nadolinny *et al.*, 2000).

The EPR signal of the AB5 center in sample H decreases throughout the annealing sequence and disappears after an heat treatment at 2000°C. This center was detected in all as-grown samples synthesized without the addition of nitrogen getters to the nickel-containing solvent / catalyst. In Subsection 4.3.3 a model consisting of a nickel-nitrogen pair in the negative charge state was proposed for its structure. For such center structure we expect that during anneal the AB5 defects will behave in a similar way as that suggested by Nadolinny *et al.* (1999) for the single substitutional Ni<sup>-</sup> defect. Hence, nickel, being larger than carbon, would release one of its four nearest-neighbors, possibly the nitrogen atom, forming a defect with the same structure as the one suggested for the NE4 center, NiVC<sub>6</sub> (see Figure 5.2). This mechanism would obviously lead to the annealing out of the AB5 centers upon high temperature heat treatments.

After annealing sample H at 1700°C we detected the EPR spectra of the AB1, AB3, and AB6 centers described in Chapter 4, as well as the resonances of the NE1 defect. The EPR spectra of the AB1, AB3, and AB6 again disappear after the heat treatment at 1700°C. Although the AB1 and AB3 lines appeared in the EPR spectra of sample H only after annealing at 1700°C, they were also observed in some as-grown samples, as shown in Table 3.3. Our EPR measurements in the available set of samples reveal that there is a general trend to detect the AB1 and AB3 centers in as-grown samples which evidence an higher amount of nickel incorporation during growth. Representative examples of this observation are the samples A, B, and C, in contrast to samples H to L. In the former crystals the concentration of substitutional Ni<sup>-</sup> defects is significantly higher than in the latter ones, as it is shown in

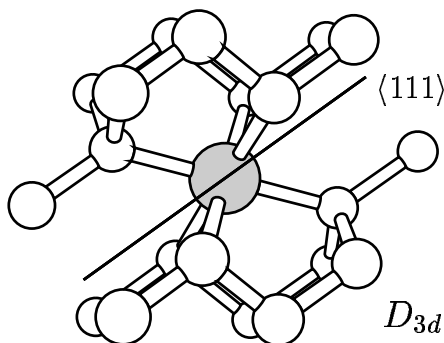


**Figure 5.2:** Model proposed for the NE4 paramagnetic center (Nadolinny *et al.*, 1999). It is suggested that the paramagnetic charge state of this structure should be responsible for the AB1 EPR spectrum.

Table 3.2. This difference is clearly due to the fact that a 100% Ni solvent / catalyst was used to grow samples A, B, and C, whereas in the synthesis of samples H to L, an Ni-Fe alloy (samples H and I) or a nickel catalyst with nitrogen getters added (samples J to K) was used. The utilization of nitrogen getters seems to lead to a lowering of the incorporation of both nitrogen- and nickel-related defects (Isoya *et al.*, 1990*b*), at least of those centers which are detected by infrared absorption and EPR spectroscopy. On the contrary to the AB1 and AB3 defects, the AB6 center has never been detected in as-grown diamond samples studied in this work. It is quite likely that the AB1, AB3, and AB6 centers are products of the nickel-related generation of carbon interstitials. As mentioned above, these carbon atoms are supposed to be responsible for the enhancement of the nitrogen aggregation observed in nickel-containing diamonds. The AB1, AB3, and AB6 centers are transient defects that anneal out at higher temperatures, being transformed into other more stable defects. These are possibly the NE1-NE3 and NE5 nickel-nitrogen complexes.

At annealing temperatures higher than 1700°C we observed the appearance of the NE2 and NE3 spectra, as well as a slight decrease in the concentration of NE1 centers. According to Nadolinny *et al.* (1999), these centers are produced by aggregation of mobile nitrogen atoms to a nickel impurity during the annealing of nickel-containing diamond (see Subsection 1.7.2). The detection of the NE1 center after anneal at 1700°C support this suggestion. Additionally, we observed that this signal decreases progressively as we anneal the sample

H at increasing temperatures. Simultaneously, the NE2 and NE3 EPR lines appear after the anneal at 1900°C and raise in intensity with the heat treatment at 2000°C. Thus, the observed changes on the NE1 and NE2 spectra intensity agree with the proposal that the NE1 defect gives rise to the NE2 center by capture of a third nitrogen atom. Regarding the NE3 defect, it is supposed that this center is generated by the aggregation of a nitrogen atom to the NE5 defect (Nadolinny *et al.*, 1999). Although the NE3 center was detected after the anneal at 1900°C, we did not measure the NE5 EPR lines at any stage of the annealing. It is likely that in this sample the NE5 center exist in other charge state which is undetectable by EPR. Originally the NE5 center was believed to be detectable solely upon illumination of the samples (Nadolinny and Yelissev, 1994), which means that, the most stable charge state was not that of the NE5 paramagnetic center.

The annealing data summarized in Table 5.1 provide the evidence that the decrease in the concentration of W8 defects is not accompanied by an equal increase on the concentration of the nickel-nitrogen defects NE1, NE2, and NE3. There is a large discrepancy between the as-grown concentration of W8 centers and the sum of the concentrations of the NE2 and NE3 defects measured after the annealing at 2000°C. The determined center concentrations clearly shown that through the mechanism proposed by Nadolinny *et al.* (1999) for the formation of the NE centers not all W8 centers transform into the paramagnetic NE centers. The  $\text{Ni}_5^-$  defects also generate other centers, which may be NE defects in another charge state with spin  $S = 0$  or may be different defects with other structures. The AB1, AB3, and AB6 defects are obvious candidates, since it is shown that they are produced upon annealing at intermediate temperatures and anneal out at higher temperatures of the heat treatments.

As mentioned above, Nadolinny *et al.* (1999) put forward the idea that the NE4 center, formed in the process of the creation of interstitial carbon atoms by substitutional  $\text{Ni}_5^-$  centers (W8), is the basic structure of the NE1-NE3 and NE5 nickel-nitrogen centers. In Section 3.4, we have shown that no EPR signals from NE4 centers were detected in the studied set of HPHT crystals. Moreover, neither the sample J nor the sample H evidence the appearance of this defect at any stage of the annealing sequence. In spite of this, the defects NE1, NE2, and NE3, which are presumably generated by the NE4 center, were proved to be created in sample H with detectable concentrations upon the heat treatments. This observation is a strong indication that the defect which gives rise to the nickel-nitrogen paramagnetic centers, and that is their common unit fragment in the model proposed by Nadolinny *et al.* (1999),

does not correspond to the NE4 EPR spectrum. However, the hyperfine structure of  $^{13}\text{C}$  studied by Nadolinny *et al.* (1999) for the nickel-nitrogen centers seems to confirm the model of a nickel ion positioned in the center of a double semivacancy  $\text{NiVC}_6$  as being the correct common fragment of the NE defects. Such a structure would result in the defect with  $D_{3d}$  symmetry shown in Figure 5.2. Nadolinny *et al.* (1999) argued that this center has a negative charge state in order to be paramagnetic with  $S = \frac{1}{2}$ . However, we believe that such  $\text{NiVC}_6$  structure can exist in more than one charge state, which may not obligatory have a non-zero spin. Further, we suggest that among the so far observed nickel-related EPR spectra, the AB1 spectrum is the best candidate to be related to a paramagnetic charge state of the  $\text{NiVC}_6$  defect structure.

The reason for the deviation from second order kinetics observed in the aggregation of nitrogen upon annealing of nickel-containing diamond at high temperature is still unknown (see Subsection 1.7.1). Among the proposed explanations, one is based on the possibility that in such samples nitrogen is also being trapped by nickel defects (Fisher and Lawson, 1998). This would lead to the formation of nickel-nitrogen complexes, along with the  $A$  aggregates. However, in comparison to the initial concentration of substitutional  $\text{N}^0$  defects, the concentration of nickel-nitrogen centers which involve two or three nitrogen atoms is not significant (see Table 5.1). Therefore, it is unlikely that the formation of the paramagnetic nickel-nitrogen complexes play a fundamental role in the kinetics of the nitrogen aggregation.

## 5.4 THE AB7 PARAMAGNETIC CENTER

### 5.4.1 THE AB7 EPR SPECTRUM

The EPR spectrum in Figure 5.3 shows some new lines labeled AB7. Besides, the single line originating from the W8 center is observed, whereas the lines of the P1 center are suppressed due to saturation effects at the used microwave power. The AB7 lines have a peak-to-peak linewidth of about 0.4 mT and, similarly to the lines belonging to other centers in this sample, exhibit an asymmetrical lineshape. The asymmetrical lineshape is caused by fluctuations on the magnetic field distribution throughout the sample, which is created by an inhomogeneous distribution of metallic inclusions with non-negligible  $\chi''$  in the diamond. The effect produced on the EPR spectrum by high magnetic susceptibility materials adjacent

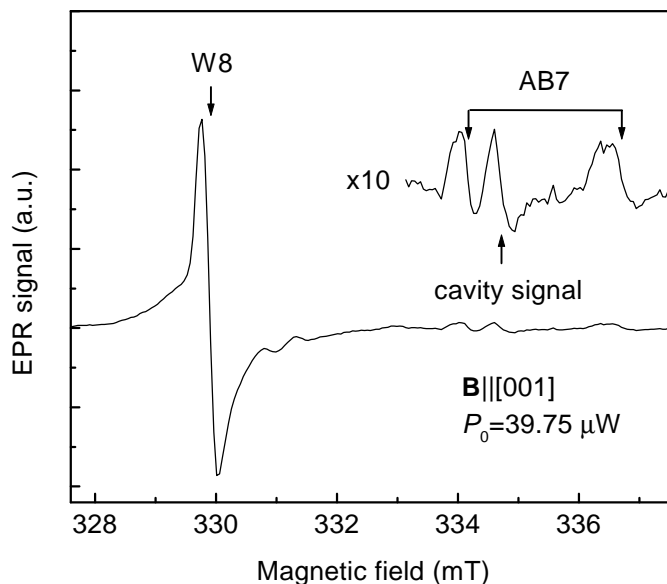


**Figure 5.3:** EPR spectrum of sample J (after the annealing at  $1900^\circ\text{C}$ ) for  $\mathbf{B} \parallel \langle 001 \rangle$ , obtained at 50 K and using a microwave frequency of  $\nu = 9.3950$  GHz. The spectrum shows, apart from the single line originating from the W8 center, some weak new lines labeled AB7, which are zoomed in the insert. The EPR line between the two AB7 lines is due to the resonator.

to a paramagnetic center was investigated by Sueki *et al.* (1993). The appearance of metallic inclusions in HPHT diamond grown with metal solvents have been extensively reported in the literature (Field, 1992). Such inclusions produce also a considerable reduction of the quality factor of the resonator since they possess a dielectric constant with non-zero imaginary part  $\epsilon''$ . This effect led consequently to a significative decrease of the sensitivity (see Subsection 2.1.7).

As usual, the anisotropic properties of the EPR lines were studied by rotating the external magnetic field in an  $\{110\}$  plane, which comprises the three main crystallographic directions  $\langle 110 \rangle$ ,  $\langle 111 \rangle$ , and  $\langle 001 \rangle$ . The angular dependence of the AB7 EPR line positions is shown in Figure 5.4. The plot shows that each one of the two lines detected when the magnetic field is aligned along a  $\langle 001 \rangle$  direction is split into two lines for arbitrary magnetic field directions. This means that the AB7 EPR spectrum is formed by four anisotropic lines. Not any additional splitting of the AB7 lines was observed. For a rotation in an  $\{110\}$  plane such a

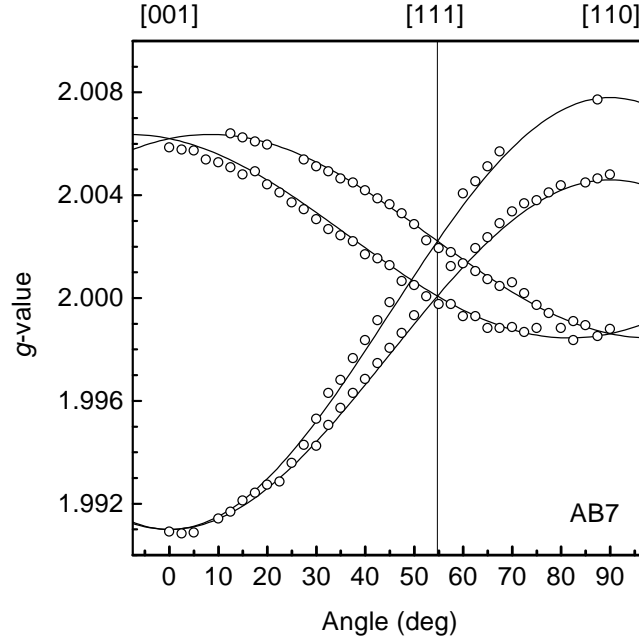


**Figure 5.4:** Angular dependence of the AB7 EPR lines by rotation of the magnetic field in an  $\{110\}$  plane. The open points represent the experimental data and solid lines are the angular dependencies calculated from a spin Hamiltonian containing only the anisotropic Zeeman interaction and using  $g$ -values given in Table 5.2.

spectrum pattern corresponds to a system with orthorhombic symmetry. This statement can be easily verified by comparing the experimental angular dependence with those calculated using the spin Hamiltonian (4.1), which contains only the anisotropic Zeeman term. The solid lines shown in Figure 5.4 were calculated with the  $g$ -values given in Table 5.2 assuming a defect with orthorhombic-I symmetry and a spin  $S = \frac{1}{2}$ . Owing to the good agreement

**Table 5.2:** Spin Hamiltonian parameters of the new AB7 defect in diamond.

Center	Symmetry	Spin	$g$ -values	$\Delta B_{pp}$ (mT)
AB7	Rhombic-I	$\frac{1}{2}$	$g_1 = 1.9910(5) \parallel [100]$	$0.4 \pm 0.1$
			$g_2 = 2.0078(5) \parallel [011]$	
			$g_3 = 2.0046(5) \parallel [0\bar{1}1]$	

between the simulated curves and the experimental data we conclude that the detected EPR lines are due to an orthorhombic-I defect.

#### 5.4.2 NATURE OF THE AB7 DEFECT

Similar arguments like in the discussion of the nature of the other AB centers are used to speculate about the AB7 center. The magnitude of deviation of the principal  $g$ -values from the free electron value  $g_e$  is indicative of a relatively strong spin-orbit coupling. This observation may imply that the AB7 involves an impurity atom. Thus, it is a reasonable assumption that the detected defect contains a transition metal ion. However, unlike the other AB paramagnetic centers, the mean  $g$ -value of the AB7 defect is less than  $g_e$ . Transition metal ions having a less than half-filled shell have typically  $g < g_e$ , whereas  $g > g_e$  are found for transition metals with a more than half-filled shell (see Subsection 2.1.2). In addition, it is observed that two of the principal  $g$ -values are greater and one is smaller than this value. The measured set of  $g$ -values is similar to that typically measured for  $d$ -shell ions with electronic configuration  $d^5$  in a strong octahedral crystal field (Abragam and Bleaney, 1970; Pilbrow, 1990). In such a case the  $t_2$  orbitals are expected to lie lower in energy than the  $e$  states. Moreover, the filling of states should be made in a way that the  $e$  states are occupied only after the  $t_2$  orbitals are completely filled, since the strong crystal field makes that the  $e$  states lie very high above the  $t_2$  subset. Here, the Hund's rule is not observed, giving rise of a low spin state. Thus, for a  $d^5$  ion the 5 valence electrons go into the  $t_2$  states originating a  $t_2^5$  configuration with electron spin  $S = \frac{1}{2}$ . The strong crystal field approach has been applied to transition metal ions in diamond by Twitchen *et al.* (2000) and Nadolinny *et al.* (1999). Some other studied transition metal centers have the same spin value for the strong and intermediate crystal field approaches (Isoya *et al.*, 1990*a,a*; Mason *et al.*, 1999).

Abragam and Bleaney (1970) give expressions for the principal  $g$ -values of a strongly bonded octahedral complex of  $t_2^5$  with an arbitrary distortion. These equations are as follows:

$$g_1 = \cos^2 \theta \{g_e \sin^2 \phi - (g_e + 2\kappa) \cos^2 \phi\} + \sin^2 \theta (2\kappa - g_e), \quad (5.4)$$

$$\frac{1}{2}(g_2 + g_3) = -\cos^2 \theta \{g_e \sin^2 \phi + 2\sqrt{2}\kappa \cos \phi \sin \phi\}, \quad (5.5)$$

$$\frac{1}{2}(g_2 - g_3) = -\sin 2\theta \{g_e \cos \phi + \sqrt{2}\kappa \sin \phi\}. \quad (5.6)$$

The parameters  $\phi$  and  $\theta$  describe the admixture of  $t_2$  orbitals in the ground state and depend on the crystal field.  $\kappa$  is an orbital reduction factor, which accounts for the fact that the spin-orbit coupling parameter is reduced in the crystal as compared with the free ion value. Here the  $g$ -values were calculated using the Equations (5.4) to (5.6) for  $\kappa = 1$ . The best agreement between our measured values in Table 5.2 and those calculated,

$$g_1 = -1.9906, \quad g_2 = -2.0074, \quad g_3 = -2.0042, \quad (5.7)$$

is afforded with  $\phi = 35.367^\circ$  and  $\theta = -0.0187^\circ$ . Although a paramagnet may have effective  $g$ -values which are positive or negative, from Equations (2.46) and (2.47) it is clearly seen that through common EPR experiments we have not access to the sign of these values. From the good fit between the module of the two sets of  $g$ -values it is reasonable to assume that the AB7 defect is produced by a  $3d^5$  transition metal ion in a strong octahedral crystal field which has undergone a small distortion to orthorhombic-I symmetry. Alike the other AB paramagnetic defects, the most probable transition metal to be involved in the AB7 defect is nickel.

## 5.5 SUMMARY

The formation and anneal out conditions of paramagnetic defects in HPHT diamond were comprehensively investigated through an annealing study of as-grown crystals. It is found that substitutional  $N^0$  and  $Ni^-$  defects show a similar behavior when diamond samples are subjected to high temperature heat treatments. NIRIM1 defects reveal a significant decrease in concentration upon annealing at temperatures higher than  $1900^\circ\text{C}$ , whereas the NIRIM2 EPR spectrum is shown to be rather insensitive to the heat treatments. Unlike the NIRIM1 center, the NIRIM2 defect seems to correspond to a rather stable configuration of nickel in the diamond lattice.

A new paramagnetic defect named AB7 was detected upon annealing diamond crystals with low nitrogen concentration. The anisotropic properties of the EPR line positions of the AB7 spectrum are consistent with a spin  $S = \frac{1}{2}$  system with orthorhombic-I symmetry. Owing to the deviation of the measured  $g$ -values from  $g_e$ , it is assumed that the AB7 defect contains a transition metal ion, perhaps nickel. A quantitative analysis of the measured  $g$ -values shows that the center probably corresponds to a  $3d^5$  ion in a strong octahedral crystal field distorted to orthorhombic-I symmetry with configuration  $t_2^5$ .

It is found that the AB5 centers occur in as-grown HPHT diamonds rich in nitrogen and that their concentration is decreased upon heat treatments. A similar mechanism like to the previously proposed by Nadolinny *et al.* (1999) to justify the behavior of the substitutional  $\text{Ni}^-$  defects upon annealing explains the decrease of the concentration of AB5 centers upon the heat treatments.

AB1, AB3, and AB6 centers exhibit a transitory behavior upon heat treatment of diamond crystals rich in nitrogen. These defects are possibly products of the generation of carbon interstitials that are supposed to enhance the nitrogen aggregation. The AB6 centers are only produced in detectable concentrations upon annealing of the samples, whereas the AB1 and AB3 defects are also detected in some high nickel-content as-grown crystals.

The detection of the NE1, NE2, and NE3 paramagnetic defects after annealing of one HPHT diamond with high nitrogen content corroborates the observations, previously reported by Nadolinny *et al.* (1997), that the nickel-nitrogen complexes are produced upon annealing of this type of crystals. However, the absence of the NE4 EPR spectrum at any annealing stage of the same sample yields the proposal that the paramagnetic charge state of the defect giving rise to the nickel-nitrogen complexes is the AB1 center.

It is unlikely that the formation of nickel-nitrogen paramagnetic defects during high temperature heat treatments of HPHT diamond is responsible for the deviation of the annealing behavior of nitrogen from second order kinetics.

# CHAPTER 6

## PHOTO-EPR OF NICKEL-RELATED CENTERS

### 6.1 INTRODUCTION

The interest in the study of transition metals does not result solely from their use during the growth process, but also from the possible variety of energy levels that the different charge states of one defect may induce in the energy gap. The appearance of such levels alter the optical and photoelectrical properties of synthetic HPHT diamond.

Contrary to the appreciable amount of information concerning the formation conditions and structure of the nickel-related centers, there is little knowledge on their energy levels in the energy gap. Concerning paramagnetic centers, these may be determined through electron paramagnetic resonance measurements upon photoexcitation (photo-EPR), as described in Section 2.2. Only for the substitutional  $\text{Ni}_s^-$  center an ionization energy of 2.5 eV has been determined from photo-EPR measurements (Hofmann *et al.*, 1994). It was suggested that this level is located at 3.0 eV above the valence band. Also Nadolinny *et al.* (1997) have recently performed EPR measurements associated with optical excitation. Their investigations yield the detection of two paramagnetic centers labeled NE6 and NE7, which are only detected upon illumination of the samples.

With the aim of investigating the defect level positions of the Ni-related centers in the diamond energy gap, we carried out photo-EPR measurements on several of these defects which are commonly detected in as-grown and annealed diamonds (Pereira *et al.*, 2001*a,b*, 2002*a*). This chapter is organized as follows. In Section 6.2, some details about the mod-

ifications implemented in a standard EPR spectrometer that permitted the measurement of photo-EPR are given. In addition, the method used in the investigations to obtain the spectral dependence of the optical cross section of a photoionization transition from photo-EPR data is also described. In Section 6.3, we deduce the rate equations describing the photoinduced effects produced during a photo-EPR experiment. A detailed study of the W8 center photoionization is given in Section 6.4. In this section, we conclude as well about the relaxation of this defect upon electron ionization. In Sections 6.5 and 6.6, the photo-EPR data obtained for the NIRIM1 and AB centers, respectively, are presented and discussed. These investigations led us to inquire about the defect level locations of the NIRIM1 and the AB centers in the energy gap. Additionally, we comment on some characteristics of the detected nickel-containing defects. In Section 6.7, we discuss about the role of nitrogen in the observed photoresponse of the nickel-related defects. Finally, a summary of the main results obtained in the photo-EPR investigations is given.

## 6.2 EXPERIMENTAL DETAILS

### 6.2.1 DIAMOND SAMPLES

In the photo-EPR measurements we used HPHT synthetic samples grown by the temperature gradient method at the National Institute for Research in Inorganic Materials (NIRIM), Japan. The stones were grown at temperatures in the range 1400 – 1500 °C using nickel or an alloy of Ni and Ti as solvent/catalist (see Table 3.1). Some samples suffered a post-growth annealing at approx. 1600 °C under a stabilizing pressure of 6 GPa (samples F and G of Table 3.1).

### 6.2.2 PHOTO-EPR EQUIPMENT

Continuous wave EPR measurements upon photoexcitation were performed using the  $Q$ -band spectrometer described above (see Subsection 3.4.1). The photo-EPR experiments were carried out in the  $Q$ -band owing to the better resolution, as compared to the  $X$ -band, enabling us to monitor non-overlapping lines, and due to the higher sensitivity taking into account the small size of the available diamond samples. In Subsection 2.1.7 was pointed out that the filling factor  $\eta$  increases with the ratio between the volume of the sample

and the volume of the cavity. Thus, since the  $Q$ -band cavity is considerably smaller than the  $X$ -band resonator,  $\eta$  increases when we go from the  $X$ -band to the  $Q$ -band microwave frequency. Then, provided that the factor  $Q$  is not significantly decreased due dielectric losses, which result from an increase of the electric component of the microwave field in the sample, the sensitivity should be increased (see Equations (2.61), (2.62), and (2.68)). The use of the  $Q$ -band cryostat is also advantageous as it prevents any unintentional infrared irradiation of the samples, since all the resonator insert is kept at low temperature. This is not the case in the flow cryostat standardly used in the  $X$ -band measurements, where the cavity walls are kept at room temperature. In Figure 6.1 is shown a scheme of the optical setup used in the photo-EPR experiments. For measuring photo-EPR, the samples were illuminated through a 0.4 mm optical fibre  $F_2$  which was placed into an home made cryostat insert CI. This insert was introduced from the top into the  $Q$ -band helium cryostat, substituting the cryostat insert that is standardly supplied by the cryostat manufacturer. The sample holder SH was made of a thin synthetic quartz tube and was fixed at the end of the insert CI. The end of the optical fiber  $F_2$  is put close to the sample through the sample holder SH. In this way, part of the optical fibre is also positioned inside the resonator during the measurements. Care was taken in order to avoid a misinterpretation of an EPR signal from the fiber  $F_2$ . As monochromatic irradiation source we used light from a 100 W Xe lamp L dispersed by a grating monochromator M. The light was then coupled into another 0.4 mm optical fibre  $F_1$ , at the end of which the spectral dependence of the photon flux was measured. The measurement of the light power was made by means of a solid state detector D based on a silicon crystal. The fibres  $F_1$  and  $F_2$  were connected when the samples were to be illuminated.

### 6.2.3 PHOTO-EPR: SATURATION METHOD

A major scope of photo-EPR experiments is the determination of the ionization energy of localized states. This can be obtained from the spectral dependence of the optical cross section  $\sigma(h\nu)$ . The requirements for a correct determination of this dependence from the photo-EPR data were extensively discussed by Godlewski (1985). The applicability of a definite method is essentially determined by the time-dependence of the involved processes. In the temperature range of our measurements, the photoinduced changes of the defect level population were metastable and it was difficult to ensure the same starting population for

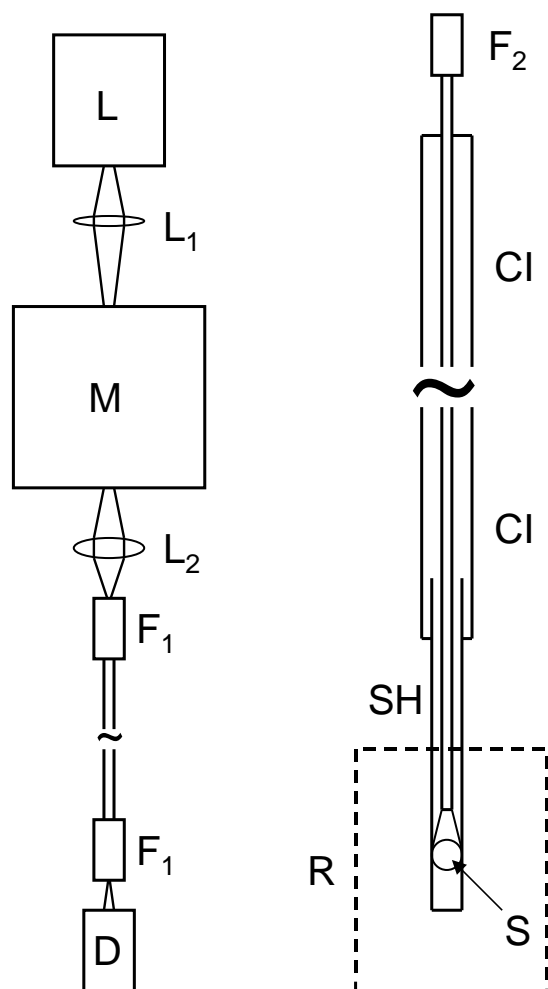


**Figure 6.1:** Scheme of the optical setup used in the photo-EPR measurements: L - Xe lamp; M - monochromator; F<sub>1</sub> and F<sub>2</sub> - optical fibres; D - detector; CI - cryostat insert; SH - sample holder; S - sample; L<sub>1</sub> and L<sub>2</sub> - lenses.

the center under study prior to each subsequent photoexcitation. Therefore, we used the *saturation method*, which is based on the determination of the difference  $\Delta I_{\text{EPR}}$  between the EPR signal intensity  $I_{\text{EPR}}$  measured prior to illumination with a certain wavelength and its photoinduced saturation value and allows, in a simple way, the consideration of different starting populations. With the external magnetic field being fixed at the position of maximum intensity of the first derivative of the corresponding EPR absorption line, the time-dependence of  $I_{\text{EPR}}$  upon an illumination sequence with increasing photon energies was

measured (see Figure 6.2). The time-dependence of the EPR signal intensity was measured

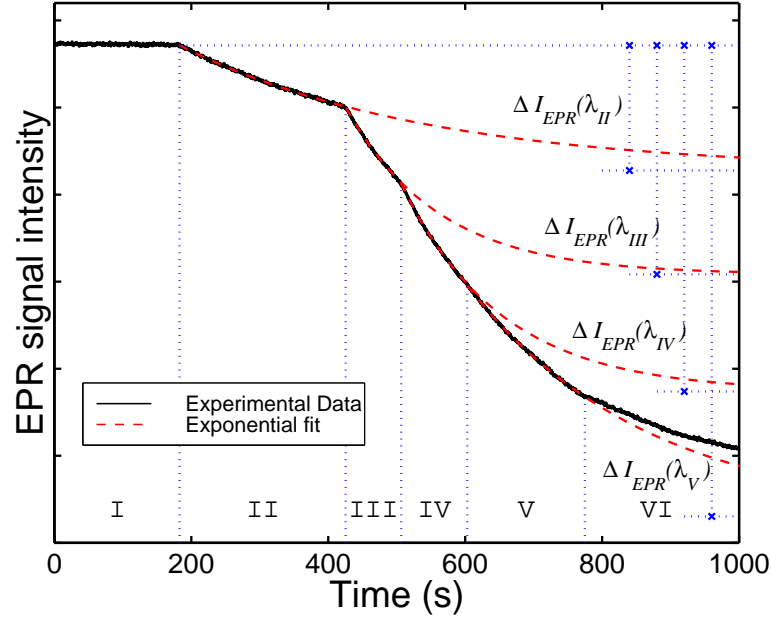


**Figure 6.2:** Time-dependence of the EPR signal intensity  $I_{\text{EPR}}$  of the AB5 center at  $T = 60$  K for different excitation energies  $h\nu$  (eV) = 1.87 (I), 1.96 (II), 2.06 (III), 2.15 (IV), 2.23 (V), and 2.32 (VI). Full curves represent experimental data and dashed curves are exponential fits. Horizontal lines represent the saturation values obtained from the fits. The vertical bars represent the  $\Delta I_{\text{EPR}}$  values used for the determination of the optical cross sections.

using the time sweep option on the EPR spectrometer. The spectral dependence of  $\Delta I_{\text{EPR}}$  for the center under study was then estimated through fitting the data by exponential decay functions and their values corrected by the corresponding previously measured photon flux.

In the framework of the saturation method, we must then find the relation between  $\Delta I_{\text{EPR}}$  and the optical cross section  $\sigma$  of the photoionization transition which induces the changes in the intensity of the EPR signals. A complete description of the dependence of  $\Delta I_{\text{EPR}}$  on  $\sigma$  requires the solution of a complex system of kinetic equations that would consider all excitation, recharging and capture processes occurring at the levels involved. In practice, different approaches are used to simplify the kinetic equations and facilitate their solution. For the moment we will analyze this issue from an experimental point of view. In the following section a more detailed theory of the photoionization kinetics will be given. The

time-dependence of the population of a given center X, neglecting carrier recombination and thermal emission, can be described by the equation

$$\frac{dn_X}{dt} = I\sigma_p^X (N_X - n_X) - I\sigma_n^X n_X + C_n^X n (N_X - n_X) - C_p^X p n_X, \quad (6.1)$$

where  $n_X$  is the concentration of centers X in the hole ionized charge state and  $N_X$  is the total concentration of defects X in both charge states.  $\sigma_n^X$  and  $\sigma_p^X$  are the optical cross sections of the two complementary photoinduced transitions involving the defect X, i.e., electron promotion from the impurity level to the conduction band (CB) and hole ionization from the impurity level to the valence band (VB), respectively.  $C_n^X$  and  $C_h^X$  are the capture rates of electrons and holes by the impurity, respectively.  $I$  is the photon flux;  $n$  and  $p$  are the numbers of free electrons and holes, respectively. The analysis of the photoinduced processes can be simplified when only one of the defects in the sample is photoionized by the incident light and when, besides, the photon energy induces transitions between the defect level and only one of the allowed energy bands. In such a case, the overall kinetic process depends on the light intensity only through one of the  $\alpha_i = I\sigma_i$  ( $i=n, p$ ) values. Thus, a very simple principle can be applied to determine the dependence of the  $\Delta I_{\text{EPR}}$  values on  $\sigma$ , since  $\Delta I_{\text{EPR}}$  has the same dependence on  $I$  and on the particular  $\sigma$ . By determining the dependence of  $\Delta I_{\text{EPR}}$  on  $\alpha$ , through fixing  $\sigma$  (i.e. the photon energy  $h\nu$ ) and measuring  $\Delta I_{\text{EPR}}$  for increasing  $I$  values, we determine also the dependence of  $\Delta I_{\text{EPR}}$  on  $\sigma$  for a particular interval of  $\alpha$  values. Figure 6.3 shows the change of  $\Delta I_{\text{EPR}}$  versus  $\alpha$ , for the case of the photoinduced quenching of the W8 EPR signal intensity, which was measured in such a way with  $h\nu = 2.72$  eV. It is found that  $\Delta I_{\text{EPR}}$  varies linearly with  $\alpha$  for low  $\alpha$  values (i.e., low light intensity) and saturates for higher  $\alpha$  values. Vice-versa, for a constant photon flux  $I$ , the saturation is achieved for large cross sections  $\sigma$  (i.e., higher photon quanta  $h\nu$ ). In the linear regime,  $\Delta I_{\text{EPR}}$  is directly proportional to the corresponding optical cross section  $\sigma$ . In the present work, only  $\Delta I_{\text{EPR}}$  values obtained under experimental conditions of a linear dependence between  $\Delta I_{\text{EPR}}$  and  $\alpha$  are considered, which consequently corresponds to a regime where  $\Delta I_{\text{EPR}}$  is linearly dependent on  $\sigma$ .

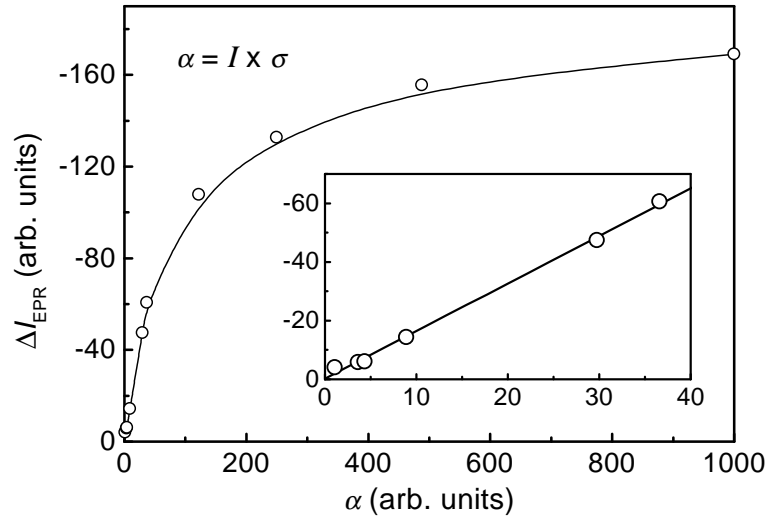


**Figure 6.3:** (a) Dependence of the quenching of the W8 EPR signal ( $\Delta I_{\text{EPR}}$  as defined in Figure 6.2) versus  $\alpha = I\sigma$ . The photon energy was fixed at  $h\nu = 2.72$  eV and the light intensity varied. The circles represent experimental values and the full curve is a guide for the eyes only. (b) The same dependence for small  $\alpha$  values. The full curve is a linear fit to the data.

### 6.3 PHOTOIONIZATION KINETICS

The photoionization energy of localized states can be obtained from the spectral dependence of the corresponding optical cross section  $\sigma$ . Methods for the determination of the spectral dependence of  $\sigma$  through the kinetics of a photoionization transition were reviewed by Godlewski (1985). In the present work we used the saturation method, which is based on the determination of  $\sigma(h\nu)$  from the spectral distribution of the photoinduced changes  $\Delta I_{\text{EPR}}$  produced on the EPR signal intensity  $I_{\text{EPR}}$  of the detected center. As mentioned above, the description of all excitation, recharging and capture processes occurring during a photoionization experiment requires the solution of a complex system of kinetic equations. Godlewski (1985) studied the photoionization processes which take place during a photo-EPR experiment and determined the relations between  $\Delta I_{\text{EPR}}$  and  $\sigma$  for a few experimental situations. However, the formalism does not account for the situation of having simultaneously two different electron traps, involving distinct physical processes. Thus, here,

we consider the case of electron ionization of a defect X with optical cross section  $\sigma_n^X$  and electron capture rate  $C_n^X$  (see Figure 6.4).  $N_X$  and  $n_X$  are the total concentration of defects

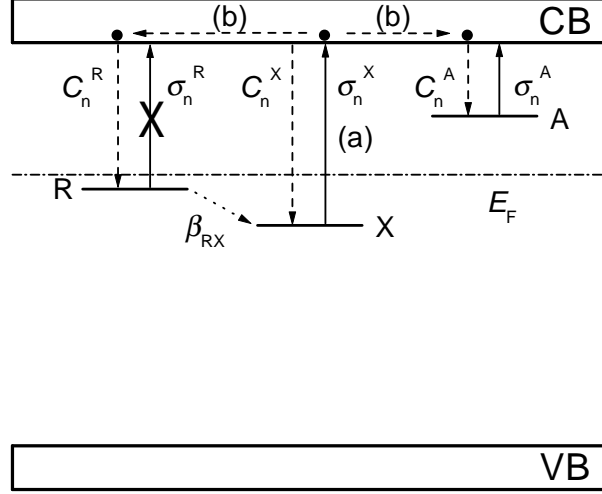


**Figure 6.4:** Diagram of the processes which may occur during an electron photoionization experiment of a given defect X. Intercenter recharging was taken into account through centers R, for which the non-ionized charge state has the dark concentration  $n_R^0$ , whereas centers A behave as electron trap levels. The photoinduction of an EPR signal may result from a direct photoionization mechanism (a) or, alternatively, may occur through an indirect process of free carrier capture (b).

X and the concentration of centers X in the non-ionized charge state, respectively. Taking into account intercenter electron transfer (recharging) through defects R ( $[R]=N_R$ ) and free carrier capture by trap centers A ( $[A]=N_A$ ), as shown schematically in Figure 6.4, the kinetic equations which describe the photoionization process are:

$$\frac{dn_X}{dt} = -I\sigma_n^X n_X + C_n^X n(N_X - n_X) + \beta_{RX}(N_X - n_X)n_R, \quad (6.2)$$

$$\frac{dn_R}{dt} = C_n^R n(N_R - n_R) - \beta_{RX}(N_X - n_X)n_R, \quad (6.3)$$

$$\frac{dn_A}{dt} = -I\sigma_n^A n_A + C_n^A n(N_A - n_A), \quad (6.4)$$

$$\frac{dn}{dt} = I\sigma_n^X n_X - C_n^X n(N_X - n_X) - C_n^R n(N_R - n_R) + I\sigma_n^A n_A - C_n^A n(N_A - n_A). \quad (6.5)$$

In these equations  $n$  represents the concentration of free carries in the conduction band and  $C_n^R$  and  $C_n^A$  are their capture rates by centers R and A, respectively.  $n_R$  and  $n_A$  are the

concentrations of defects R and A in the non-ionized charge state, respectively.  $\sigma_n^A$  is the cross section of the photoionization transition involving the trap centers A, and  $I$  is the light intensity.  $\beta_{RX}$  accounts for the direct transfer of electrons from R to X. In thermal equilibrium, and assuming that the Fermi energy is close to the R center defect level, the dark concentration of ionized trap centers would be  $N_A$  and the amount of defects X in the photoinduced charge state would be zero. In Equations (6.2) to (6.5) we assumed that the recharging centers R are not ionized by the incident light. As we shall see later, this assumption is well justified for cases where the dominant defect, and consequently the one that determines the Fermi energy level, has a large difference of the thermal and optical ionization energies.

Assuming that a steady-state amount of excited electrons  $n$  is obtained on a very short time scale as compared to the time required to obtain a sensitive change in the EPR signal (Godlewski, 1985), we may solve Equation (6.5) independently, getting under stationary conditions:

$$n = \frac{\alpha_n^X N_X}{C_n^R(N_R - n_R^0) + C_n^A N_A}, \quad (6.6)$$

where  $\alpha_n^X = I\sigma_n^X$  and  $n_R^0$  is the amount of non-ionized recharging centers before illumination. Substituting the obtained expression for  $n$  in Equations (6.2) to (6.4) and solving the set of equations under stationary conditions, we obtain the following results for the saturation values of the light induced changes produced in the occupancies of the non-ionized charge state of the centers X ( $\Delta n_X$ ), R ( $\Delta n_R$ ) and A ( $\Delta n_A$ ):

$$\Delta n_X = \frac{N_X}{N_R - (n_R^0 - \lambda)} \times \left\{ \frac{\alpha_n^X}{2\beta_{RX}} + \frac{n_R^0 - \lambda}{2\Lambda} - \sqrt{\left(\frac{\alpha_n^X}{2\beta_{RX}}\right)^2 + \left(\frac{n_R^0 - \lambda}{2\Lambda}\right)^2 + \frac{\alpha_n^X[2N_R - (n_R^0 - \lambda)]}{2\Lambda\beta_{RX}}} \right\}, \quad (6.7)$$

$$\Delta n_R = -\frac{\alpha_n^X \Lambda}{2\beta_{RX}} - \frac{n_R^0 - \lambda}{2} + \sqrt{\left(\frac{\alpha_n^X \Lambda}{2\beta_{RX}}\right)^2 + \left(\frac{n_R^0 - \lambda}{2}\right)^2 + \frac{\alpha_n^X \Lambda[2N_R - (n_R^0 - \lambda)]}{2\beta_{RX}}}, \quad (6.8)$$

$$\Delta n_A = N_A \frac{\sigma_n^X C_n^A (\Lambda - 1)}{\sigma_n^A C_n^X + \sigma_n^X C_n^A (\Lambda - 1)}, \quad (6.9)$$

with

$$\Lambda = 1 + \frac{C_n^X N_X}{C_n^R(N_R - n_R^0) + C_n^A N_A} \quad \text{and} \quad \lambda = \frac{C_n^A}{C_n^R} N_A.$$

## 6.4 SUBSTITUTIONAL NICKEL: W8 CENTER

In a photo-EPR investigation on substitutional  $\text{Ni}^-$  in synthetic diamonds, Hofmann *et al.* (1994) observed a quenching of the W8 EPR signal upon illumination of the samples with photon quanta  $h\nu$  higher than 2.47 eV. The authors suggested that the acceptor level of the W8 center is located at 3.03 eV above the valence band. However, this assignment of the transition requires that the observed photoinduced effect originate from a direct ionization of W8 centers and not from an indirect recharging process. Moreover, the photoionization mechanism may involve electron or hole excitation. With the purpose of clarifying the proposal of Hofmann *et al.* (1994), we performed further photo-EPR measurements on the W8 and P1 centers. In the measurements of the dependence of the W8 EPR signal intensity on the photoexcitation wavelength, diamonds similar to sample L of Table 3.1 were chosen. The EPR spectra of these crystals exhibited only two signals, the W8 line and a weak P1 spectrum.

### 6.4.1 PHOTOEXCITATION OF THE W8 CENTER

Fixing the external magnetic field at the value corresponding to the maximum intensity of the first derivative of the W8 EPR line, the time-dependence of the EPR signal intensity  $I_{\text{EPR}}$  upon an illumination sequence with increasing photon energies was measured. The dependence of  $\Delta I_{\text{EPR}}$  on the magnitude of the photoexcitation quanta, normalized to a constant photon flux, is shown in Figure 6.5. The  $\Delta I_{\text{EPR}}$  values were determined through fitting the time-dependence of  $I_{\text{EPR}}$  by exponential decay functions for each illumination window like shown in Figure 6.2. The EPR signal intensity starts to decrease exponentially at a photon energy threshold of  $\sim 2.5$  eV, in agreement with Hofmann *et al.* (1994). The observed decrease of the W8 line intensity is originated by a photoionization transition occurring on a defect with a localized state in diamond.

It was pointed out that, the spectral dependence of the optical cross section  $\sigma$  of a definite photoionization transition can be determined from the spectral distribution of the photoinduced changes in the EPR signal intensity  $\Delta I_{\text{EPR}}$ . In such a case we must find the relation between  $\sigma$  and  $\Delta I_{\text{EPR}}$ . In the framework of the saturation method, our approach was based on the fact that in the kinetic equations describing the photoionization process, the light intensity  $I$  and the optical cross section  $\sigma$  always appear together in the form of  $\alpha = I\sigma$ .

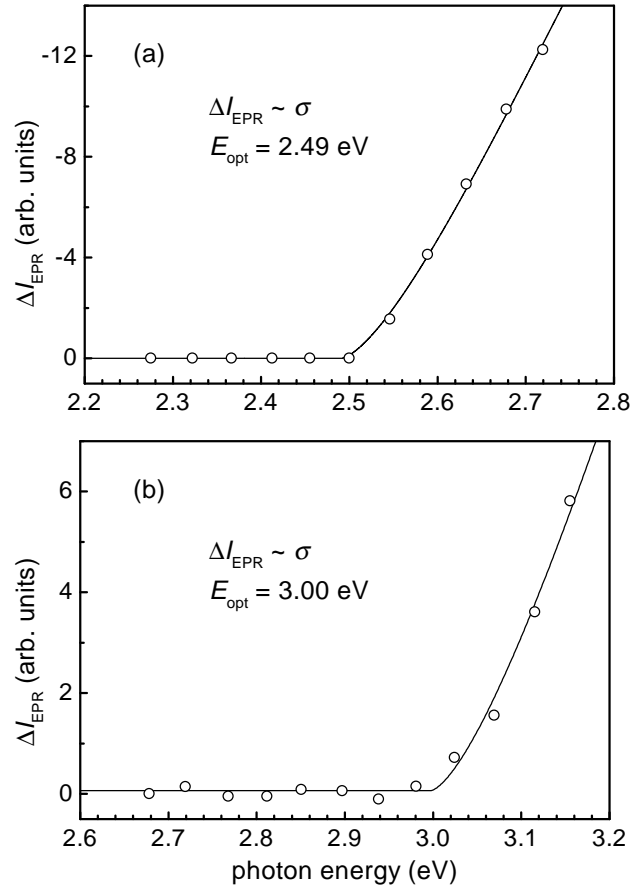


**Figure 6.5:** (a) Dependence of the quenching of the EPR signal ( $\Delta I_{\text{EPR}}$  as defined in Figure 6.2) versus the photon energy for the W8 center, measured at 40 K. (b) Spectral dependence of the recovery of the W8 EPR signal previously quenched by illumination with  $h\nu = 2.72 \text{ eV}$ . In this case,  $\Delta I_{\text{EPR}}$  is measured relatively to the minimum signal intensity achieved after a prolonged illumination. The circles represent experimental values and the full curves are fits to the data by the Lucovsky formula.

This leads to the general characteristic that  $\Delta I_{\text{EPR}}$  depend in the same way on both  $I$  and  $\sigma$ . When the measurements of the photoexcitation process are made under conditions of a linear dependence between  $\Delta I_{\text{EPR}}$  and  $\alpha$  and only one dominating photoionization is considered,  $\Delta I_{\text{EPR}}$  will have a linear dependence on the corresponding optical cross section  $\sigma$  (see Subsection 6.2.3). Taking into account that the data points represented in Figure 6.5 were obtained under the experimental condition of linearity between  $\Delta I_{\text{EPR}}$  and  $\alpha$ , we get

that  $\Delta I_{\text{EPR}}$  is linearly dependent on  $\sigma$  of the involved photoionization transition. The linear behavior of  $\Delta I_{\text{EPR}}$  for small  $\alpha$ , that is generally observed in our photo-EPR measurements on Ni-related defects, will be justified in Section 6.7 through the use of the results deduced in Section 6.3.

Fitting the spectral dependence  $\sigma(h\nu)$  of the W8 excitation by the Lucovsky formula for a purely electronic cross section (Lucovsky, 1965),

$$\sigma_{\text{el}}(E_{\text{opt}}, h\nu) \propto \frac{(h\nu - E_{\text{opt}})^{\frac{3}{2}}}{h\nu^3}, \quad (6.10)$$

the ionization energy  $E_{\text{opt}} = 2.49 \pm 0.03$  eV is found, see Figure 6.5(a).

In order to clarify the nature of the process that causes the changes of the W8 signal intensity, we suppressed the latter to its lowest value by applying an high intensity photoexcitation with  $h\nu \approx 2.7$  eV and then tracked the recovery of the EPR signal intensity upon illumination of the sample with  $h\nu > 2.7$  eV. A threshold energy for which the W8 EPR signal intensity starts to increase exponentially was found, see Figure 6.5(b). The best fit of the experimental data by Equation (6.10) is obtained for  $E_{\text{opt}} = 3.00 \pm 0.05$  eV. This value added up to the previously measured 2.5 eV photoionization threshold matches the 5.5 eV wide bandgap of diamond. In the situation of a very small lattice stabilization energy upon removal of one electron, the second onset may be related with the complementary photoionization transition of the previously observed 2.5 eV transition. A study of the relaxation of the W8 defect upon photoionization is described in the following subsection.

To find out whether the 2.5 eV ionization process observed for the W8 center involves the promotion of electrons to the conduction band or that of holes to the valence band, we monitored the photoinduced changes of the EPR signal intensity of the  $\text{N}_s^0$  deep donor (P1 center), proceeding in a way similar to that described above for the W8 center. Figure 6.6 shows the spectral dependence of the photoinduced enhancement of the P1 EPR signal. The signal intensity starts to increase gradually at photon energies  $h\nu > 2.5$  eV. An indirect process can explain this increase: the illumination induces the photoionization of the W8 center and the electrons promoted to the CB are then captured by the nitrogen. In order to exclude that the photoelectrons are generated through another transition than the 2.49 eV photoionization, the recharging process of the P1 center was investigated in detail. Under the experimental conditions described above, the  $\Delta I_{\text{EPR}}$  values of P1 are proportional to the optical cross section of the involved photoionization transition. Fitting the data in

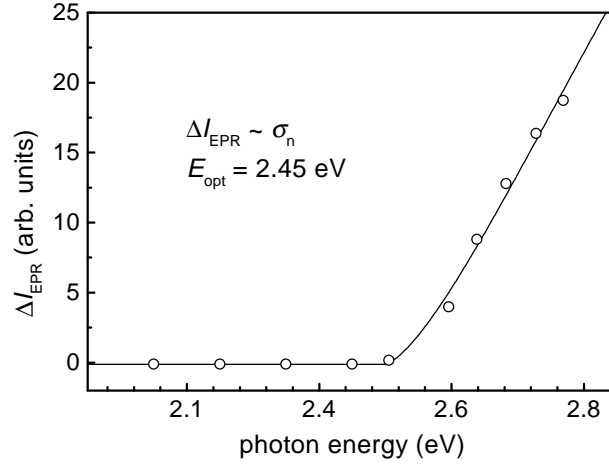


**Figure 6.6:** Spectral dependence of the enhancement of the P1 EPR signal intensity. The circles represent experimental values and the full curves are fits to the data by the Lucovsky formula.

Figure 6.6 by Equation (6.10) we obtain the threshold energy  $E_{\text{opt}} = 2.45 \pm 0.05$  eV, that is in good agreement with the 2.49 eV ionization energy found for the photoquenching of the W8 spectrum. The detection of a recharging of the nitrogen deep donor indicates clearly that the 2.49 eV threshold is related with an electron ionization process ( $\sigma \equiv \sigma_n$ ). This observation means that the involved defect level is localized at 2.49 eV below the conduction band.

#### 6.4.2 TEMPERATURE DEPENDENCE OF THE 2.5 eV PHOTOIONIZATION

From the intensity behavior of the two photoinduced effects observed for the W8 center and as the sum of the two thresholds coincide with the 5.5 eV gap of diamond, they may be interpreted as being the two complementary photoionization transitions occurring at the  $\text{Ni}^{-/0}$  acceptor level. However, this assignment of the transitions requires that the relaxation energy of the system upon removal / filling of one electron is very small. The following analysis of the temperature dependence of the photoexcitation process proves that this assumption is justified. This corroborates the proposal that the photoinduced changes observed in the W8 EPR signal intensity result mainly from the direct photoionization of the substitutional nickel. This should give the ultimate proof of the localization of its defect

level in the energy gap.

Figure 6.7 schematically shows both photoionization transitions related with substitutional nickel in a configuration coordinate (CC) formalism, which considers the adiabatic and Condon approximations. The general considerations of the CC model were described above

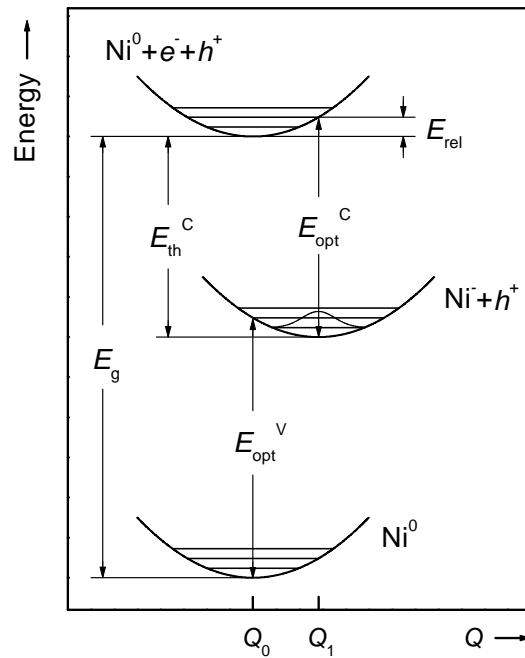


**Figure 6.7:** The configuration coordinate model scheme of the two complementary ionization transitions related with substitutional nickel in diamond.

in Section 2.2.2. Although this model was originally created to describe transitions between localized states, it has been successfully applied to transitions between a localized state and a continuum of states (Monemar and Samuelson, 1978; Samuelson and Monemar, 1978; Kopylov and Pikhtin, 1974; Piekara *et al.*, 1977). The assumption of a linear coupling in the electron-lattice interaction means that the CC diagrams will be made up of parabolas with the same curvature. In such an approach the electron-phonon interaction is generally reflected in a temperature dependent broadening of the photoionization onset. Piekara *et al.* (1977), using a semiclassical approach, proposed the Equation (2.84) given above for the temperature dependent optical cross section  $\sigma$ . The meaning of some of the symbols used in this expression is shown in Figure 6.7.

Fixing the external magnetic field at the value corresponding to the maximum intensity of the first derivative of the W8 EPR line, we measured the time-dependence of the EPR signal intensity  $I_{\text{EPR}}$  upon an illumination sequence with increasing photon energies for different temperatures in the range 20–150 K. Figure 6.8(a) shows the spectral dependence of  $\Delta I_{\text{EPR}}$  produced in the W8 EPR spectrum by the 2.5 eV photoionization transition for three different temperatures and normalized to a constant photon flux. Since the measurements of the photoexcitation process were performed under the conditions of a linear dependence between  $\Delta I_{\text{EPR}}$  and  $\alpha_n$ , and if we assume only one dominating photoionization transition, the corresponding optical cross section  $\sigma_n$  has a linear dependence on  $\Delta I_{\text{EPR}}$ . The best fits of Equation (2.84) to the experimental data for 20 K, 60 K, and 150 K are obtained with  $E_{\text{opt}} = 2.49 \pm 0.03$  eV,  $E_{\text{opt}} = 2.49 \pm 0.02$  eV, and  $E_{\text{opt}} = 2.48 \pm 0.02$  eV, respectively, with  $\Gamma$  being virtually zero for all temperatures. Here,  $\sigma_{\text{el}}$  was substituted by the Lucovsky formula (6.10). Therefore, our experimental data reveal no influence of the temperature on the spectral dependence of the 2.5 eV photoionization, at least in the temperature range of our measurements. This is established by both the vanishing broadening parameter  $\Gamma$  that results from the fitting procedure and the negligible variation in the transition threshold. Thus, this is an evidence of a small energy difference between the optical and thermal ionization thresholds  $E_{\text{rel}} = E_{\text{opt}} - E_{\text{th}}$  (see Figure 6.7) for substitutional  $\text{Ni}^-$  in diamond.

Relying on the CC model, an upper limit for  $E_{\text{rel}}$  can be estimated. In Figure 6.8(b), the spectral dependence of the photoquenching of the  $\text{Ni}^-$  EPR signal close to the transition edge is given. The plotted circles are experimental data obtained at the highest temperature used in the measurements (150 K), for it is the temperature at which we expect the maximum smoothing of the photoionization threshold. The solid line results from the best fit of Equation (2.84) to the experimental data, which gives the parameters  $E_{\text{opt}} = 2.48 \pm 0.02$  eV and  $\Gamma = 0.00 \pm 0.01$  eV. Together, the variations of the optical cross section as calculated by Equation (2.84) using  $E_{\text{opt}} = 2.48$  eV and  $\Gamma = 0.1$  eV (dashed line) and  $\Gamma = 0.04$  eV (dotted line) are represented. By introducing a non-zero  $\Gamma$  value the model predicts a broadening of the photoionization threshold. As follows from Figure 6.8(b), we may assume an upper detection limit of such broadening effect  $\Gamma_{\text{max}}$  of 0.04 eV. From Equation (2.85), and knowing the magnitude of the phonon frequencies  $\omega$  and  $\Omega$ , we can estimate the maximum possible value of the relaxation energy  $E_{\text{rel}}^{\text{max}}$ . The 2.51 eV optical absorption band with a 16.5 meV phonon structure is believed to occur at the substitutional  $\text{Ni}^-$  center (Nazaré *et al.*, 2001). In a linear electron-lattice coupling regime we get  $\hbar\omega \simeq \hbar\Omega = 16.5$  meV, and substituting

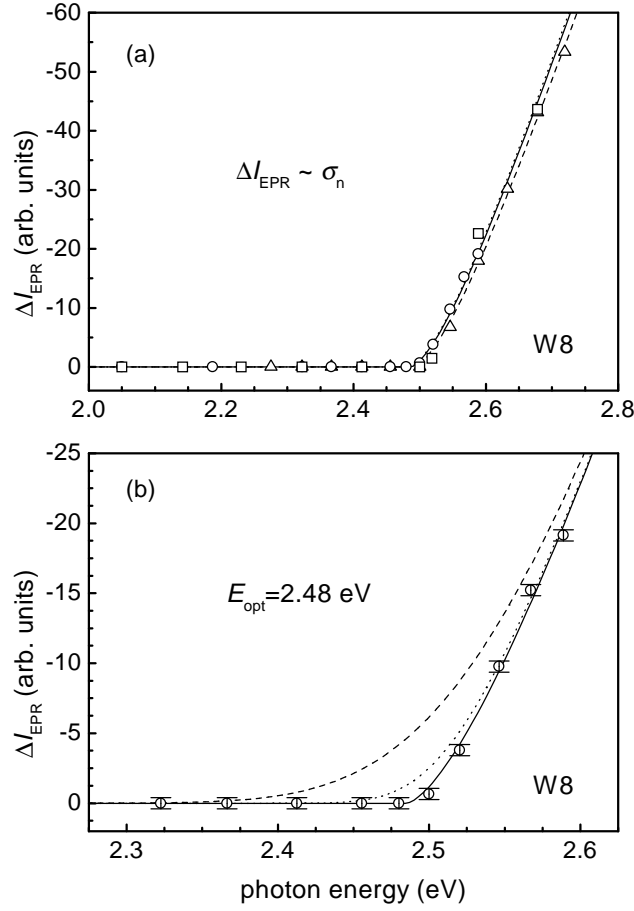


**Figure 6.8:** (a) Normalized spectral dependence of the quenching of the W8 EPR signal produced by the photoionization transition with a threshold at 2.5 eV for 20 K ( $\square$ ), 60 K ( $\triangle$ ), and 150 K ( $\circ$ ). All lines result from the fitting of Equation (2.84) to the experimental data for the following temperatures: 20 K (solid), 60 K (dot), and 150 K (dash). (b) Dependence of  $\Delta I_{\text{EPR}}$  on  $h\nu$  near the transition edge for  $T = 150$  K, normalized to a constant photon flux. Experimental data are represented by circles and the solid line results from fitting the experimental data with Equation (2.84). Dashed and dotted lines are calculated using the same equation with  $E_{\text{opt}}$  obtained from the fitting procedure, and  $\Gamma = 0.1$  eV and  $\Gamma = 0.04$  eV, respectively.

in Equation (2.85) we obtain  $E_{\text{rel}}^{\text{max}} = 0.02$  eV. The small value of  $E_{\text{rel}}$  is an evidence for the modest electron-photon coupling experienced by the substitutional Ni impurity in diamond.

## 6.5 THE NIRIM1 CENTER

The NIRIM1 paramagnetic center was ascribed to the interstitial  $\text{Ni}^+$  defect with electronic configuration  $3d^9$  and spin  $S = \frac{1}{2}$ , giving rise to an isotropic line at  $g = 2.0112$  in the EPR spectra (Isoya *et al.*, 1990b). Although this assignment was not definitely proven, for the sake of simplicity, we will not contest it, as it does not change the meaning of the following discussion.

For studying the photoexcitation processes involving the NIRIM1 center we used green diamonds grown using a nickel solvent with the addition of Ti (similar to samples J and K of Table 3.1). The samples contained typically 12 ppm of substitutional  $\text{N}^0$  centers and around 6 ppm of  $\text{N}^+$  as measured by IR absorption spectroscopy. Their EPR spectra evidenced the presence of only the P1, W8, and NIRIM1 paramagnetic centers, with typical concentrations of W8 and NIRIM1 centers being 3 ppm and 0.2 ppm, respectively. The samples were successively irradiated with increasing photon energies and the consequent changes in the EPR signals intensity were observed. Resulting from the illumination with photon energies between 1.8 eV and  $\sim 2.0$  eV, a small decrease of the NIRIM1 EPR signal intensity is detected. Though we were merely able to measure the P1 lines in fast-passage conditions, in the temperature range where the NIRIM1 line is detectable, an increase of the intensity of the P1 spectrum for the same excitation energies, as well as a slight decrease of the W8 spectrum intensity could be detected. For  $h\nu > 2.0$  eV a comparatively stronger enhancement of the NIRIM1 signal is observed. Such increase takes place in two stages, one upon illumination with  $h\nu > 2.0$  eV and the other  $h\nu > 3.0$  eV. Figure 6.9 shows the spectral dependence of the changes produced in the NIRIM1 EPR signal intensity, measured at 35 K, in the two distinct stages. For irradiation energies  $h\nu > 2.4$  eV the  $\Delta I_{\text{EPR}}$  values saturate, so that, an increase in the photon energy does not produce any further change in the EPR signal. The  $\Delta I_{\text{EPR}}$  values for  $h\nu > 2.6$  eV were measured relatively to this saturation value. In the same samples, the W8 EPR line intensity shows a photoinduced behavior very similar to that described above, with strong decrease and increase for  $h\nu > 2.5$  eV and  $h\nu > 3.0$  eV, respectively.

The changes in the EPR signals intensity observed upon illumination should result from photoionization processes occurring on localized states introduced by defects in the diamond crystal. As already discussed in Section 6.3, these ionizations can occur directly on the defect whose EPR signal is being monitored, or may happen on other defects. In such

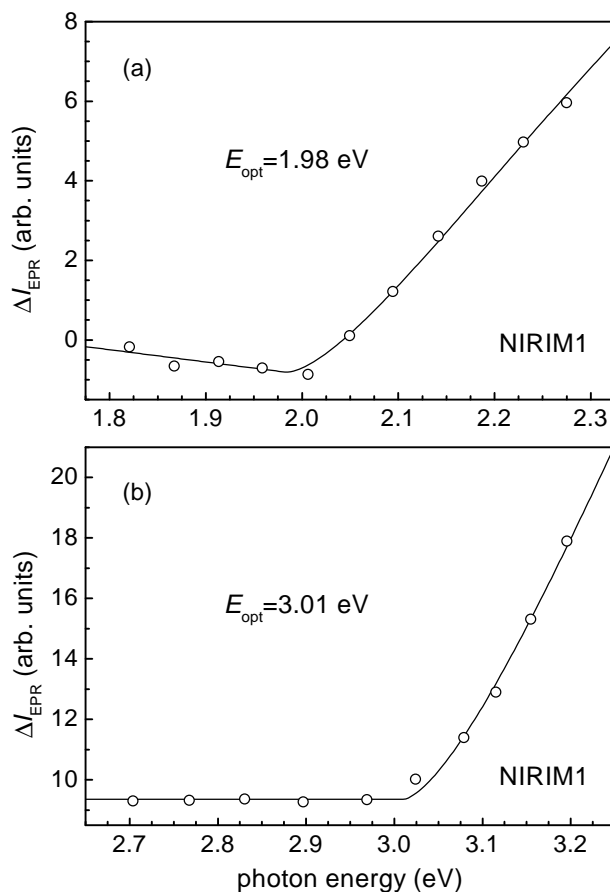


**Figure 6.9:** (a) Spectral dependence of the photoinduced changes in the intensity of the NIRIM1 spectrum, normalized to a constant photon flux. (b) Dependence of the enhancement of the NIRIM1 EPR signal intensity on  $h\nu$  produced by the photoionization transition with a threshold at  $\sim 3$  eV. The circles present the experimental data and the solid lines result from a fitting procedure to these data.

indirect processes, electrons (holes) excited from a defect to the conduction band (valence band) are captured by the monitored center. Additionally, this center may be a recharging path of electrons (holes) to the photoexcited defect. In both situations the  $\Delta I_{\text{EPR}}$  values of the monitored center depend on only one optical cross section  $\sigma$ , if we have non-overlapping photoionization transitions or one dominant photoionization process. The observation of simultaneous changes in the P1, W8, and NIRIM1 EPR lines intensity for  $h\nu < 2.0$  eV suggests that they have one and the same origin. Such a process should not involve neither  $\text{N}^0$

nor  $\text{Ni}^-$  ionization, as their photoionization thresholds are found to be  $E_{\text{opt}} = 2.2$  eV (Rosa *et al.*, 1999) and  $E_{\text{opt}} = 2.5$  eV, respectively. The photoinduced process should involve ionization of another defect. The obvious candidates are the NIRIM1 or another center not detected through the EPR spectra. Moreover, the increase in intensity of the nitrogen deep donor signal (P1 spectrum) points out that the ionization process involves the promotion of electrons to the conduction band. The concentration of NIRIM1 centers in the studied samples is rather low, so it can not induce enough charge carriers that would be captured by nitrogen and nickel to produce the observed changes in their paramagnetic signals. Thus, we come to the conclusion that the charge carriers must arise from another center and the observed photoinduced changes of the concentrations of the paramagnetic defects should result from an indirect photoinduced process. The observation of the P1 EPR signal before illumination indicates that it is probable to have populated defect levels at  $E > E_c - 1.8$  eV, as the thermal ionization energy of the  $\text{N}^0$  state have been taken to be  $E_{\text{th}} = 1.7$  eV (Walker, 1979), see Figure 6.10. While in the  $h\nu < 2$  eV energy range NIRIM1 defects act as electron

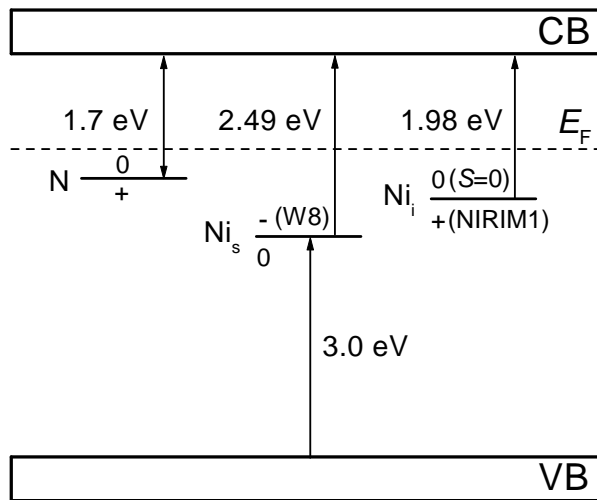


**Figure 6.10:** Diagram of the energy levels of nickel and nitrogen in diamond. The 1.7 eV level correspond to the thermal ionization energy of the nitrogen donor (the optical one is 2.2 eV (Rosa *et al.*, 1999)), while the other levels correspond to optically determined thresholds. Due to the small  $\Gamma$  values of the Ni-related defects, the optically detected levels coincide with the thermodynamic filling levels. Thus, the shown arrangement of the nitrogen and Ni-related defect levels is justified.

traps, the subsequent increase of the signal intensity for  $h\nu > 2$  eV is interpreted as resulting from direct photoionization of interstitial  $\text{Ni}^0$  centers. Such assumption is motivated by the fact that among the detected paramagnetic centers, only the NIRIM1 shows a photoinduced effect setting in at  $\sim 2$  eV excitation. Assuming that above this threshold the kinetics of the photoexcitation of the NIRIM1 center is dominated by its photoionization transition with optical cross section  $\sigma_{\text{Ni}^0}$  and taking into account that  $\Delta I_{\text{EPR}}$  was obtained under conditions of linear dependence between  $\Delta I_{\text{EPR}}$  and  $\alpha_{\text{Ni}^0}$ , we infer that  $\Delta I_{\text{EPR}}$  depends linearly on  $\sigma_{\text{Ni}^0}$ . Fitting the spectral dependence of  $\Delta I_{\text{EPR}}$  for  $h\nu \gtrsim 2.0$  eV by Equation (2.84) with  $\sigma_{\text{el}}$  given by the Lucovsky formula, we obtain a photoionization energy  $E_{\text{opt}} = 1.98 \pm 0.03$  eV and a broadening parameter  $\Gamma = 0$  eV.

It is likely that the process setting in at 3 eV which leads to a further increase of the NIRIM1 signal is the same that results in the observed enhancement of the W8 EPR signal intensity. In this case, interstitial Ni in the neutral charge state behaves as a trap level for holes that were ionized from substitutional  $\text{Ni}^0$ . Fitting the  $\Delta I_{\text{EPR}}$  spectral dependence for  $h\nu$  between 2.6 and 3.2 eV with Equation (2.84), we obtain  $E_{\text{opt}} = 3.01 \pm 0.05$  eV and  $\Gamma = 0$  eV, in good agreement with the values determined for the W8 center in Section 6.4. The observation of this effect on the NIRIM1 center corroborates the interpretation of the first onset at 1.98 eV as resulting from electron ionization.

With the  $\text{Ni}_i^{0/+}$  donor level being localized at 1.98 eV below the conduction band we should expect that all interstitial nickel stays in the neutral charge state in HPHT diamonds, which usually have a concentration of neutral nitrogen higher than the amount of  $\text{N}^+$ . The commonly applied Ludwig-Woodbury model (see Section 2.3) predicts for the  $\text{Ni}_i^0$  state an electronic configuration  $3d^{10}$  with spin  $S = 0$ , not detectable by EPR. The positive charge state was observable in the dark due to fluctuations of the Fermi level resulting from inhomogeneities in the defects distribution, known to occur in this type of samples. This was revealed in the used samples by their inhomogeneous color. The NIRIM1 center is only observed in diamond samples grown with a nitrogen getter or samples doped with boron, where the concentration of  $\text{N}_s$  defects in the neutral charge state is strongly decreased. This produces a lowering of the Fermi level and the  $\text{Ni}_i^+$  state becomes statistically possible to occur, though the concentration of NIRIM1 centers is usually quite low. We observed a substantial decrease in the ratio between the amount of P1 defects and substitutional nitrogen in the positive charge state in diamonds which exhibit the presence of NIRIM1 centers, as com-

pared to other samples. The widespread idea that interstitial nickel is more rarely formed in diamond than in the substitutional form may result from the fact that it is normally incorporated in the neutral charge state, which being non-paramagnetic is not detectable by EPR. Contrarily, substitutional nickel is easily detected as it is incorporated in the negative charge state with an orbital singlet ground state with  $S = \frac{3}{2}$ .

## 6.6 THE AB CENTERS

In order to investigate the energy levels produced by the newly found AB nickel-related centers in diamond, the excitation behavior of their EPR signal was measured using the photo-EPR technique. The diamond samples used for this propose where HPHT diamonds growth with a nickel-containing solvent / catalyst, which exhibit an high nitrogen content. Namely, the samples A to I described in Chapter 3.

### 6.6.1 CENTER AB5

The AB5 center was firstly detected in annealed HPHT diamond samples. This trigonal center has an electron spin  $S = 1$  and was tentatively assigned to a nickel-nitrogen pair in the negative charge state (see Chapter 4). To determine the energy level of the AB5 center in the forbidden gap, photo-EPR investigations similar to those described above for the W8 center were made in four diamond crystals exhibiting sufficient AB5 EPR signal intensity.

The time-dependence of the AB5 signal intensity was recorded at  $T = 60$  K for different photoexcitation energies, as shown in Figure 6.2. From these data we determined the spectral dependence of the  $\Delta I_{\text{EPR}}$  values through fitting the decays with single exponential functions. The variation of  $\Delta I_{\text{EPR}}$  normalized to a constant photon flux is presented in Figure 6.11(a). There is a photon energy threshold of about 1.9 eV for the observed strong decrease of the signal intensity. This threshold is sample independent. All other centers observed in these samples exhibit photoexcitation processes with different spectral dependencies. This indicates that the observed AB5 quenching process occurs due to direct photoionization. Although the presence of other defects in the sample may influence the kinetics of the observed depopulation of the AB5 level they do not change its energy threshold, for the latter results from a direct ionization of the AB5 center. There are only two possible electron transitions,

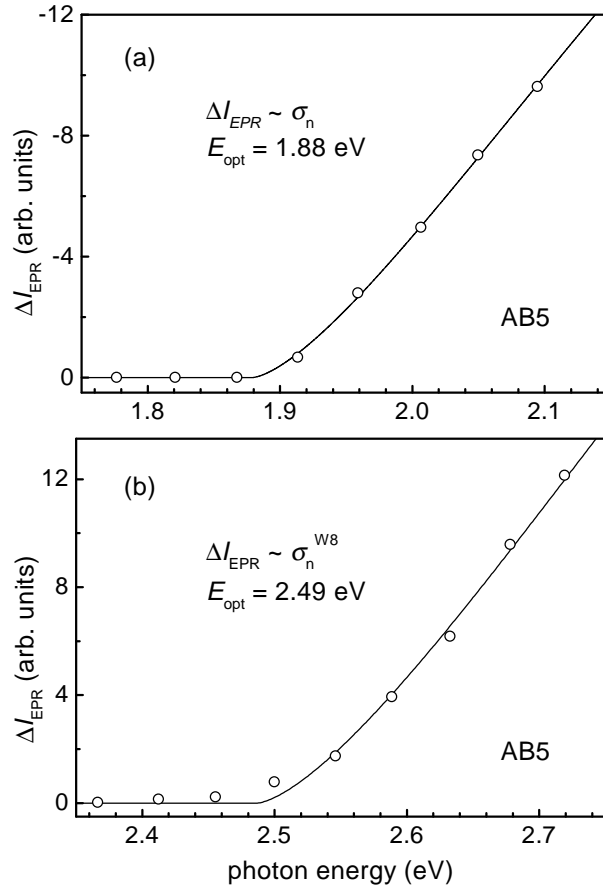


**Figure 6.11:** (a) Dependence of the quenching of the EPR signal versus the photon energy for the AB5 center. (b) Spectral dependence of the recovery of the AB5 EPR signal previously quenched by illumination with  $h\nu = 2.23$  eV. In this case,  $\Delta I_{EPR}$  is measured relative to the minimum signal intensity achieved after a prolonged illumination. The circles represent experimental values and the full curves are fits to the data by Equation (2.84).

namely, that from the impurity level to the CB or that from the VB to the impurity level, with optical cross sections  $\sigma_n^{AB5}$  and  $\sigma_p^{AB5}$ , respectively. Under the assumption of only one dominant transition and excluding photoionization of other defect levels, the kinetics of the AB5 photoionization can be linked to the light intensity either through  $\alpha_n^{AB5} = I\sigma_n^{AB5}$  or through  $\alpha_p^{AB5} = I\sigma_p^{AB5}$ . The data shown in Figure 6.11(a) were obtained under the condition of a linear relation between  $\Delta I_{EPR}$  and the corresponding  $\alpha^{AB5}$  value. Fitting the spectral dependence of these experimental data by Equation (2.84), we obtained for the AB5 center

the ionization energy  $E_{\text{opt}} = 1.88 \pm 0.03$  eV, with  $\Gamma = 0$  eV. Since the detected photoquenching can be caused by the electron or hole ionization, the locations of the level below the CB or above the VB are indistinguishable. In order to verify the nature of this transition, we suppressed the AB5 signal intensity by photoexcitation with the photon energy  $\approx 2.3$  eV to its minimum value and monitored the changes in the signal intensity upon illumination with photon energies  $h\nu > 2.3$  eV. We found that the signal intensity increases upon illumination with  $h\nu > 2.5$  eV. Fitting, for each photoexcitation, the time-dependence of this increase by exponential decay functions, we determined the spectral dependence of  $\Delta I_{\text{EPR}}$ , see Figure 6.11(b). The optical cross section may be considered to be linearly proportional to the  $\Delta I_{\text{EPR}}$  values of the AB5 recharging process. The increase of the AB5 signal intensity can be explained by an indirect process similar to the previously described recharging of nitrogen, i.e., electrons photoexcited from the nickel center are subsequently captured by the AB5 defect. In general, this process depends on both the optical cross sections  $\sigma_{\text{n}}^{\text{AB5}}$  and  $\sigma_{\text{n}}^{\text{W8}}$ . As a matter of fact, the photo-EPR data on the AB5 center show that the cross section cannot be neglected. Thus, at energies higher than 2.5 eV we have to consider both the transitions, namely from W8 to CB and from AB5 to CB. However, it is evident from the EPR spectra that the concentration of the substitutional nickel in the investigated samples is always much higher than that of the AB5 defects. For this reason, the photoelectrons produced by the illumination with photon energies  $h\nu > 2.5$  eV are mainly created through the ionization of the W8 centers. The best fit of the spectral dependence of  $\Delta I_{\text{EPR}}$  by Equation (2.84) is obtained for  $E_{\text{opt}} = 2.49 \pm 0.04$  eV, in excellent agreement with the value measured from the direct ionization of the  $\text{Ni}_{\text{s}}^{-/0}$  acceptor level. Again, the Lucovsky formula for the purely electronic optical cross section was considered in the calculation. The observation of such indirect recharging of AB5 together with the localization of the  $\text{Ni}_{\text{s}}^{-/0}$  level at  $E = E_{\text{c}} - 2.49$  eV provide a direct proof that the photoionization process detected on the AB5 center at 1.88 eV involves the promotion of electrons to the conduction band. Therefore, the recharging level of the AB5 defect is located at  $E = E_{\text{c}} - 1.88$  eV.

### 6.6.2 CENTER AB4

As we concluded in Chapter 4, the EPR spectrum of the AB4 center is detected in HPHT diamonds that suffered a post-growth heat treatment. Our EPR measurements upon irradiation with visible light revealed that the AB4 signal strongly increases in intensity. Samples

used in the studies of the photoexcitation behavior of the AB4 centers were annealed synthetic HPHT diamonds similar to samples F and G of Table 3.1. EPR spectra of the samples exhibited also the presence of the centers P1, W8, AB1-AB6, and NE1-NE3. From infrared absorption spectroscopy we estimate the concentrations of substitutional  $N_s^0$ ,  $N_s^+$ , and  $A$  aggregates as being typically 80 ppm, 25 ppm, and 250 ppm, respectively.

In order to monitor the kinetics and the wavelength dependence of this photoinduced effect, we fixed the external magnetic field  $\mathbf{B}$  at the position of maximum intensity of the first derivative of one of the AB4 EPR lines and monitored the time-dependence of the EPR signal intensity ( $I_{\text{EPR}}$ ) upon monochromatic illumination. In order to avoid an erroneous evaluation of the photoinduced changes by monitoring overlapping EPR lines from different centers, we chose the well isolated lower magnetic field AB4 line for  $\mathbf{B} \parallel [011]$  shown in the spectrum of Figure 4.12. The photoinduced changes produced in the AB4 signal intensity for excitation photon quanta  $h\nu = 2.01, 2.05, 2.09,$  and  $2.14$  eV are shown in Figure 6.12. For a sequence of increasing photoexcitation energies  $h\nu$ , the difference  $\Delta I_{\text{EPR}}$  between the photoinduced EPR signal intensity and the  $I_{\text{EPR}}$  measured prior to illumination was estimated through fitting the  $I_{\text{EPR}}$  vs. time data with exponential decay functions, see Figure 6.12. The spectral dependence of  $\Delta I_{\text{EPR}}$  determined from this fitting is presented in Figure 6.13. The observed enhancement of the AB4 EPR signal intensity is interpreted as a result of a photoionization process occurring at a defect with localized states in diamond. In the case of the AB4 excitation we assume that the enhancement of its EPR signal intensity results from one dominant photoionization process. This assumption is highly motivated in this case, since the increase of the AB4 signal intensity with time has a single exponential variation. Considering, besides, that the data shown in Figure 6.13 were obtained under the experimental conditions of a linear dependence between  $\Delta I_{\text{EPR}}$  and  $\alpha$ , described above, the optical cross section of the involved photoionization is linearly related to  $\Delta I_{\text{EPR}}$ . Fitting the spectral dependence  $\sigma(h\nu)$  of the AB4 photoexcitation by Equation (2.84), with  $\sigma_{\text{el}}$  substituted by the Lucovsky formula, we find an ionization energy  $E_{\text{opt}} = 2.06 \pm 0.02$  eV and  $\Gamma = 0$  eV.

The observed enhancement of the AB4 signal intensity can be caused by two types of processes: (i) a direct electron (hole) excitation from the AB4 centers to the conduction (valence) band or (ii) an indirect process if electrons (holes) excited to the conduction (valence) band from another defect are then captured by the AB4 centers. The unambiguous determination

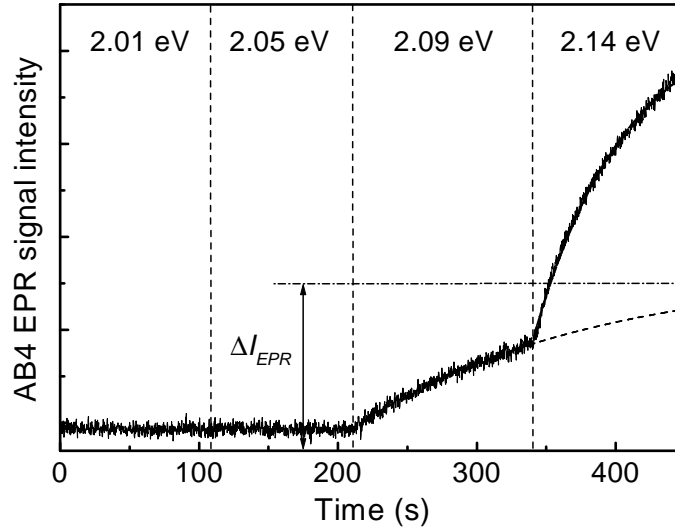


**Figure 6.12:** Time-dependence of the EPR signal intensity  $\Delta I_{EPR}$  of the AB4 center at  $T = 100$  K for different excitation energies  $h\nu$ . Full curves represent experimental data and dashed curves are exponential fits.

of the process that governs the photoinduced increase of the AB4 EPR signal intensity is hindered by the fact that this spectrum could only be detected in one type of the available set of samples. However, the appearance of a strong photoinduced effect with a threshold at 2.06 eV only for the AB4 lines, together with the observation of different spectral dependencies for the photoinduced changes of other centers present in the same samples, indicate that a direct photoionization is the most probable process to explain the observed behavior of the AB4 center under illumination. Whether the increase of the AB4 signal is resulting from a direct (i) or an indirect (ii) process, it can occur either by electron or by hole ionization. The observation of the nitrogen donor signal (P1) prior to any illumination of the samples indicates that the Fermi level is located at or above the  $N^{0/+}$  level. The position of this defect level in the diamond gap have been taken as  $E = E_c - 1.7$  eV (Walker, 1979). Therefore, the observed transition with the threshold at 2.06 eV is interpreted as promotion of electrons to the conduction band.

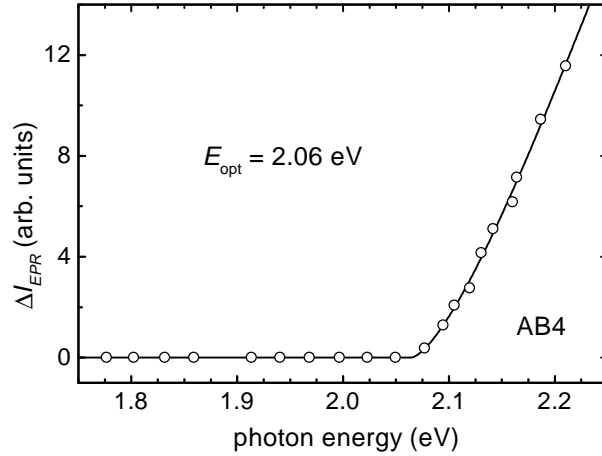


**Figure 6.13:** Spectral dependence of the AB4 EPR signal photoenhancement. The measurement temperature is 100 K. The circles represent experimental data and the solid curve is a fit of the data by Equation (2.84).

### 6.6.3 CENTER AB2

Like the AB4 center, the AB2 paramagnetic defect is observed in HPHT diamonds grown from a pure nickel solvent, which were posteriorly annealed at 1600 °C. This center has trigonal symmetry and spin  $S = \frac{1}{2}$  with  $g$ -values evidencing the presence of nickel (see Chapter 4). Carrying out EPR measurements on synthetic diamonds which have shown the presence of AB2 centers (the same samples as those used to study the AB4 photoexcitation), we observed a strong decrease of the AB2 spectrum upon illumination. Figure 6.14 shows the spectral dependence of the quenching of the AB2 spectrum obtained in the same way as described in Subsection 6.2.3. The open circles are experimental data and the solid line represents the best fit of Equation (2.84) to these data. Taking  $\sigma_{el}$  as given by the Lucovsky formula, the fitting procedure leads to  $E_{opt} = 1.67 \pm 0.03 \text{ eV}$  and  $\Gamma = 0.03 \pm 0.03 \text{ eV}$ . Among the paramagnetic centers detected in the same samples, only the AB2 center shows an optically induced effect with this spectral dependence. The ionization of the AB5 centers was observed for  $h\nu \geq 1.88 \text{ eV}$ , whereas the AB3 and AB4 spectra evidenced photoinduced intensity changes for photon energies  $h\nu$  higher than 2.26 eV (see the following subsection) and 2.06 eV, respectively. The AB3 spectrum intensity shows a decrease, whereas the AB4

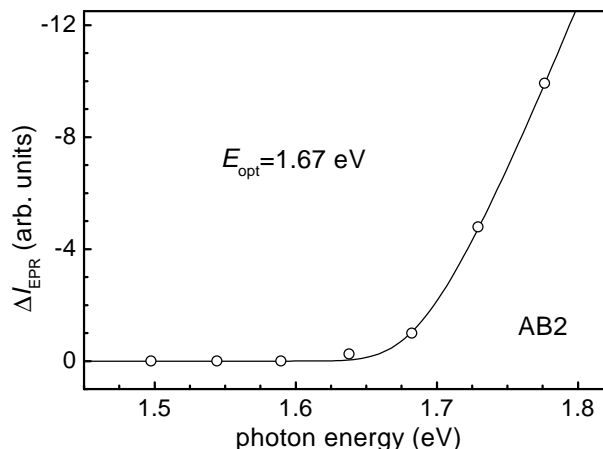


**Figure 6.14:** Spectral dependence of the photoinduced changes in the intensity of the AB2 center spectrum, normalized to a constant photon flux. Experimental data are represented by open circles and the solid line results from fitting the experimental data with Equation (2.84).

EPR signal intensity increases upon illumination.

Due to the fact that only the AB2 spectrum exhibits a strong photoinduced effect setting in at 1.67 eV, in samples showing the presence of a large variety of paramagnetic defects, we infer that the observed photoexcitation should result from direct ionization of the AB2 centers. Similarly to the AB4 EPR signal photoexcitation, the 1.67 eV threshold should correspond to electron ionization, since the Fermi level in these samples is located above 1.7 eV.

#### 6.6.4 CENTER AB3

The intensity of the AB3 EPR lines in some of the used crystals decreases upon sample illumination with visible light. The time-dependence of this process was recorded for different excitation wavelengths and the  $\Delta I_{\text{EPR}}$  values were determined as described above for the other studied centers. The normalized spectral dependence of  $\Delta I_{\text{EPR}}$  obtained is presented in Figure 6.15. A photon energy threshold of about 2.3 eV was determined for the observed decrease of the signal intensity. Provided that only one dominant photoionization process is responsible for the decrease of the AB3 EPR signal intensity and taking into account that

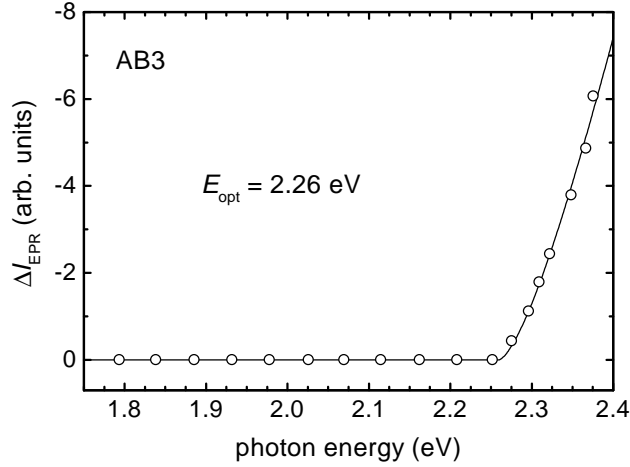


**Figure 6.15:** Spectral dependence of the AB3 EPR signal photoquenching. The circles represent experimental data and the solid curve is a fit of the data by Equation (2.84).

the experimental data shown in Figure 6.15 were obtained under the conditions of linear dependence between  $\Delta I_{\text{EPR}}$  and  $\alpha$ , the optical cross section of the photoionization is linearly related to  $\Delta I_{\text{EPR}}$ . The best fit of Equation (2.84) to the curve shown in Figure 6.15 is obtained for  $E_{\text{opt}} = 2.26 \pm 0.02$  eV and a zero  $\Gamma$  value.

No relevant changes were observed in the AB1 and AB6 signal intensities. Furthermore, we failed to detect any signal from the NE6 and NE7 spectra upon illumination. Both defects are reported by Nadolinny *et al.* (1997) as being produced upon excitation with photon energies  $h\nu$  higher than  $\sim 3.4$  eV.

The photoinduced effect described for the AB3 center was only observed in annealed samples (the same samples used to study the photoexcitation of the AB2 and AB4 centers), whereas in as-grown diamonds that exhibit the AB3 spectrum a sensitive change of the AB3 EPR signal intensity upon illumination was not detected. We see two possible explanations for this behavior of the AB3 center: (a) the decrease of the signal intensity results from the capture, from the conduction (valence) band, of electrons (holes) that were excited from another defect produced during the annealing process and located at 2.26 eV in the diamond gap; or (b) the direct photoionization of AB3 centers is observed and the photoexcitation effect in the as-grown samples is undetectable due to the small amount of acceptor (donor)

levels available to capture the photoexcited electrons (holes). From Equation (6.8), we see that the photoexcitation is enhanced for increasing values of  $(N_R - n_R^0)$  and  $N_A$ . Alike in the AB4 photoexcitation mechanism, the photoionization transition that leads to the changes in the AB3 signal intensity should involve the promotion of electrons to the conduction band, independent of which process (a) or (b) occurs.

### 6.6.5 DISCUSSION

It is quite unlikely that the distinct photoexcitation thresholds detected in the AB2-AB5 centers correspond to indirect mechanisms other than photoionization of these centers. Moreover, we do not expect that through an indirect process a capture center would have a strong dependence of the photoexcitation on the light intensity, like that observed for the AB2-AB3 centers. For the kinetic model presented in Section 6.3, we see that the expression derived for the photoexcitation  $\Delta n_A$  of pure capture centers A is independent of the light intensity, see Equation (6.9).

The AB3 and AB4 EPR signals, both with orthorhombic-I symmetry and no hyperfine structure, may in principle correspond to the same defect in different charge states. In such a case we should observe a complementary behavior of their EPR signal intensities upon photoionization, i.e., an increase of the AB4 center concentration due to photoionization at  $h\nu > 2.06$  eV would be accompanied by a corresponding decrease of the AB3 spectrum. Even though the EPR spectra of the used samples evidenced a dark concentration of AB4 centers approximately three times higher than the amount of AB3 defects we failed to observe such a complementary behavior of their EPR spectra upon illumination. Thus, the AB3 and AB4 spectra must belong to different defects.

According to the Ludwig-Woodbury model, the most likely structure for the AB5 defect consistent with the observed spin state  $S = 1$  is a substitutional  $\text{Ni}^{2-}$  ion, with the trigonal symmetry caused by a Jahn-Teller distortion or a nearest neighbor impurity, e.g., nitrogen (see Subsection 4.3.3). In the case of a Jahn-Teller effect the W8 and AB5 spectra might correspond to the same defect in different charge states. In this situation, through the photoionization of the AB5 centers for  $h\nu > 1.88$  eV, we should observe as well an increase of the EPR signal of the W8 center. This effect was not observed in our photo-EPR measurements, even in the samples which show a significant concentration of AB5 centers. Thus, we may

**Table 6.1:** Huang-Rhys factors  $S$  for some nickel-related optical centers obtained from electron-vibrational spectra.

Feature (eV)	Huang-Rhys factor $S$	Dominant phonon (meV)	Reference
1.40	1.6	60	Davies (1977 <i>b</i> )
1.693	1.3	28	Neves <i>et al.</i> (1999 <i>a</i> )
1.883	0.7	61	Nazaré and Rino (1993)
2.51	$\sim 0.25$	16.5	Nazaré <i>et al.</i> (2001)

rule out the hypothesis that the structure of the AB5 center is a single substitutional Ni<sup>2-</sup> ion.

It is interesting to note that all the ionization transitions observed in our photo-EPR measurements exhibit a sharp spectral onset of the photoexcitation. This is evidenced by a vanishing broadening parameter  $\Gamma$ , resulting from the fitting procedure. Thus, a small relaxation energy  $E_{\text{rel}}$  appears to be a common characteristic of the nickel-containing defects in diamond. On the contrary, substitutional nitrogen N<sub>s</sub><sup>0</sup> exhibits a rather strong relaxation upon ionization,  $E_{\text{rel}} \approx 0.5$  eV (Walker, 1979; Rosa *et al.*, 1999). This relative large relaxation energy seems to be related with the trigonal distortion which results from the population of an antibonding orbital in one of the N-C bonds by the nitrogen's fifth valence electron (Breuer and Briddon, 1996). Small values of  $E_{\text{rel}}$  are indicative of a relatively weak electron-lattice coupling of nickel defects in diamond. Huang-Rhys factors  $S$ , obtained from vibronic spectra of nickel-related optical centers, also reveal a modest electron-phonon coupling. Table 6.1 shows the factors  $S$  and corresponding dominant phonon energies for some nickel-related optical features. This is possibly a result of the high localization of the defect wavefunctions on the impurity. Moreover, the spin-orbit coupling, shown to be relatively strong in Ni defects (as derived from the deviations of the  $g$ -values from  $g_e$ ), may play a predominant role in the stabilization of the defects, as compared to distortions produced by terms of interaction between the electrons and the lattice vibrations.

## 6.7 THE ROLE OF N IN THE PHOTOIONIZATION KINETICS

Nitrogen, being a deep donor (and in the neutral charge state giving rise to the P1 EPR center), acts as a charge compensator for other defects with acceptor levels lying more deeply in the gap, like substitutional  $\text{Ni}^-$  (W8 EPR center). In diamonds with an excess of nitrogen (with  $[\text{N}_s]=N_N$ ), the latter is found to coexist in thermal equilibrium in both the neutral and the positive charge states, with concentrations  $n_N$  and  $N_N - n_N$ , respectively. Even in synthetic diamonds grown with the addition of a nitrogen getter to the metal solvent, nitrogen is found to be the most abundant impurity. In such a case the Fermi energy should be near to  $E_F = E_c - 1.7$  eV. This is probably the reason why most of the photoionization processes observed in our photo-EPR measurements have energy thresholds  $E_{\text{opt}} \gtrsim 1.7$  eV. In this type of samples nitrogen should be as well the main charge transfer path during photoionization of other defects. Such direct intercenter recharging processes were observed to be quite efficient in deep defects in silicon (Frens *et al.*, 1994) and, consequently, must be considered in the analysis of ionization experiments. In the case of deep centers, this mechanism occurs by tunnelling and presupposes a non-vanishing overlap between the two defect wavefunctions. In our case, this means a spatial correlation between substitutional N and Ni-related defects. The formation of nickel-nitrogen complexes in HPHT diamonds evidences the probability of such a correlation (Nadolinny *et al.*, 1999). The intercenter charge transfer mechanism is responsible for some recovery of the EPR signals after switching off the illumination. Though this recovery was in some cases very small, it was always observed, proving the participation of these recharging processes.

Under these conditions the changes produced by the illumination on the population of the photoinduced charge state of a given center X ( $\Delta n_X$ ) have the form given by Equation (6.8). If the charge transfer efficiency  $\beta_{\text{NX}}$  between nitrogen and the defect X is not extremely low,  $\Delta n_X$  has a linear dependence on the absorption coefficient  $\alpha_n^X$ , for  $\alpha_n^X < 2\beta_{\text{NX}}$ :

$$\Delta n_X \simeq -\frac{N_X}{(n_N^0 - \lambda)\beta_{\text{NX}}}\alpha_n^X \quad (6.11)$$

with

$$\lambda = \frac{C_n^A}{C_n^N}N_A .$$

Here,  $n_N^0$  is the dark concentration of P1 centers and  $C_n^N$  is the capture rate of electrons by  $\text{N}^+$ . For high  $\alpha_n^X$  values,  $\Delta n_X$  does not depend anymore on  $\alpha_n^X$ , i.e.,  $\Delta I_{\text{EPR}}$  saturates as

observed in our photo-EPR measurements,

$$\Delta n_X \simeq -\frac{N_X}{\Lambda} \quad (6.12)$$

with

$$\Lambda = 1 + \frac{C_n^X N_X}{C_n^N (N_N - n_N^0) + C_n^A N_A}.$$

In the case of the AB2-AB5 and NIRIM1 centers, the approximation of negligible photoionization of the recharging centers (see Section 6.3) is highly motivated as the  $N^0$  defects are optically ionized only for  $h\nu > 2.2$  eV (Rosa *et al.*, 1999). The linear dependence on  $\Delta n_X$  is only observed in the case of a non-zero dark concentration of recharging centers. In diamond, this is reflected by the observation of the P1 defects before illumination, i.e, not all substitutional nitrogen centers participate in the charge compensation process. This is generally true in N containing diamonds where nitrogen is not fully compensated, e.g., through the addition of boron. This model justifies the observed linear dependence of  $\Delta I_{\text{EPR}}$  on the photoionization optical cross section of Ni-containing defects.

## 6.8 SUMMARY

We have investigated the photoinduced effects produced on paramagnetic defects involving nickel and nitrogen atoms. The experimental method used to measure photo-EPR was discussed. A theoretical description of the photoionization kinetics is proposed to explain the dependence of the photoexcitation on the optical cross section of the transitions induced during a photo-EPR experiment.

A photoinduced quenching of the substitutional  $\text{Ni}_s^-$  EPR signal was observed for photoexcitation energies  $h\nu$  higher than  $\sim 2.5$  eV, in accordance to Hofmann *et al.* (1994). An enhancement of the W8 EPR signal is also observed for photon energies  $h\nu > 3.0$  eV. Indirect photoinduced recharging of the nitrogen donor defect P1 and detection of two complementary photoionization transitions involving the substitutional nickel indicated that the  $\text{Ni}_s^{-/0}$  acceptor level should be located at  $2.49 \pm 0.03$  eV below the minimum of the conduction band. The analysis of the temperature dependence of the W8 spectrum photoquenching showed that the relaxation energy of the substitutional nickel defect upon ionization of the

negative charge state should be less than  $\sim 0.02$  eV. This result corroborates the hypothesis that the observed photoinduced effects, with thresholds at 2.5 eV and 3.0 eV, correspond to two complementary photoionization transitions involving substitutional  $\text{Ni}_s^-$  in diamond. This observations prove that the  $\text{Ni}_s^{-/0}$  level is located at  $E_c - 2.49$  eV.

Photoinduced changes produced in the NIRIM1 EPR spectrum, tentatively assigned to interstitial  $\text{Ni}_i^+$ , suggest that the  $\text{Ni}_i^{0/+}$  defect level is located at  $1.98 \pm 0.03$  eV below the conduction band. In nitrogen-doped diamond, interstitial nickel is shown to be more likely to appear in the neutral charge state, which is undetectable by EPR, whereas the nickel impurity in the substitutional site is introduced in the negative charge state  $\text{N}^-$ , which is revealed by EPR.

The photoexcitation properties of some of the AB paramagnetic defects were also investigated. A strong decrease of the AB5 EPR signal intensity is produced by irradiation of the samples with photon energies  $h\nu > 1.88$  eV. This photoinduced effect is sample independent. Observation of a recharging process upon photoexcitation with  $h\nu > 1.88$  eV yields the localization of the AB5 defect level position at  $E_c - 1.88$  eV.

We observed a strong increase of the AB4 EPR signal intensity when diamond samples were illuminated with monochromatic light with photon energies  $h\nu > 2.06 \pm 0.02$  eV, and a strong decrease of the AB2 EPR spectrum intensity upon illumination with  $h\nu > 1.67 \pm 0.03$  eV. Additionally, a quenching of the AB3 signal intensity was observed for photoexcitations at  $h\nu > 2.26 \pm 0.02$  eV. The observation of photoinduced changes of the AB2, AB3, and AB4 centers having different spectral dependencies, yielded the proposal that the observed effects correspond to direct ionization of these paramagnetic defects. The fact that the concentration of nitrogen deep donors in the used samples is quite high, indicates that the observed transitions involve the promotion of electrons to the conduction band. In such a case, the energy defect levels of the AB2, AB3, and AB4 are located at 1.67 eV, 2.23 eV, and 2.06 eV below the conduction band.

Photo-EPR data show that the AB3 and AB4 rhombic-I centers cannot be different charge states of the same center and rule out the single substitutional  $\text{Ni}^{2-}$  model for the AB5 center. A weak lattice relaxation upon ionization associated with a low electron-phonon coupling seems to be a common characteristic of nickel-containing defects in diamond.

It is presented a theoretical model describing the kinetics of the photoexcitation processes occurring on nickel defects in nitrogen containing diamond, which assumes direct recharging

through substitutional nitrogen centers.

# CONCLUDING REMARKS

Owing to the use of the nickel catalyst in the synthesis of high quality diamond at high pressure and high temperature, the understanding of the behavior of nickel related defects in this material is an essential goal of investigators engaged in the diamond research. Some of the prominent issues are, for instance, the structure and amount of the nickel-related defects formed in as-grown HPHT diamond and their dependence on the particular growth method; the interactions between nickel and other centers like nitrogen and intrinsic defects; the role of nickel in the aggregation mechanism of nitrogen during high temperature annealing; and the influence of nickel on the optical properties of HPHT diamond.

In this thesis, diamonds grown at HPHT with nickel-containing solvent / catalysts were investigated. The work concerned with the study of point defects related with impurities incorporated in such type of crystals during their synthesis. The experiments were grounded on the electron paramagnetic resonance technique (EPR) in the usual configuration and also associated with optical excitation (photo-EPR). The formation conditions of paramagnetic centers in HPHT diamond and the interactions between impurities during high temperature annealing were investigated by carrying out an annealing work on HPHT crystals.

The analysis of the complex anisotropic structure of the EPR spectra of HPHT diamonds grown at distinct conditions and annealed after growth at different temperatures revealed the existence of several unreported paramagnetic centers, which we labeled AB1 to AB7. These defects have different characteristics regarding, the local symmetry, spin, and type of crystals where they occur. Furthermore, their spectroscopic properties strongly suggest that they are all related with the introduction of the nickel impurity in diamond.

The AB1 center is shown to have trigonal symmetry and electron spin  $S = 1/2$ . This paramagnetic defect is detected in as-grown crystals which incorporated large amounts of both nitrogen and nickel during the HPHT synthesis. Its concentration is increased upon annealing at temperatures approximately in the interval  $1600^\circ \lesssim T_a \lesssim 1900^\circ$ , and anneals

out after heat treatments at higher temperatures. It is proposed that the AB1 defect is the most probable paramagnetic charge state of the trigonal defect which is believed to be the common fragment of the NE1-NE3, NE5, and RM1/NE8 nickel-nitrogen complexes. This proposal contradicts the original and accepted model, where such basic trigonal structure is assumed to be the NE4 paramagnetic center (Nadolinny *et al.*, 1999). However, further studies must be carried out to attain an unambiguous determination of the precursor of the NE centers in diamond.

Along with the AB1 center, the AB3 paramagnetic defect is also present in as-grown crystals containing high amounts of nitrogen and nickel impurities. This point defect reveals an orthorhombic-I symmetry with spin  $S = 1/2$ . Like the AB1 defect, the AB3 center concentration increases through heat treatments at intermediate temperatures and decreases behind the detection limit upon annealing at very high temperatures. The photoinduced effects observed on the AB3 EPR spectra seem to indicate that this center has a deep level in the gap of diamond located at  $E_c - 2.06$  eV.

Among the paramagnetic defects described in this work, the AB5 center is the only one that is not a spin-half defect. Its electron spin is found to be  $S = 1$  and the anisotropic properties of the corresponding EPR lines shows unambiguously a trigonal pattern. This defect has been detected in all as-grown diamonds which are synthesized from nickel-containing solvent / catalysts without the addition of nitrogen getters. The concentration of AB5 centers is gradually decreased when samples are subjected to high temperature annealings at increasing temperatures, until it anneals out at temperatures as high as 2000°C. It is also found that the AB5 defect level position is situated in the gap at 1.88 eV below the conduction bottom. A model of a nearest-neighbor pair of substitutional nickel and nitrogen atoms in the negative charge state  $(\text{Ni}_s\text{-N}_s)^-$  was putted forward for this center. According to the Ludwig-Woodbury theory, the nickel ion assumes in such structure the electronic configuration  $3d^8$  for an electron spin  $S = 1$ .

The AB6  $S=1/2$  defect corresponds to a nearly monoclinic-I system that undergoes a small distortion to triclinic symmetry. This is a transitory defect, since it is solely detected in annealed HPHT crystals (at temperatures  $T_a > 1600^\circ\text{C}$ ) and is suppressed upon heating the samples at temperatures higher than 1900°.

Also the AB2 and AB4 centers are detected exclusively in diamond crystals that suffered heat treatments ( $T_a \approx 1600^\circ\text{C}$ ). However, they could not be produced in detectable amounts

in the annealing study which was carried out. The AB2 defect is trigonal, whereas the AB4 is an orthorhombic-I center, both having spin  $S = 1/2$ . The photoinduced transitions related with the ionization of the AB2 and AB4 centers were found with photon energy thresholds of 1.67 eV and 2.06 eV. These transitions are probably related with the promotion of electrons to the conduction band.

The AB7 paramagnetic center is produced upon annealing at temperatures  $T_a > 1600^\circ\text{C}$  of low nitrogen HPHT samples. This  $S = 1/2$  paramagnetic defect reveals an orthorhombic-I symmetry. Using the ligand field approach, we observe that the measured  $g$ -values are consistent with a transition metal ion with  $3d^5$  electronic configuration in a strong-bonded octahedral environment that is distorted to orthorhombic-I symmetry.

A detailed investigation of the photoexcitation properties of the dominant nickel-related defect in diamond (substitutional  $\text{Ni}_s^-$ ) was carried out. It is clearly shown that this defect induces the level  $\text{Ni}_s^{-/0}$  in the energy gap of diamond. Such level is found to be located at 2.49 eV below the conduction band minimum.

The photoexcitation properties of the NIRIM1 spin-half center, ascribed to positively charged nickel  $\text{Ni}_i^+$  (Isoya *et al.*, 1990b), were investigated. The detected photoinduced changes suggest that the  $\text{Ni}_i^{0/+}$  level is located at 1.98 eV below the conduction band.

A theoretical model describing the defect-related excitation and capture processes which occur during a photoionization experiment was put on view. This approach may be generally used in the interpretation of photo-EPR transients in the framework of the saturation method proposed by Godlewski (1985). Here, the model was consistently applied in the explanation of the photoexcitation behavior of the nickel-related defects in diamond, by assuming direct recharging through substitutional nitrogen defects.

It is hoped that the information provided by the present work stem further exploitations of defects in diamond, and ultimately will be useful for the understanding of the role of transition metals in diamond.

For a more definitive determination of the structure of the AB centers, it is required information regarding their carbon environment. One possibility is the study of synthetic crystals isotopically enriched with a small amount of  $^{13}\text{C}$  ( $I = 1/2$ , natural abundance 1.1%). Any superhyperfine structure related with the  $^{13}\text{C}$  isotope, revealed as symmetrically positioned lines on either side of a given EPR line, would give important information about the structure

of the defects.

Small hyperfine parameters may result in a structure which is hidden within the linewidth of an EPR line. In such a case, the hyperfine interaction may be resolved by means of electron-nuclear double resonance (ENDOR) experiments. For example, ENDOR measurements on the AB1 and AB5 paramagnetic defects may give the ultimate proof about their proposed structures.

# APPENDIX A

## LORENTZIAN FUNCTION

An important lineshape which is commonly observed in EPR experiments is that of the Lorentzian function. The analytical expression of this function reads,

$$Y(x - x_0) = \frac{A}{\pi} \frac{\Gamma}{\Gamma^2 + (x - x_0)^2}, \quad (\text{A.1})$$

where  $A$  is the area under the absorption peak, which corresponds to the intensity of the EPR line  $I_{\text{EPR}}$ . A normalized Lorentzian function corresponds to a line with unitary area  $A$ . The half-width at half-height is given by  $\Gamma$ . Usually an EPR line have the shape of the Lorentzian function first-derivative,

$$Y'(x - x_0) = -\frac{A}{\pi} \frac{2\Gamma(x - x_0)}{[\Gamma^2 + (x - x_0)^2]^2}, \quad (\text{A.2})$$

like that shown in Figure A.1. Important quantities that are normally measured at this type of line are the peak-to-peak amplitude  $A_{\text{pp}}$  and the peak-to-peak width  $\Delta x_{\text{pp}}$ . These are related to  $A$  and  $\Gamma$  in the following way:

$$A_{\text{pp}} = \frac{3\sqrt{3}}{4\pi} \frac{A}{\Gamma^2} \quad (\text{A.3})$$

$$\Delta x_{\text{pp}} = \frac{2}{\sqrt{3}} \Gamma \quad (\text{A.4})$$

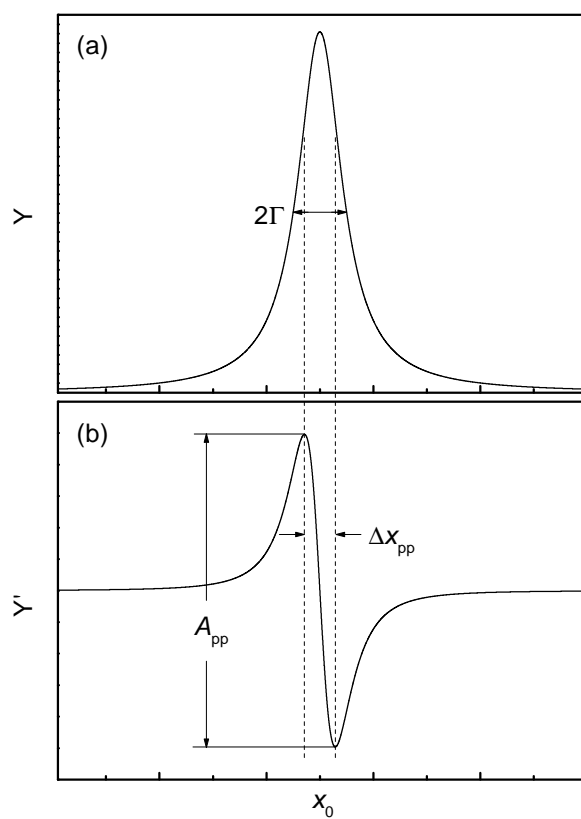


**Figure A.1:** Lorentzian lineshapes: (a) absorption spectrum; (b) first-derivative lineshape.

# BIBLIOGRAPHY

- Abragam A and Bleaney B, *Paramagnetic Resonance of Transition Metal Ions* (Oxford University Press, Oxford, United Kingdom, 1970).
- Amato M A, J. Phys. C: Solid St. Phys. **13**, 2027 (1980).
- Ammerlaan C A J, in *Landolt-Börnstein - Numerical Data and Functional Relationships in Science and Technology, New Series, Group III, vol. 22b*, (edited by O Madelung and M Shulz), pp. 117–206 (Springer-Verlag, Berlin, Germany, 1990).
- Atherton N M, Davies M J, and Gilbert B C, *Electron Spin Resonance : a Review of Recent Literature to 1993* (The Royal Society of Chemistry, Cambridge, United Kingdom, 1994).
- Bachelet G B, Baraff G A, and Schulüter M, Phys. Rev. B **24**, 4736 (1981).
- Bagdasaryan V S, Markosyan E A, Matosyan M A, Torosyan O S, and Sharoyan E G, Fiz. Tverd. Tela **17**, 1518, [Soviet Phys. Solid State **17**, 991 (1975)] (1975).
- Baker J M, J. Phys.: Condens. Matter **13**, 2043 (2001).
- Baker J M and Newton M E, Appl. Magn. Reson. **7**, 209 (1994).
- Bebb H B and Chapman R A, J. Phys. Chem. Solids **28**, 2087 (1967).
- Bharuth-Ram K, Hartick M, Kankeleit E, Dorn C, Held P, Sielemann R, Wende L, Kübler J, and Sellschop J P F, Phys. Rev. B **58**, 8955 (1998).
- Bloch F, Phys. Rev. **70**, 460 (1946).
- Born M, *Atomic Physics* (Dover Publications, Inc., New York, USA, 1989).
- Bourgoin J and Lannoo M, *Point Defects in Semiconductors II: Experimental Aspects* (Springer-Verlag, Berlin, Germany, 1981).
- Boyd S R, Kiflawi I, and Woods G S, Philos. Mag. B **69**, 1149 (1994).

- Boyd S R, Kiflawi I, and Woods G S, *Philos. Mag. B* **72**, 351 (1995).
- Breuer S J and Briddon P R, *Phys. Rev. B* **53**, 7819 (1996).
- Bruch M D, *NMR Spectroscopy Techniques* (Marcel Dekker, New York, USA, 1996).
- Burns R C, Cvetkovic V, Dodge C N, Evans D J F, Rooney M L T, Spear P M, and Welbourn C M, *J. Crystal Growth* **104**, 257 (1990).
- Burns R C and Davies G J, in *The Properties of Natural and Synthetic Diamond*, (edited by J E Field), pp. 396–422 (Academic Press, London, 1993).
- Butler J E and Goodwin D G, in *Properties, Growth and Applications of Diamond*, (edited by M H Nazaré and A J Neves), 26, pp. 262–263 (INSPEC, The Institution of Electrical Engineers, London, United Kingdom, 2001).
- Charnock F and Kennedy T A, *Phys. Rev. B* **64**, 041201 (2001).
- Chevallier J, in *Properties, Growth and Applications of Diamond*, (edited by M H Nazaré and A J Neves), 26, pp. 236–242 (INSPEC, The Institution of Electrical Engineers, London, United Kingdom, 2001).
- Chevallier J, Lusson A, Ballutaud D, Theys B, Jomard F, Deneuille A, Bernard M, Gheeraert E, and Bustarret E, *Diamond Relat. Mater.* **10**, 399 (2001).
- Chrenko R M, *Phys. Rev. B* **7**, 4560 (1973).
- Chrenko R M, Strong H M, and Tuft R E, *Phil. Mag.* **23**, 313 (1971).
- Chrenko R M, Tuft R E, and Strong H M, *Nature* **270**, 141 (1977).
- Clark C D, Dean P J, and Harris P V, *Proc. R. Soc. A* **277**, 312 (1964).
- Clark C D, Ditchburn R W, and Dyer H B, *Proc. R. Soc. A* **234**, 363 (1956).
- Clark C D, Kanda H, Kiflawi I, and Sittas G, *Phys. Rev. B* **51**, 1668116688 (1995).
- Clark D D, Collins A T, and Woods G S, in *The Properties of Natural and Synthetic Diamond*, (edited by J E Field), pp. 35–79 (Academic Press, London, United Kingdom, 1993).
- Collins A T, *J. Phys. C: Solid State Phys.* **13**, 2641 (1980).

- Collins A T, Kanda H, and Burns R C, *Philos. Mag. B* **61**, 797 (1990).
- Collins A T and Spear P M, *J. Phys. D* **15**, L183 (1982).
- Collins A T and Williams W S, *J. Phys. C: Solid State Phys.* **4**, 1789 (1970).
- Cox A, Newton M E, and Baker J M, *J. Phys.: Condens. Matter* **6**, 551 (1994).
- Davies G, *J. Phys. C: Solid St. Phys.* **9**, L537 (1976).
- Davies G, *Nature* **269**, 498 (1977*a*).
- Davies G, in *Chemistry and Physics of Carbon*, (edited by P W Philips and P A Turner), volume 13, pp. 1–143 (Marcel Dekker, New York, USA, 1977*b*).
- Davies G, *Physica B* **273-274**, 15 (1999).
- Davies G, in *Properties, Growth and Applications of Diamond*, (edited by M H Nazaré and A J Neves), 26, pp. 193–203 (INSPEC, The Institution of Electrical Engineers, London, United Kingdom, 2001).
- Davies G, Neves A J, and Nazaré M H, *Europhys. Lett.* **9**, 47 (1989).
- Delerue C, Lannoo M, and Allan G, *Phys. Rev. B* **39**, 1669 (1989).
- Dresselhaus M S and Kalish R, *Ion Implantation in Diamond, Graphite and Related Materials* (Springer-Verlag, Berlin, Germany, 1992).
- Evans T, in *The Properties of Natural and Synthetic Diamond*, (edited by J E Field), pp. 259–290 (Academic Press, London, United Kingdom, 1992).
- Evans T and Qi Z, *Proc. R. Soc. London A* **381**, 159 (1982).
- Farrer R G, *Solid State Commun.* **7**, 685 (1969).
- Feher G, *Phys. Rev.* **103**, 834 (1956).
- Field J E, in *The Properties of Natural and Synthetic Diamond*, (edited by J E Field), pp. 667–699 (Academic Press, London, 1992).
- Fisher D and Lawson S C, *Diamond Relat. Mater.* **7**, 299 (1998).
- Frens A M, Bennebroek M T, Zakrzewski A, Schmidt J, Chen W M, Janzén E, Lindström J L, and Monemar B, *Phys. Rev. Lett.* **72**, 2939 (1994).

- Gippius A A and Collins A T, *Solid State Commun.* **88**, 637 (1993).
- Godlewski M, *Phys. Status Solidi (a)* **90**, 11 (1985).
- Gordy W, *Theory and Applications of Electron Spin Resonance* (John Wiley & Sons, New York, USA, 1980).
- Goss J, <http://newton.ex.ac.uk/people/goss/symmetry/index.html> (2000).
- Griffith J S, *Theory of Transition Metal Ions* (Cambridge University Press, Cambridge, United Kingdom, 1961).
- Günther H, *NMR Spectroscopy: Basic Principles, Concepts, and Applications in Chemistry* (John Wiley & Sons, Chichester, 1998).
- Harris R K, *Nuclear Magnetic Resonance Spectroscopy* (Longman Scientific & Technical, Harlow, 1986).
- Hofmann D M, Ludwig M, Christmann P, Volm D, Meyer B K, Pereira L, Santos L, and Pereira E, *Phys. Rev. B* **50**, 17618 (1994).
- Iakoubovskii K and Adrienssens G J, *J. Phys.: Condens. Matter* **14**, L95 (2002).
- Iakoubovskii K and Stesmans A, *Phys. Status Solidi (a)* **186**, 199 (2001).
- Isoya J, Kanda H, Akaishi M, Morita Y, and Ohshima T, *Diamond Relat. Mater.* **6**, 356 (1997a).
- Isoya J, Kanda H, and Morita Y, *Phys. Rev. B* **56**, 6392 (1997b).
- Isoya J, Kanda H, Norris J R, Tang J, and Bowman M R, *Phys. Rev. B* **41**, 3905 (1990a).
- Isoya J, Kanda H, and Uchida Y, *Phys. Rev. B* **42**, 9843 (1990b).
- Isoya J, Kanda H, Uchida Y, Lawson S C, Yamasaki S, Itoh H, and Morita Y, *Phys. Rev. B* **45**, 1436 (1992).
- Jaros M, *Phys. Rev. B* **16**, 3694 (1977).
- Jones R, Briddon P R, and Öberg S, *Phil. Mag. Lett.* **66**, 67 (1992).
- Kaiser W and Bond W L, *Phys. Rev.* **115**, 857 (1959).

- Kajihara S A, Antonelli A, Bernholc J, and Car R, *Phys. Rev. Lett.* **66**, 2010 (1991).
- Kalish R, *Diamond Relat. Mater.* **10**, 1749 (2001).
- Kalish R, Reznik A, Uzan-Saguy C, and Cytermann C, *Appl. Phys. Lett.* **76**, 757 (2000).
- Kalish R and Uzan-Saguy C, in *Properties, Growth and Applications of Diamond*, (edited by M H Nazaré and A J Neves), 26, pp. 321–330 (INSPEC, The Institution of Electrical Engineers, London, United Kingdom, 2001).
- Kanda H and Sekine T, in *Properties, Growth and Applications of Diamond*, (edited by M H Nazaré and A J Neves), 26, pp. 247–255 (INSPEC, The Institution of Electrical Engineers, London, United Kingdom, 2001).
- Kanda H and Watanabe K, *Diamond Relat. Mater.* **8**, 1463 (1999).
- Kaplianskii A A, *Opt. Spectrosc.* **16**, 329 (1964).
- Katayama-Yoshida H, Nisjimatsu T, Yamamoto T, and Orita N, *J. Phys.: Condens. Matter* **13**, 8901 (2001).
- Kawarada H, Yokota Y, Mori Y, Nishimura K, and Hiraki A, *J. Appl. Phys.* **67**, 983 (1990).
- Keil T H, *Phys. Rev.* **140**, A601 (1965).
- Kelley C S, *Phys. Rev. B* **6**, 4112 (1972).
- Kiflawi I, Kanda H, and Lawson S C, *Diamond Relat. Mater.* **11**, 204 (2002).
- Kiflawi I, Kanda H, Lawson S C, and Fisher D, *Diamond Relat. Mater.* **6**, 1643 (1997).
- Kiflawi I, Kanda H, and Mainwood A, *Diamond Relat. Mater.* **7**, 327 (1998).
- Kiflawi I, Mainwood A, Kanda H, and Fisher D, *Phys. Rev. B* **54**, 16719 (1996).
- Kiflawi I, Mayer A E, Spear P M, van Wyk J A, and Woods G S, *Philos. Mag. B* **69**, 1141 (1994).
- Kittel C, *Introduction to Solid State Physics* (John Willey & Sons, New York, USA, 1996).
- Koizumi S, Kamo M, Sato Y, Mita S, Sawabe A, Reznik A, Uzan-Saguy C, and Kalish R, *Diamond Relat. Mater.* **7**, 540 (1998).

- Koizumi S, Kamo M, Sato Y, Ozaki H, and Inuzuka T, *Appl. Phys. Lett.* **71**, 1065 (1997).
- Kopylov A A and Pikhtin A N, *Fiz. Tverd. Tela* **16**, 1837, [*Soviet Phys. Solid State* **16**, 1200 (1975)] (1974).
- Kupriyanov I N, Gusev V A, Borzdov Y M, Kalinin A A, and Pal'yanov Y N, *Diamond Relat. Mater.* **8**, 1301 (1999).
- Kupriyanov I N, Pal'yanov Y N, Gusev V A, Borzdov Y M, Kalinin A A, Khokhryakov A F, and Sokol A G, in *21st International Conference on Defects in Semiconductors*, (edited by D M Hofmann) (2001).
- Lancaster G, *Electron Spin Resonance in Semiconductors* (Hilger & Watts, London, United Kingdom, 1966).
- Lang A R, Moore M, and Walmsley J C, in *The Properties of Natural and Synthetic Diamond*, (edited by J E Field), pp. 215–258 (Academic Press, London, United Kingdom, 1992).
- Lawson S C, Fisher D, Hunt D C, and Newton M E, *J. Phys.: Condens. Matter* **10**, 6171 (1998).
- Lawson S C and Kanda H, *J. Appl. Phys.* **73**, 3967 (1993).
- Lawson S C and Kanda H, *J. Appl. Phys.* **79**, 4348 (1996).
- Lax M and Burstein E, *Phys. Rev.* **97**, 39 (1955).
- Loubser J H N and van Ryneveld W P, *Nature* **211**, 517 (1966).
- Loubser J H N and van Ryneveld W P, *Br. J. Appl. Phys.* **18**, 1029 (1967).
- Loubser J H N and van Wyk J A, *Rep. Prog. Phys.* **41**, 1201 (1978).
- Lucovsky G, *Solid State Commun.* **3**, 299 (1965).
- Ludwig G W and Woodbury H H, *Phys. Rev. Lett.* **5**, 98 (1960).
- Ludwig G W and Woodbury H H, in *Solid State Physics*, (edited by F Seitz and D Turnbull), volume 13, pp. 223–304 (Academic, New York, 1962).
- Machi I Z, Connell S H, Baker M, Sellschop J P F, Bharuth-Ram K, Fisher C G, Nilen R W, Cox S F J, and Butler J E, *Physica B* **289-290**, 507 (2000).

- Markham J J, Rev. Mod. Phys. **31**, 956 (1959).
- Mashkovtsev R I and Palyanov Y N, Solid State Commun. **111**, 397 (1999).
- Mason P W, Ham F S, and Watkins G D, Phys. Rev. B **60**, 5417 (1999).
- Messmer R P and Watkins G D, Phys. Rev. B **7**, 2568 (1973).
- Mims W B, in *Electron Paramagnetic Resonance*, (edited by S Geschwind), pp. 227–376 (Plenum, New York, USA, 1972).
- Miyazaki T, Okishi H, and Uda T, Phys. Rev. Lett. **88**, 066402 (2002).
- Monemar B and Samuelson L, Phys. Rev. B **18**, 809 (1978).
- Nadolinny V A and Yelisseyev A P, Diamond Relat. Mater. **3**, 17 (1993).
- Nadolinny V A and Yelisseyev A P, Diamond Relat. Mater. **3**, 1196 (1994).
- Nadolinny V A, Yelisseyev A P, Baker J M, Newton M E, Twitchen D J, Lawson S C, Yuryeva O P, and Feigelson B N, J. Phys.: Condens. Matter **11**, 7357 (1999).
- Nadolinny V A, Yelisseyev A P, Baker J M, Twitchen D J, Newton M E, Feigelson B N, and Yuryeva O P, Diamond Relat. Mater. **9**, 883 (2000).
- Nadolinny V A, Yelisseyev A P, Yuryeva O P, and Feigelson B N, Appl. Magn. Reson. **12**, 543 (1997).
- Nassau K, *Gems Made by Man* (Chilton, Radnor, 1980).
- Nazaré M H, Lopes J C, and Neves A J, Physica B **308-310**, 616 (2001).
- Nazaré M H and Neves A J, editors, *Properties, Growth and Applications of Diamond*, 26 (INSPEC, The Institution of Electrical Engineers, London, United Kingdom, 2001).
- Nazaré M H, Neves A J, and Davies G, Phys. Rev. B **43**, 14196 (1991).
- Nazaré M H and Rino L M, Materials Sci. Eng. **B21**, 329 (1993).
- Neves A J, Nazaré M H, Lopes J P, and Kanda H, Physica B **273-274**, 636 (1999a).
- Neves A J, Pereira R, Sobolev N A, Nazaré M H, Gehlhoff W, Näser A, and Kanda H, Physica B **273-274**, 651 (1999b).

- Neves A J, Pereira R, Sobolev N A, Nazaré M H, Gehlhoff W, Näser A, and Kanda H, *Diamond Relat. Mater.* **9**, 1057 (2000).
- Newton M, Baker J, and Twitchen D, in *Properties, Growth and Applications of Diamond*, (edited by M H Nazaré and A J Neves), 26, p. 204 (INSPEC, The Institution of Electrical Engineers, London, United Kingdom, 2001).
- Noble C J, Pawlik T, and Späth J M, *J. Phys.: Condens. Matter* **10**, 11781 (1998).
- Okano K, in *Diamond: Electronic Properties and Applications*, (edited by S P Lawrence and D R Kania), pp. 139–174 (Kluwer Academic Press, Dordrecht, 1995).
- Pake G E and Estle T L, *The Physical Principles of Electron Paramagnetic Resonance* (W. A. Benjamin Inc., London, United Kingdom, 1973).
- Pan L S and Kania D R, *Diamond: Electronic Properties and Applications* (Kluwer Academic Publishers, Boston, USA, 1995).
- Pantelides S T, *Rev. Mod. Phys.* **50**, 797 (1978).
- Paslovsky L and Lowther J E, *J. Phys.: Condens. Matter* **4**, 775 (1992).
- Pawlik T, Noble C J, and Späth J M, *J. Phys.: Condens. Matter* **10**, 9833 (1998).
- Pereira M E, in *Luminence: Phenomena, Materials and Devices*, (edited by R P Rao), p. 137 (Nova Science Publisher, New York, USA, 1992).
- Pereira R N, Gehlhoff W, Neves A J, and Sobolev N A, submitted to *Phys. Rev. B* (2002a).
- Pereira R N, Gehlhoff W, Sobolev N A, and Neves A J, to be published (2002b).
- Pereira R N, Gehlhoff W, Sobolev N A, Neves A J, and Bimberg D, *J. Phys.: Condens. Matter* **13**, 8957 (2001a).
- Pereira R N, Gehlhoff W, Sobolev N A, Neves A J, and Bimberg D, *Physica B* **308-310**, 589 (2001b).
- Pereira R N, Neves A J, Gehlhoff W, Sobolev N A, Rino L, and Kanda H, *Diamond Relat. Mater.* **11**, 623 (2002c).
- Pereira R N, Neves A J, Gehlhoff W, Sobolev N A, Rino L, and Kanda H, to be published (2002d).

- Petit J, Allan G, and Lannoo M, *Phys. Rev. B* **33**, 8595 (1986).
- Piekara U, Langer J M, and Kruskowska-Fulde B, *Solid State Commun.* **23**, 583 (1977).
- Pilbrow J R, *Transition Ion Electron Paramagnetic Resonance* (Oxford University Press, Oxford, United Kingdom, 1990).
- Poole C P, *Electron Paramagnetic Resonance: A Comprehensive Treatise on Experimental Techniques* (Dover Publications, Inc., Mineola, New York, USA, 1983).
- Prins J F, *Diamond Relat. Mater.* **10**, 1756 (2001).
- Ramdas A, in *Properties, Growth and Applications of Diamond*, (edited by M H Nazaré and A J Neves), 26, pp. 3–13 (INSPEC, The Institution of Electrical Engineers, London, United Kingdom, 2001).
- Ridley B K, *J. Phys. C: Solid St. Phys.* **13**, 2015 (1980).
- Ridley R K, *Quantum Processes in Semiconductors* (Oxford University Press, Oxford, United Kingdom, 1999).
- Rosa J, Vaneck M, Nesladek M, and Stals L, *Diamond Relat. Mater.* **8**, 721 (1999).
- Saada D, Adler J, and Kalish R, *Appl. Phys. Lett.* **77**, 878 (2000).
- Samoilovich M I, Bezrukov G N, and Butuzov V P, *ZhETF Pis. Red.* **14**, 551, [*JETP Lett.* **14**, 379 (1971)] (1971).
- Samsonenko N D, Toiř V V, and Gorban' S V, *Fiz. Tverd. Tela* **33**, 2496, [*Soviet Phys. Solid State* **33**, 1409 (1991)] (1991).
- Samuelson L and Monemar B, *Phys. Rev. B* **18**, 830 (1978).
- Satoh S and Sumiya H, in *High Pressure Research in Solids*, (edited by M Senoo, K Suito, T Kayabashi, and H Kubota), p. 270 (Elsevier Science and The Society of Material Science, Japan, 1995).
- Schiff L I, *Quantum Mechanics* (McGraw-Hill, New York, USA, 1968).
- Sellschop J P F, in *The Properties of Natural and Synthetic Diamond*, (edited by J E Field), pp. 81–179 (Academic Press, London, United Kingdom, 1992).

- Shu'lman L A, Zaritskii I M, and Podzyarei G A, *Sov. Phys.-Solid State* **8**, 1842 (1967).
- Sigel H, *ENDOR, EPR, and Electron Spin Echo for Probing Coordination Spheres* (Marcel Dekker, New York, USA, 1987).
- Slichter C P, *Principles of Magnetic Resonance* (Springer-Verlag, Berlin, Germany, 1996).
- Smith W V, Sorokin P P, Gelles I L, and Lasher G J, *Phys. Rev.* **115**, 1546 (1959).
- Stoneham A M, *Theory of Defects in Solids* (Clarendon Press, Oxford, United Kingdom, 1975).
- Sueki M, Eaton S S, and Eaton G R, *J. Mag. Reson A* **105**, 25 (1993).
- Twitchen D, Newton M, Baker J, and Nadolinny V, in *Properties, Growth and Applications of Diamond*, (edited by M H Nazaré and A J Neves), 26, p. 214 (INSPEC, The Institution of Electrical Engineers, London, United Kingdom, 2001).
- Twitchen D J, Baker J M, Newton M E, and Johnston K, *Phys. Rev. B* **61**, 9 (2000).
- Vittone E and Manfredotti C, in *Properties, Growth and Applications of Diamond*, (edited by M H Nazaré and A J Neves), 26, pp. 386–392 (INSPEC, The Institution of Electrical Engineers, London, United Kingdom, 2001).
- van Vleck J H, *Electric and Magnetic Susceptibilities* (Oxford University Press, Oxford, United Kingdom, 1932).
- Walker J, *Rep. Prog. Phys.* **42**, 108 (1979).
- Watkins G D, *Physica B* **117-118**, 9 (1983).
- Watkins G D, in *Semiconductors and Semimetals*, (edited by M Stavola), volume 51A, p. 1 (Academic Press, 1999).
- Watkins G D and Williams P M, *Phys. Rev. B* **52**, 16575 (1995).
- Weger M, *Bell Syst. Tech. J.* **39**, 1013 (1960).
- Weil J A, *J. Mag. Reson.* **18**, 113 (1975).
- Weil J A, Bolton J R, and Wertz J E, *Electron Paramagnetic Resonance: Elementary Theory and Practical Applications* (John Wiley & Sons, Inc., New York, USA, 1994).

- Wild C and Koidl P, in *Properties, Growth and Applications of Diamond*, (edited by M H Nazaré and A J Neves), 26, pp. 351–355 (INSPEC, The Institution of Electrical Engineers, London, United Kingdom, 2001).
- Windischmann H, in *Properties, Growth and Applications of Diamond*, (edited by M H Nazaré and A J Neves), 26, pp. 410–415 (INSPEC, The Institution of Electrical Engineers, London, United Kingdom, 2001).
- Winter M, <http://www.webelements.com/> (2002).
- Woods G S, Proc. R. Soc. London A **407**, 219 (1986).
- Woods G S and Collins A T, J. Phys. Chem. Solids **44**, 471 (1983).
- van Wyk J A and Loubser J H N, J. Phys.: Condens. Matter **5**, 3019 (1993).
- van Wyk J A and Woods G S, J. Phys.: Condens. Matter **7**, 5901 (1995).
- Yelisseyev A P and Nadolinny V A, Diamond Relat. Mater. **4**, 177 (1995).
- Zaitsev A M, in *Handbook of Industrial Diamond and Diamond Films*, (edited by M A Prelas, G Popovici, and L K Bigelow), pp. 227–376 (Marcel Dekker, New York, USA, 1998).
- Zaitsev A M, Phys. Rev. B **61**, 12909 (2000).
- Zaitsev A M, in *Properties, Growth and Applications of Diamond*, (edited by M H Nazaré and A J Neves), 26, pp. 155–164 (INSPEC, The Institution of Electrical Engineers, London, United Kingdom, 2001).
- Zavoiskii E K, J. Phys. (URSS) **9**, 245 (1945).
- Zhirnov V V and Hren J J, in *Properties, Growth and Applications of Diamond*, (edited by M H Nazaré and A J Neves), 26, pp. 362–374 (INSPEC, The Institution of Electrical Engineers, London, United Kingdom, 2001).
- Zhu W, in *Diamond: Electronic Properties and Applications*, (edited by S P Lawrence and D R Kania), pp. 175–239 (Kluwer Academic Press, Dordrecht, 1995).